Surface Electrostatic Properties of Organic Semiconductors

A DISSERTATION
SUBMITTED TO THE FACULTY OF
UNIVERSITY OF MINNESOTA
BY

Yanfei Wu

IN PARTIAL FULFILLMENT OF THE REQUIREMENTS
FOR THE DEGREE OF
DOCTOR OF PHILOSOPHY

C. Daniel Frisbie, Advisor

March, 2016

Acknowledgements

First of all, I would like to express my deepest gratitude to my advisor Prof. Dan Frisbie, for his inspiration, guidance and support throughout my PhD research. Thank him for letting me work on this exciting project six years ago. Thank him for his encouragement and suggestions every time when I hit obstacles in my research. And thank him for all the ideas, help, and support which have made this thesis possible. He is a great scientist and also a great mentor! I feel extremely lucky to have Dan as my PhD advisor and I will keep reminding myself everything Dan has taught me over these years.

I would also like to sincerely thank Dr. Greg Haugstad, my "unofficial" co-advisor, for all his guidance and help on my research. Thank him for sharing his expertise on AFM imaging and data analysis, which is the foundation of this thesis. Thank him for the large amount of time he spent on reading my manuscripts, and thank him for all the great ideas and critical comments on my work. I really appreciate all his great help.

I am also grateful for all the collaborators for their assistance on my research: Annabel Chew and Prof. Alberto Salleo (Stanford University) for their tremendous help on quantifying strain in rubrene single crystals by XRD; Dr. Geoff Rojas, for taking on the night shifts in Oak Ridge National Lab to help me with the SKPM measurements; Dr. Gjergji Sini (Université de Cergy-Pontoise), Dr. Hong Li (Georgia Institute of Technology), Prof. Chad Risko (University of Kentucky), and Prof. Jean-Luc Bredas (King Abdullah University of Science and Technology), for performing DFT calculations to verify the strain effects of work function in rubrene; Dr. Alex Belianinovand and Dr. Sergei Kalinin (Oak Ridge National Lab) for providing instrument time and also important technical help on SKPM measurements; Dr. Wei Xie, for growing rubrene single crystals and also for the helpful discussions; Xinglong Ren, for great help on crystal growth, electrical measurements, and XRD measurements, and for helpful discussions.

I would also like to thank all my colleagues in Frisbie group. I am especially thankful to Dr. Vivek Kalihari and Dr. David Ellison for helping me start my project and for all the trainings, suggestions, and help. Thank Dr. Yan Liang, Dr. Bryan Paulsen, Dr.

To my dearest family.

Abstract

Understanding the surface/interface electrostatic properties of organic semiconductors has great implications for the fundamental transport properties of these materials and their performance in devices. Therefore, this thesis aims to correlate electrostatic properties with microstructure and mechanical strain in benchmark organic semiconductors. To this end, a number of scanning probe microscopy (SPM) techniques are employed to examine thin films and single crystals of prototypical organic semiconductors. In particular, strong variations of interfacial polarization at the organic/insulator interfaces are quantified by scanning Kelvin probe microscopy (SKPM). The roles of the dielectric type and deposition condition are identified. Moreover, striking lateral electrostatic heterogeneities are visualized in thermally deposited organic semiconductor bi-layers on various dielectrics, and are directly related to the complex microstructural motifs of the films. The mixed homoepitaxial growth modes, which give rise to the inhomogeneous microstructure, can be conveniently determined by combining two variants of lateral force microscopy (LFM), namely, friction force microscopy (FFM) and transverse shear force microscopy (TSM). Furthermore, a fundamental correlation is established between the surface electrostatic potential and mechanical strain. The effects of tensile and compressive strains in both elastic and plastic regimes are determined for the first time. Overall, organic semiconductors exhibit complex surface/interface electrostatic properties, which can be visualized by SPM and can be correlated with microstructure and mechanical properties.

Table of Contents

List of Tables

List of Figures

Chapter 1 Introduction

1.1 Motivation

Semiconducting materials based on small organic molecules and polymers have received intensive research over the past few decades. The intense interest in organic semiconductors stems from their optical and electrical advantages as semiconductors, as well as their chemical and mechanical benefits as organics. These carbon-rich compounds feature π-conjugated units that form planar or nearly planar molecular structures. Such conjugated structure gives rise to delocalized π-orbitals that afford these materials unique optical and electrical properties for applications. In addition, the structures of organic semiconductors can be easily tailored by chemical synthesis such that optimization of particular functions is possible. Also, organic semiconductors exhibit low-temperature solution processability and are compatible with flexible substrates such as plastics. Therefore, organic semiconductors present great potential for large area, low-cost, flexible electronics for applications in displays, solid-state lighting, solar energy conversion, etc. [1-7]

The large-scale technological exploration of organic semiconductors has led to impressive performance improvement. Notably, high efficiency, very bright and colorful thin displays based on organic light-emitting devices (OLEDs) have already been commercialized.[8-10] Exciting progresses have also been made in the realization of sensors and printed electronics.[11-19] However, fundamental questions still remain regarding the

structure-property-processing relationships of organic semiconductors, which hinders the further development of organic electronics. Therefore, the primary objective of this thesis is to address the fundamental structure-property correlations in order to open up new opportunities for theoretical studies and technological applications of organic semiconductors.

In particular, an important electrical parameter, the surface electrostatic potential, of model organic semiconductors is probed and correlated with microstructure and mechanical properties. The surface electrostatic potential, synonymous with the work function, is an electrical potential energy and a state variable for surface charges. It reflects many intrinsic and extrinsic factors associated with surfaces/interfaces, namely the crystal structure, the spatial distribution of dopant species, the charge states of surface traps, the presence of extended defects (dislocations and grain boundaries), dipoles, fixed charges, contaminations, electric fields, and illumination.[20-22] The surface electrostatic potential is known to impact charge transport along and across the surfaces/interfaces. For example, in an organic field effect transistor (OFET), the surface electrostatic potential variations at the organic/insulator interface will affect the spatial distribution of gate-induced charges, and the peaks and valleys of surface electrostatic potential serve as the barriers or traps for charge transport parallel to the interface.[23-26] Therefore, the surface electrostatic potential is directly relevant to the performance of electronic devices. Probing local surface electrostatic potential distribution and establishing direct links between surface electrostatic potential with microstructure and mechanical properties in

organic semiconductors thus have critical importance for understanding the charge transport bottlenecks in organic electronic devices.

In this thesis, non-destructive and spatially-resolved scanning probe microscopy (SPM) techniques, specifically, scanning Kelvin probe microscopy (SKPM), electrostatic force microscopy (EFM), and lateral force microscopy (LFM) are employed to map the microstructural and surface/interface electrostatic properties of benchmark organic semiconductors. The surface electrostatic potential of organic thin films is related to the polarization effect at organic/dielectric interfaces and to the microstructural features of the films, particularly the complex microstructural motifs arising from homoepitaxial growth modes. In addition, the surface electrostatic potential is linked to the tensile and compressive strains in organic materials, which has important implications for flexible electronics.

1.2 Thesis Overview

Chapter 2 introduces the basic aspects of bonding and structure of organic semiconductors, in particular, conjugated small organic molecules. Fabrication techniques for both thin films and single crystals of organic semiconductors are reviewed. Examples are given including benchmark pentacene thin films and rubrene single crystals.

Chapter 3 focuses on the physics, operational modes, and applications of scanning probe microscopy (SPM). Detailed descriptions of several advanced SPM techniques, including friction force microscopy (FFM), transverse shear microscopy (TSM), scanning

3

Kelvin probe microscopy (SKPM), and electrostatic force microscopy (EFM), are presented.

Chapter 4 presents a comprehensive SKPM study of surface potentials and contact potential differences across ultrathin (1-2 monolayer) crystalline islands of the benchmark organic semiconductor pentacene thermally deposited on a variety of polymer dielectrics. Strong variations in the interfacial polarization and lateral electrostatic heterogeneity are observed, arising from the dielectric type, deposition conditions, and microstructure (i.e., homoepitaxy) inhomogeneity. This work is published as *Y. Wu, G. Haugstad and C. D. Frisbie, The Journal of Physical Chemistry C, 118, 2487-2497 (2014).*

Chapter 5 describes a combined FFM/TSM technique as a feasible way to identify complex microstructural motifs due to mixed homoepitaxial growth modes in pentacene bi-layers deposited on a variety of dielectric substrates. The different homoepitaxial modes are further correlated to the lateral surface potential variations and one-to-one correspondences between homoepitaxy and surface potential are generally established in pentacene bi-layers. This work is published as *Y. Wu, V. Kalihari, G. Haugstad, and C. D. Frisbie, Physica Status Solidi b, 252, 1291-1299 (2015).*

Chapter 6 reports the first concrete link between mechanical strain and a key electrical property, the work function, in rubrene single crystals. By utilizing mismatch of coefficients of thermal expansion between rubrene and the substrates, controlled tensile and compressive strains are induced in rubrene. The strains are quantified by *in-situ* X-ray diffraction and the corresponding work function changes are measured by

temperature-dependent SKPM. We find that the WF of rubrene increases (decreases) significantly with in-plane tensile (compressive) strain. This work is published as *Y. Wu, A. R. Chew, G. Rojas, G. Sini, A. Belianinov, S. V. Kalinin, H. Li, C. Risko, J.-L. Bredas, G. Haugstad, A. Salleo and C. D. Frisbie, Nature Communications 7, (2016).*

Chapter 7 proposes potential future research projects based on our previous findings.

Chapter 2 Organic Semiconductors

Organic semiconductors, as a low-cost alternative to silicon, are attractive candidates for large-area, light-weight, flexible, inexpensive electronic applications. Unlike their inorganic counterparts, these π-conjugated materials are held together by weak van der Waals force, and hence they exhibit very different optical and electronics properties than inorganic semiconductors. This chapter will focus on some general aspects of organic semiconductors that govern the electronic transport properties in organic devices. The scope of discussion will mainly be on small organic molecules. Particular emphasis will be placed on bonding, structure, and the growth of organic molecular thin films and single crystals. Benchmark organic semiconductor systems including pentacene thin films and rubrene single crystals will be introduced.

2.1 Structure and Bonding

The bonding and structure are, amongst all, two key factors that distinguish organic semiconductors and determine their unique electronic transport properties. Comprising small organic molecules and polymers, organic semiconductors commonly feature π-conjugated bonds. In contrast to inorganic semiconductors, such as Si and Ge, which are bound by strong covalent interaction, the solid-state structure of organic semiconductors is based on significantly weaker interactions between neighboring molecules or polymer chains, primarily van der Waals and dipole-dipole interactions. A key consequence is that

organic semiconductors typically have less overlap in the wavefunctions of neighboring molecules/polymer chains and hence the transport is less delocalized in organic semiconductors compared to their traditional inorganic counterparts.

Organic molecules, for example, are highly conjugated systems composed of thiophene or benzene ring building blocks. The benzene ring, as a typical conjugated molecule, has alternating single and double bonds. The π-conjugation in a benzene ring is realized by overlapping one p_z orbital with another across an intervening σ bond as shown in Figure 2.1. All of the carbon atoms are sp^2-hybridized in a way that the one s orbital and two p orbitals (p_x and p_y) combine to create three new hybrid orbitals with equal energy level, i.e., the σ bond. The π bond is then formed by combination of the remaining p_z orbitals. Due to the cyclic structure of benzene ring, the electrons in π bonds (π electrons) are able to delocalize in molecular orbitals that extend all the way around the ring, above and below the plane of the ring, as shown in Figure 2.1. Such delocalized π-electron system is essential for organic semiconductors as it provides the conduction pathway for charge carriers.

p_z orbital   **σ bond**   **π orbital**

6 p_z orbitals   **Delocalized**
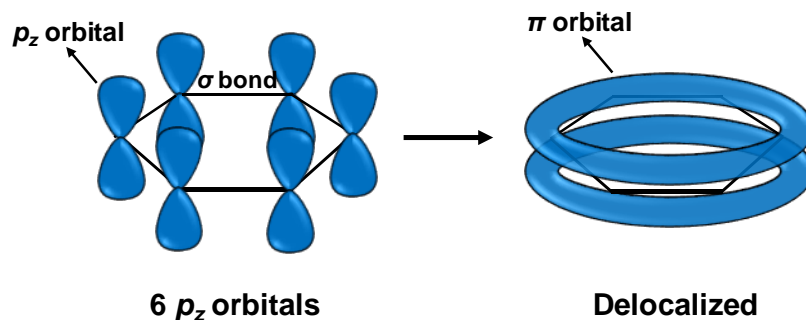
Figure 2.1 sp^2 hybridization of p_z orbitals in a benzene ring.

The effectiveness of π-π overlap between molecules, therefore, is critical to the transport properties of organic semiconductors, and is largely determined by the packing motif. There are two major categories of packing motifs, namely herringbone packing and π stacking,[27, 28] resulting from a complex balance of intramolecular interactions within a very narrow energy range. A more detailed classification considers the specific π-overlaps among neighboring molecules and thus results in four different types of packing motifs as shown in Figure 2.2.[29-32]
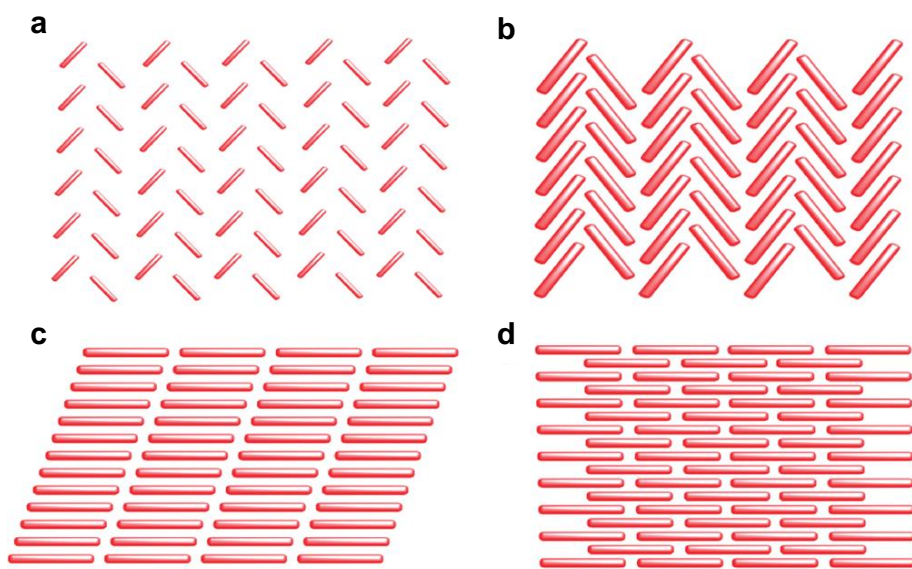
Figure 2.2 Molecular packing motifs in organic semiconductors. [ref 29]
(a) Herringbone packing (face-to-edge) without π-π overlap between adjacent molecules, e.g., pentacene. (b) Herringbone packing with π-π overlap between adjacent molecules, e.g., rubrene. (c) Lamellar motif, 1-D π-stacking, e.g., hexyl substituted naphthalene diimide. (d) Lamellar motif, 2-D π-stacking, e.g., TIPS-Pentacene.

One of the herringbone motifs (Figure 2.2a), exhibiting only face-to-edge stacking, does not have π-π overlap between adjacent molecules. Examples of molecules that adopt this type of packing motif include most acene molecules, such as pentacene. The other

herringbone packing motif, depicted in Figure 2.2b, shows both face-to-edge and face-to-face stacking. Therefore, this so-called "slipped π stacking" promotes some extent of π-π interactions between adjacent molecules and hence is more favorable for charge transport. Rubrene is an exemplary molecule adopting this packing motif, which has been reported to exhibit much higher hole mobility than pentacene.[33] Regardless, the π-π overlap is more or less minimized by the edge-to-face packing in herringbone motif. Therefore, molecules that stack only face-to-face in the solid-state are believed to better facilitate carrier transport. Figure 2.2c shows the schematic of a one-dimensional π stacking where effective π-π overlap is only along one direction. An example of organic molecule adopting this type of packing motif is hexyl substituted naphthalene diimide. However, such one-dimensional π-stacks are still not in a perfectly face-to-face manner for improved transport behavior. The most ideal packing motif for efficient charge transport is therefore two-dimensional π stacking as shown in Figure 2.2d. Clearly, the π-π intermolecular interaction is maximized in this kind of packing motif. 6,13-Bis(triisopropylsilylethynyl)pentacene (TIPS-pentacene) is reported to have the two-dimensional π stacking.

2.2 Organic Semiconductor Thin Films

Thin Films of organic semiconductors are of significant interest due to their ease of processing and compatibility with flexible substrates. Particular attention has been

focused on realization of organic thin film transistors (OTFTs), organic thin film photovoltaic cells, and organic light emitting devices (OLEDs).[34, 35]

Take OTFTs, which are potential building blocks for various applications including radio-frequency ID tags and sensors,[16, 17] as an example. An OTFT is a special variant of field effect transistors (FETs) made by depositing an organic semiconductor active layer as well as the dielectric layer and metallic contacts on a supporting substrate, such as glass and plastic. Typical geometries of top contact and bottom contact OTFTs are shown in Figure 2.3.
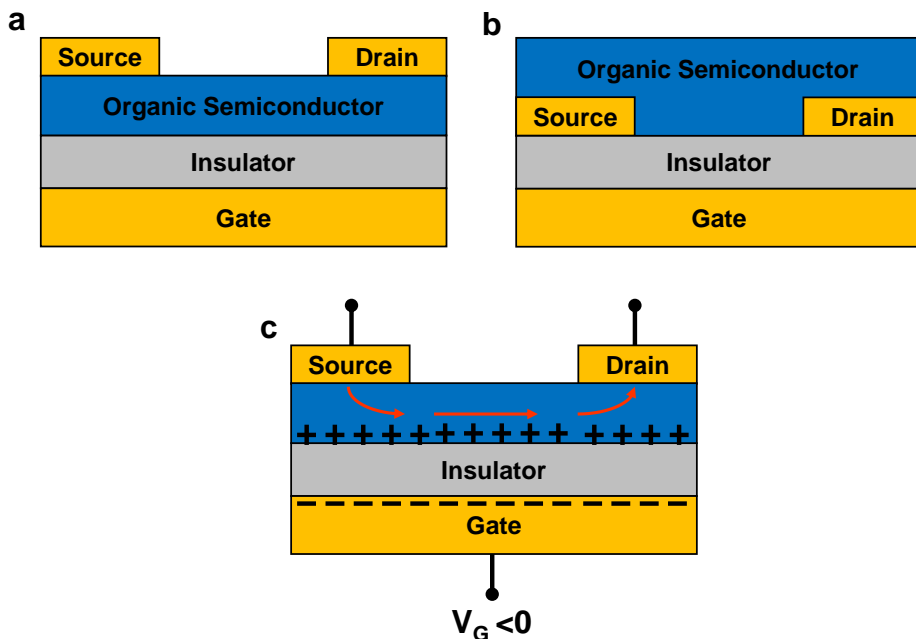
Figure 2.3 Schematics of OFETs and operation OFET.
(a) Top contact OFET. (b) Bottom contact OFET. (c) Operation of an OFET with p-type organic semiconductor.

In both top and bottom contact OTFTs, a thin film of organic semiconductor active layer is deposited on an insulating substrate. There are three electrodes used to operate

the device, the source, drain and gate electrode. The basic operation of an OTFT is relatively simple and will be demonstrated here using a p-type OTFT as a model. The organic semiconductor active layer and the gate electrode can be viewed as a capacitor separated by a dielectric. If the gate electrode is biased positively, the channel is depleted and the transistor is in "off state". When a negative gate bias V_G is applied to the gate electrode, negative charges are induced at the interface of gate electrode and insulator. In the meantime, positive charges will build on the organic semiconductor/insulator interface in an attempt to balance the net charge. The transistor is now operating in the accumulating mode or "on state" with a large carrier concentration in the channel.

It is intuitive that the organic semiconductor thin film incorporated in an OTFT plays the key role in the performance of the device. Indeed, strong correlations between film quality/crystallinity and device performance have been demonstrated. In particular, it is generally accepted that the majority of charge carriers induced by the gate insulator are confined within the first few monolayers of organic semiconductor films close to the organic/insulator (O/I) interfaces, and the electrical performance of the devices is inextricably connected to the microstructure of these layers.[36-39] Therefore, it is critical to understand the growth and structure of organic semiconductor thin films. The following sections will discuss the fabrication method and growth mechanism of organic semiconductor active layers that are central to the performance of organic thin film devices. Detailed information of the growth of pentacene thin films will be given to demonstrate several practical aspects that affect the film microstructures.

11

2.2.1   Organic Thin Film Deposition

The organic active layers in devices such as OTFTs can be fabricated either by vacuum sublimation or solution processing. Solution processing utilizes soluble organic semiconductors. The organic semiconductor is completely dissolved in an organic solvent and the solution is then coated onto the substrate by either drop-casting, spin-coating, dip-coating, or printing. Solution processing provides a cost-effective fabrication method as it eliminates the need for expensive vacuum chambers and lengthy pump-down cycles. Moreover, it enables high-throughput, large area manufacturing, as required for successful commercialization of organic semiconductor devices. Therefore, a lot of efforts have been devoted to the synthesis of soluble organic molecules so that that they can be solution-processed because small organic molecules, in general, are not very soluble in organic solvent. Some limitations of solution processing methods include the difficulty to locally pattern the film and the possibility for the solvent to attack existing layers. More importantly, for the purpose of fundamental structure-property relationship, the complex microstructure of solution-processed films can be difficult to assess and it is even harder to correlate it with electrical properties. Therefore, this part of the thesis will be focused on vacuum sublimation method.

Physical vapor evaporation is one of the most commonly used techniques to deposit thin films of small organic molecules due to its simplicity and relative ease of control.[40, 41] A schematic of the technique is shown in Figure 2.4. This method involves vaporization of source material in vacuum and condensation of the sublimed source vapor to a cooler substrate. It can be utilized for a variety of small organic molecules, as long as

the molecules have high decomposition temperature than the sublimation temperature. Crystalline films with well-controlled thicknesses are typically produced, which are of both fundamental and practical interests.
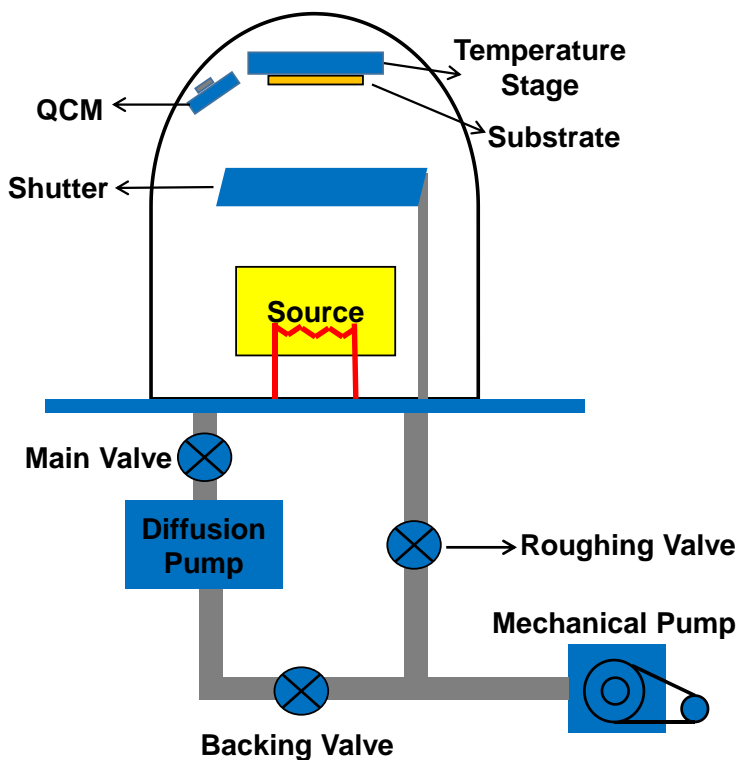
Figure 2.4 Schematic of a thermal evaporation system.

In a typical evaporation process,[40] thermal energy is imparted to the source material placed in a ceramic crucible in a vacuum chamber with a pressure of about 10^{-6} Torr. When the source material is slowly heated to its sublimation point, source molecules are transferred to the substrates aligned a distant away above the source. This so called "bottom up" geometry is favored over the "top down" geometry since it can effectively prevent the source material from splitting out of the source crucible. Also, because dust is

13

unable to land on the substrates, contamination of the substrates is largely avoided. The deposition rate can be monitored using a quartz crystal microbalance (QCM) located close to the substrates. This makes thermal evaporation a controllable technique to deposit organic thin films with desired thickness.

The morphology and crystallinity of thermally deposited films are closely related to several important deposition variables including the pressure of the vacuum system, the deposition rate determined by the source crucible temperature and the substrate temperature.[40] To better understand the impact of these variables on the microstructure of as-deposited films, fundamental growth mechanism in thermal evaporation is introduced in the following section, including the thermodynamics of nucleation and growth, the rate of nucleation, and the growth modes.

2.2.2   Growth Mechanism

Concepts from film growth of inorganic materials have been used to interpret the growth of organic thin films since the organic thin-film growth closely mimics the growth of inorganic materials in a number of fundamental aspects. This section (1) introduces the atomistic model for nucleation and growth; (2) reviews the thermodynamic and kinetic considerations for deriving the rate and density of nucleation; and (3) presents three primary growth modes.

The growth of thin films involves nucleation and growth. In the atomistic model,[42] typical microscopic processes that may occur during nucleation and growth of thin films (Figure 2.5) are taken into consideration. For vapor deposition from ideal gas at a certain

14

pressure, molecules condense onto a perfect substrate surface with a flux of $F(a)$, typically measured in monolayers per second. Once molecules are on the surface, referred to as ad-molecules, they can (i) diffuse laterally with a diffusion constant $D(b)$; (ii) meet other ad-molecules to form a dimer, or (iii) attach to existing islands. Once ad-molecules are attached to an island, they can detach from the island edge or diffuse along the island edge. Other possible processes include deposition of ad-molecules on top of islands and desorption of ad-molecules at high temperatures. Each of these processes has characteristic time, which is dependent on the concentration of molecules and the coverage. For thermally activated processes, such as diffusion and desorption, their characteristic times are determined by the activation energies and the frequency factor. For instance, the characteristic time for desorption (τ_a) is given by:

$$\tau_a = v^{-1}exp\left(\frac{E_a}{kT_S}\right) \qquad \textbf{Equation 2.1}$$

where E_a is the activation energy for desorption, T_s is the substrate temperature, k is the Boltzmann's constant, and v is the frequency factor. Therefore, we need two system variables (T_s and $F(a)$) as well as three materials parameters E_d (activation energy for diffusion), E_a, and E_i (binding energy for small cluster with size i) (Figure 2.5) to describe the early stage nucleation and growth.
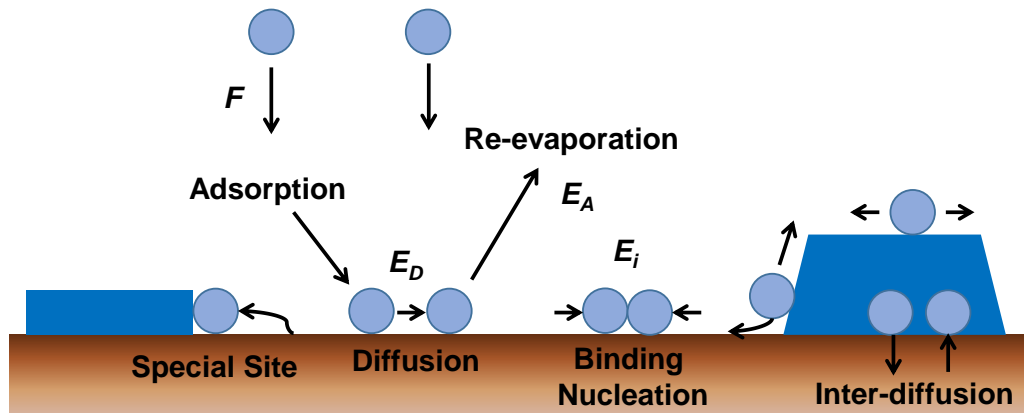
Figure 2.5 atomistic model for nucleation and growth.

In terms of nucleation, in organic thin film deposition, it requires that the vapor phase (v) and crystalline phase (c) deposited on the substrate is in thermodynamic inequilibrium; that is, when the vapor phase and crystalline phase are both at the same pressure and temperature, the chemical potential of the two phases, i.e., the work needed to change the number of molecules in the phase by one molecule ($\mu = \delta G/\delta n$), are different. The chemical potential difference, $\Delta\mu$, is known as the thermodynamic driving force for nucleation of molecules in vapor to an infinitely large crystal. When molecules at supersaturation are transferred from vapor into a finite sized crystal with j molecules, the free energy needed is expressed by:

$$\Delta G(j) = -j\Delta\mu + j^{\frac{2}{3}}\sum_i r_i A_i \qquad\qquad \textbf{Equation 2.2}$$

where $\Delta\mu = \mu_c - \mu_v$, r_i is the surface energy of surface i with area A_i. Therefore, Equation 2.2 shows that the nucleation process is a competition between thermodynamic driving force (first term) and the energy needed to increase the surface area. This equation, although could be problematic when nucleation at very small islands are considered, is a

16

reasonable approximation of the relationship between free energy, crystal size and surface energy that describes the nucleation behavior.

The two competing terms in Equation 2.2 result in an energy barrier (ΔG^*) for stable nucleus formation. When the nucleus is small, the surface effect is dominant in Equation 2.2; that is, adding one molecule increases surface energy and thus the instability of the nucleus. As the nucleus gets larger, or the instability reaches its maxima, the volume effect becomes dominant, i.e., there are enough molecules in the aggregates so that they can adjust themselves to improve stability. The critical size (*i*) of the nucleus for stable nucleation can be obtained by differentiating Equation 2.2:

$$\left(\frac{\partial G(j)}{\partial j}\right)_{T,P} = 0$$

Equation 2.3

The energy barrier for nucleation ΔG^* is thus equal to *G(i)*, where *i* is the critical size solved from the above equation.

In addition to thermodynamic models, several kinetic models have also been adopted to describe nucleation and growth of organic materials. These models are also developed from inorganic materials. The assumption for generating kinetic rate equations is that only single molecules are mobile on the substrate surface. Based on the processes introduced in Figure 2.5, the rate equations are given by:

$$\frac{dN_1}{dt} = F(a) - \frac{N_1}{\tau_a} - \sum_{j=2}^{\infty} U_j$$

Equation 2.4

$$\frac{dN_j}{dt} = U_{j-1} - U_j \ (j \geq 2)$$

Equation 2.5

where N_1 is the surface concentration of organic molecules in units of number of molecules per unit area, N_j is the concentration of clusters with j molecules, U_i is the net rate of capture of single molecules by clusters with j molecules.

If the clusters are divided into unstable ($j \leq i$) and stable ($j > i$), the concentration of all stable clusters is thus given by:

$$N_x = \sum_{i+1}^{\infty} N_j \qquad \textbf{Equation 2.6}$$

The above rate equations can be simplified to:

$$\frac{dN_1}{dt} = F(a) - \frac{N_1}{\tau_a} - \frac{d(N_x w_x)}{dt} \qquad \textbf{Equation 2.7}$$

$$\frac{dN_j}{dt} = 0 \qquad \textbf{Equation 2.8}$$

$$\frac{dN_x}{dt} = U_i - U_c \qquad \textbf{Equation 2.9}$$

where the third term in Equation 2.7 represents the growth of N_x stable clusters with w_x average molecules. The second term (U_c) in Equation 2.9 takes into account the coalescence of two stable clusters, in which case the number of stable clusters decreases.

According to the thermodynamic and kinetic considerations, the rate of nucleation is therefore a function of the rate of deposition, the substrate temperature, surface properties of the substrate, intermolecular interactions, and molecule–surface interactions. The energetic terms that are relevant to heterogeneous nucleation and growth include the activation energy for diffusion E_d, the activation energy for desorption E_a, and the energy barrier for nucleation ΔG^*. Based on the rate equations introduced above, the nucleation density of stable islands (N_D) can be written as:

$$N_D = \frac{n_x}{N_0} = \left(\frac{F}{N_0}\right)^\rho exp\left(\frac{E}{kT_S}\right)$$

Equation 2.10

where ρ is a constant related to the critical cluster size and is dependent on the regimes of condensation (see Table 2.1), E is a function of E_d, E_a, and ΔG^*. Assuming that the energy barrier for nucleation and the deposition rate scale equivalently, and the chemical potential driving force is small, then $E = (-E_a + E_d + \Delta G^*)$. Therefore, the nucleation density of stable islands can be re-written as:

$$N_D = \frac{n_x}{N_0} = \left(\frac{F}{N_0}\right)^\rho exp\left(\frac{-E_a + E_d + \Delta G^*}{kT_S}\right)$$

Equation 2.11

This equation clearly demonstrates the roles of the three energetic barriers on the nucleation density.

Table 2-1 Maximum cluster density in different condensation regimes.

Regime	3D islands	2D islands
Extreme incomplete	$\rho = 2i/3$ $E = 2/3\ [E_i + (i + 1)\ E_a - E_d]$	$\rho = i$ $E = [E_i + (i + 1)\ E_a - E_d]$
Initially incomplete	$\rho = 2i/5$ $E = 2/5\ (E_i + i\ E_a)$	$\rho = i/2$ $E = 1/2\ (E_i + i\ E_a)$
Complete	$\rho = i/(i + 2.5)$ $E = (E_i + i\ E_d)/(i + 2.5)$	$\rho = i/(i + 2)$ $E = (E_i + i\ E_d)/(i + 2)$

When the microstructure and related properties of an organic thin film are concerned, another important aspect aside from nucleation density is the growth modes. It is generally known that there are three different growth modes,[42] namely island mode, layer mode, and layer-plus-island mode, as depicted in Figure 2.6.
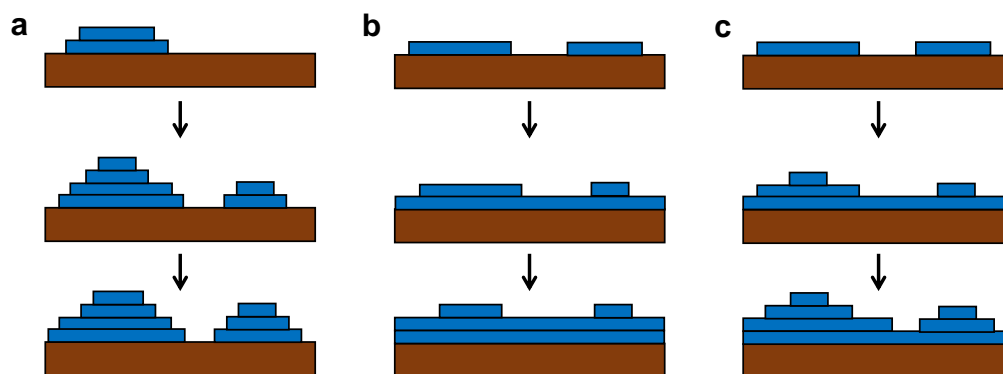
Figure 2.6 Growth modes of thin films. [ref 42]
(a) Island mode, or Volmer-Weber (VW) mode. (b) Layer mode, or Frank-van der Merwe (FM) mode. (c) Layer-plus-island mode, or Stranski-Krastonov (SK) mode.

The island mode (Figure 2.6a), also known as the Volmer-Weber (VW) mode, describes the nucleation of small clusters directly onto the substrate surface and the growth into three-dimensional islands of condensed phase. This happens when the molecules are more strongly bond to each other than to the substrate. This three-dimensional growth mode, however, is not favorable as it usually creates voids as well as more severe grain boundaries in the film. In contrast to the island mode, the layer mode (Figure 2.6b), or the Frank-van der Merwe (FM) mode, is a two-dimensional growth mode. The molecules are more tightly bound to the substrate than to each other so that the first molecules tend to condensate on the surface to form a complete monolayer. The second layer that covers the first layer is actually more weakly bound. Such monotonic decrease in binding leads to a layer-by-layer growth of films toward to the bulk. This growth mode is preferable in organic semiconductor applications as it gives rise to high film quality and hence high mobility. The third growth mode, the layer-plus-island or the Stranski-Krastonov (SK) growth mode (Figure 2.6c), is an intermediate case

characterized by both two-dimensional and three-dimensional island growth. It initially adopts the layer growth mode up to one or a few monolayers until subsequent layer growth becomes unfavorable and islands are formed on top of the "intermediate wetting layer". This growth mode is more commonly observed in the growth of many materials and can be better understood from a thermodynamic point of view.

Differences in growth modes can be attributed to the influences of the surface and the relevant interfacial energies. The change of free energy (ΔG) for the formation of an organic film with area A_A on top of a substrate with area A_B is given by:

$$\Delta G = \gamma_A A_A + \gamma_i A_i - \gamma_B A_B$$ **Equation 2.12**

where γ_A is the surface energy of the organic film, γ_B is the surface energy of the substrate, and γ_i is the interfacial surface energy between the organic film and the substrate. For layer growth mode, $A_A = A_i = A_B$ and $\Delta G \leq 0$. Thus, the criteria for layer mode and island mode are given by:

$$\gamma_B \geq \gamma_A + \gamma_i$$ **Equation 2.13**

$$\gamma_B < \gamma_A + \gamma_i$$ **Equation 2.14**

The SK mode can be described by both Equations, i.e., Equation 2.13 holds for the initial layer growth and then Equation 2.14 becomes true.

Note that the atomistic model as well as the thermodynamic and kinetic arguments discussed above is rather simple because they treat the molecules as isotropic spheres so that the orientation of the ad-molecules relative to the substrate or to other molecules is irrelevant. However, the real situation is much more complex when turning to organic molecules deposited on solid substrates as they are generally known with pronounced

21

anisotropy. Thus, the strength of the molecule-molecule and molecule-substrate interactions and hence the free energy of the system depend on the relative orientation of the ad-molecules. The growth and nucleation of organic molecules, therefore, is a delicate balance from such anisotropic strength of interactions between molecule-molecule and molecule-substrate. The following section will present a case study of the growth of a model organic molecule, pentacene, as well as the important growth parameters.

2.2.3   Pentacene Thin Film Growth

Pentacene ($C_{22}H_{14}$) is the benchmark organic semiconductor for organic thin-film devices. It is a planar molecule consisting of five linearly fused benzene rings, as depicted in Figure 2.7a. In the bulk phase, pentacene crystallizes in a triclinic structure (space group $P\bar{1}$) with two molecules per unit cell and the molecules are arranged in a herringbone packing motif like its lower homologues (Figure 2.7b and 2.7c). The interlayer distance for bulk pentacene is d_{001} = 14.1 Å.[43, 44]
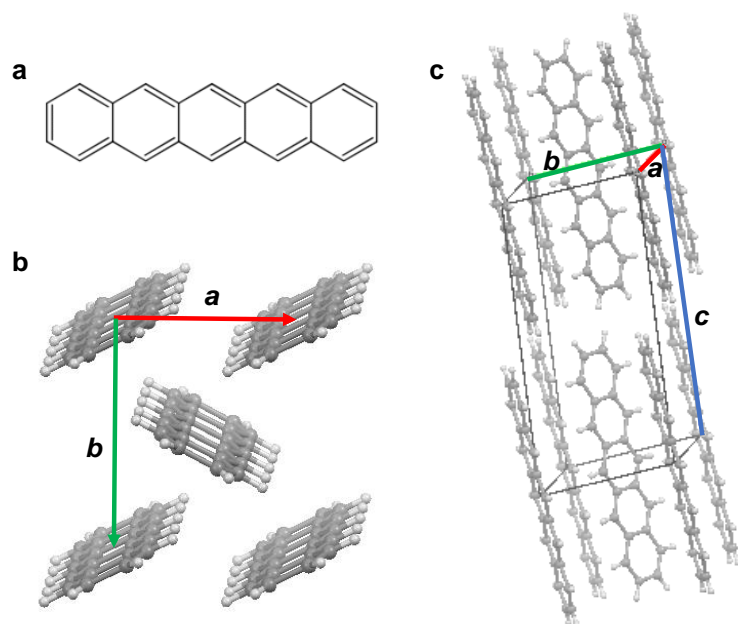
Figure 2.7 Pentacene molecular structure and bulk crystal structure.

Vacuum deposited pentacene films have different structures compared to the bulk crystals. Three "thin film" multilayer phases with different d_{001} values of 14.4, 15.0, and 15.4 Å have been identified by wide-angle X-ray diffraction, indicating different packing structures in the *a-b* plane.[45-47] Since understanding such structural differences is important for achieving high performing pentacene thin film devices, significant efforts have been made to investigate the growth mechanism of pentacene films that leads to different structures. There are several primary parameters that govern the growth and structure of pentacene films. The roles of substrate type, deposition rate, substrate temperature, and growth kinetics will be reviewed in the following.

Substrate Type. As introduced in the previous section, nucleation and growth of an anisotropic molecule like pentacene depends on the delicate balance between the

anisotropic strength of interactions between molecule-molecule and molecule-substrate. The nature of the substrate largely affects the pentacene-substrate interaction and thereby plays an important role in the morphology of pentacene first monolayer and subsequent layers. A large amount of experimental observations have been made to understand the general substrate effects.[48-51] For reactive substrates such as clean Si and metals, the interactions between pentacene molecule and the substrate are so strong that there could even be interfacial charge transfer. As a result, the pentacene molecules lie flat on the substrate. For flat and inert substrates including inorganic and organic dielectrics relevant to TFTs, pentacene-substrate interactions are much weaker than the interlayer pentacene-pentacene interactions. Therefore pentacene molecules tend to form a nearly vertically standing-up state on these substrates so that the (001) plane which has the lowest surface energy exposed. The "thin film phase" structure adopted in these films which differs that in the bulk has been an interesting research topic and fundamental understandings have been obtained with the aid of grazing incidence X-ray diffraction (GIXD).[52] In particular, the detailed monolayer structure of pentacene on SiO_2 has been determined. Unlike the "thin film phase" structures determined in relatively thick pentacene films which characterize slight tilt in the long molecular axis, pentacene molecules in the first monolayer stand vertically on SiO_2 surface. This unique "monolayer phase" structure is possibly stabilized by the minimized pentacene-substrate interaction or the large induced electrostatic polarization at the pentacene/SiO_2 interface. Since the "thin film phase" structures are substrate induced, it has been observed that the bulk phase sets in after the growth of certain critical thickness.

24

Substrate Temperature and Deposition Rate. As revealed by Equation 2.11 in the previous section, two important system variables that influence nucleation and growth are the substrate temperature (T_s) and the deposition rate (R, also equivalent to F). Simply speaking, increasing the substrate temperature and/or decreasing the deposition rate reduce the nucleation density and hence increase the grain size. However, in practical situations, some other factors need to be considered to interpret the role of substrate temperature and deposition rate, including the bulk phase nucleation, the surface diffusion, the dislocation assisted growth, and the thermodynamically conditions for layer growth, as shown in Figure 2.8. These factors essentially set the limitations for the substrate temperature and deposition rate for the formation of single-phase layered films.
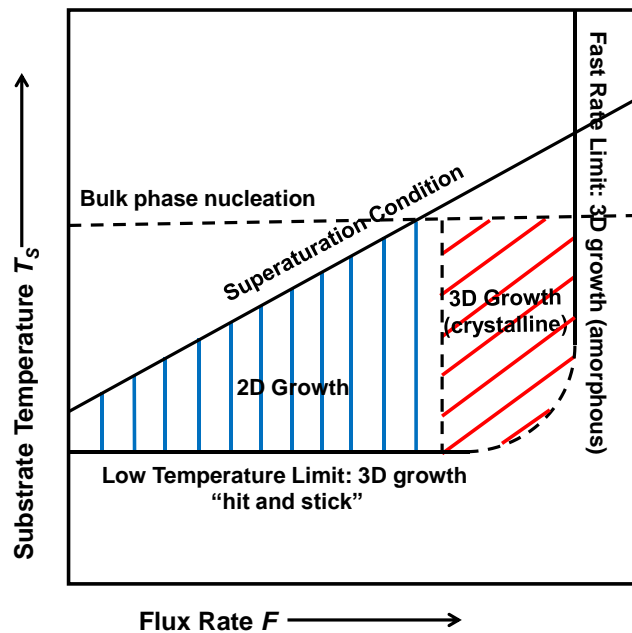
Figure 2.8 Role of deposition rate and substrate temperatures on layer growth.

25

As mentioned above, the bulk phase starts after certain critical thickness and it has been found that the critical thickness increases with decreasing substrate temperature. The deposition rate, however, is found irrelevant to the critical thickness for bulk phase formation. Therefore, according to Figure 2.8, the nucleation of the bulk phase sets the upper limit for the substrate temperature in order to obtain single-phase layered films. The lower limit for the substrate temperature, on the other hand, is set by the limit of surface diffusion. When the substrate temperature is low, hindered surface diffusion leads to amorphous films with very high nucleation density and poor film quality. Similarly, it has been shown that amorphous films also form when the deposition rate is too high. Another important limitation is the degree of super-saturation. At the low-saturation regime, i.e., high substrate temperature and low deposition rate, the nucleation rate for the formation of stable cluster is very low and thus the growth mainly occurs on step edges of dislocations. This so-called dislocation assisted will be introduced in more detail later in this section. In addition, the regime for the single-phase layer growth is further restricted by thermodynamic conditions. Primarily, the chemical potential between pentacene in vapor phase and in a stable homogeneous cluster should be negative.

Growth Kinetics. The kinetic rate equations introduced previously also indicate the importance of the energetic barriers for diffusion and reaction. It has been generally accepted that there are two different growth kinetic models depending on the competition between the diffusion and reaction processes, namely reaction-limited aggregation (RLA) and diffusion-limited aggregation (DLA).[53] A characteristic difference between films grown in these two different models is the film morphology.

26

In RLA, the energy barrier for aggregation is large ($E > k_bT$), resulting in very slow aggregation rate, i.e., the rate-limiting step. The clusters formed by reaction-limited aggregation have very dense and compact morphology as they can interpenetrate one another in a large degree. The aggregation, once happen, is very strong and rigid. In DLA, the energy barrier for aggregation is very small ($E \ll k_bT$) so that the aggregation rate is several orders of magnitude higher than reaction-limited aggregation. Therefore, the incoming molecules stick to existing clusters quickly and irreversibly and the aggregation is only limited by the diffusion of the molecules. There are four different stages for diffusion-limited aggregation. At stage I, the molecules diffuse around on an almost bare substrate until critical numbers of molecules meet and form a cluster. At stage II, the molecules still form new clusters while some of them start aggregating to the existing clusters. State III is called the aggregation stage when all incoming molecules aggregate to the existing clusters. Finally, at stage IV, the film coalesces. A general feature of films formed with diffusion-limited aggregation is their fractal morphology, in contrast to the compact films formed in reaction-limited aggregation. The fractal dimension (D_f) is used to quantify the complexity of the fractal pattern. D_f is around 1.7 for growth in DLA regime and about 2 for that in RLA regime.

Factors that determine whether the growth is in DLA regime or RLA regime include surface temperature, surface coverage, structural details, as well as the kinetic energy of the impinging molecules. The sticking coefficient (σ), a function of these factors, is therefore used to distinguish the two growth regimes. It is defined as the ratio of the number of molecules that stick to the surface to the total number of molecules impinging

27

on the surface. Clearly, the value of sticking coefficient is from 0 to 1, with 0 being that none of the molecules stick and 1 being that all the molecules stick. A true DLA growth ($\sigma = 1$) leads to very fractal islands, as shown in Figure 2.9a; whereas a RLA growth has σ close to 0, and compact clusters are formed, as shown in Figure 2.9c. An intermediate sticking coefficient ($0 < \sigma < 1$) thus leads to moderate DLA growth (Figure 2.9b), in which less fractal clusters are formed than those in a true DLA growth. It is found that pentacene films grown on SiO_2 is in DLA regime.
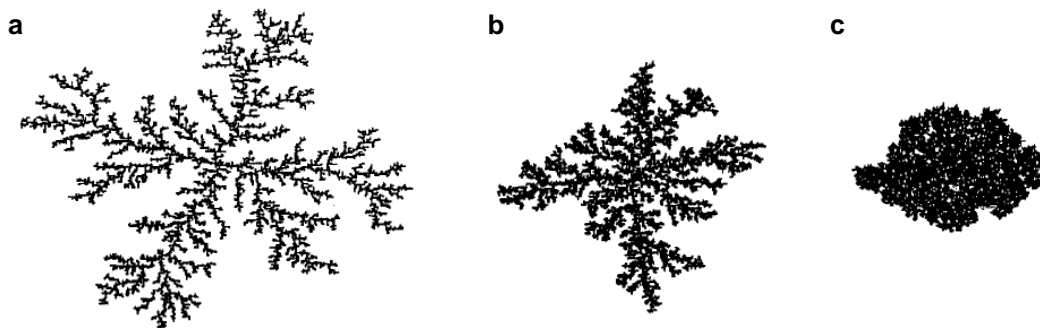
Figure 2.9 DLA and RLA of 10000 particles in two-dimensional space. [ref 53]
(a) True DLA ($\sigma = 1$; $D_f = 1.67$). (b) Moderate DLA ($\sigma = 0.1$; $D_f = 1.76$). (c) True RLA ($\sigma = 0.01$; $D_f = 1.93$).

2.3 Organic Single Crystals

Organic thin films, despite their importance for practical applications, are associated with structural imperfections (e.g., grain boundaries) and chemical impurities, which inhibit fundamental understandings of the intrinsic electronic properties in organic semiconductors. Organic single crystals, on the other hand, are perfect systems with high

material purity, excellent crystalline quality and nanoscale surface smoothness, which are of both fundamental and practical interests. In particular, organic single crystals provide an ideal platform for exploring the intrinsic charge transport characteristics and structure/property relationships. In this section, the methods of growing high quality organic single crystals will be introduced, and then the structural order and electrical properties of a model organic single crystal, i.e., rubrene, will be present in detail.

2.3.1   Growth Methods

In order to examine the intrinsic electronic properties of organic materials, field effect structures on the surface of free-standing organic single crystals have been adopted.[54-56] To fabricate such a single crystal OFETs, high quality organic single crystals with at least a few micrometers in size have to be formed directly on prepared surfaces. If structural determination is concerned, the size of the crystals needs to be at least several tens of micrometers. Thus, different methods have been developed to grow organic single crystals, including solution, gas-phase, and melt-growth methods.[57]

Solution growth methods are designed for organic molecules that are soluble in organic solvents over a range of temperatures and pressures. For highly soluble organic molecules, the most efficient way to grow organic single crystals in solution is to use the co-called "solvent evaporation method". In this method, a saturated solution of the organic molecules is uncovered to allow the solvent to evaporate. The resulting supersaturated solution then enables the organic molecules to spontaneously nucleate and grow into big crystals. For organic molecules with solubility that is moderate at room

temperature but changes significantly with temperature, another solution growth method named "slow cooling method" is adopted. In this case, the saturated solution is prepared in high temperature and as the temperature slowly decreases, the solution becomes supersaturated and the organic molecules spontaneously form nuclei and grow into large crystals. There are other solution growth methods according to the properties of the organic materials, e.g., the "vapor diffusing method", the "liquid-liquid diffusion method", etc. Table 2.2 summaries several major solution growth methods. The brief procedure, the properties of organic materials as well as examples of organic molecules are presented.

Table 2-2 Solution growth methods of organic single crystals. [ref 57]

Method	Brief Description	Examples
Solvent evaporation	Supersaturated solution forms when solvent evaporates. Seeds spontaneously form and grow into larger crystals.	poly(3-hexylthiophene) (P3HT)
Slow cooling	Seeds spontaneously form when hot saturated solution is cooled.	rubrene
Vapor diffusion	Volatile poor solvent evaporates and diffuses into the saturated solution, leading to an oversaturated solution. Seeds spontaneously form.	tetrathiafulvalene-tetracyanoquinodimethane (TTF-TCNQ)
Liquid–liquid diffusion	Low-solubility solvent diffuses into the high-solubility solvent layer, forming a saturated solution at the interface between the solvent layers.	Triisopropylsilylethyny pentacene (TIPS-pentacene)

The most commonly used growth method for organic single crystals is physical vapor transport (PVT)[58] since most organic molecules have low melting temperature and

low sublimation temperature. PVT combines the purification process of the organic materials and the growth of organic single crystals. Therefore, crystals with very high purity can be obtained by PVT. PVT can be performed in an open, closed, or semi-closed system.[57] PVT in an open system, which is the simplest and most widely used, will be introduced in the following.
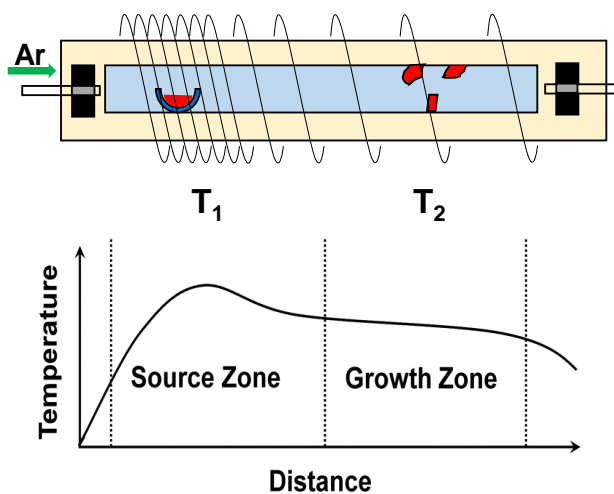
Figure 2.10 Crystal growth apparatus and different temperature zones.

A schematic of PVT in an open system is depicted in Figure 2.10. An inert gas is flowing in the open system of a horizontal tube reactor with different temperature zones. The source material is placed in the hottest region of the reactor and the crystal growth occurs within a narrow temperature range near the cold region of the reactor. Note that the organic single crystals and impurities deposit at different regions of the reactor because of their different molecular weights. The rate of sublimation, deposition, and crystal growth is controlled by the flow rate of the inert gas which also protects the

organic materials from oxidation. Typical inert gases used for PVT include H_2, Ar, and N_2.

The crystal growth in such a horizontal tube can be understood with a model proposed by Laudise et al.[58] The inert gas is assumed to be Poiseuille flow with a circular jet structure. A flow rate of 50 ml/min thus gives rise to a mean velocity of 12 cm/s and a maximum velocity of 24 cm/s for the jet exiting a 3 mm inlet tube. The maximum velocity (u_{max}) of the jet before it enters the source and growth zone is given by:

$$u_{max} = 3K'/8\pi vx \qquad\qquad\qquad \textbf{Equation 2.15}$$

where v is the kinematic viscosity of the gas, x is the distance from the inlet tube, and K' $= 4Q^2/3\pi a^2$ and is the kinematic momentum. K' is determined by experimental conditions as Q is the volume flow rate and a is the radius of the inlet tube. Therefore, u_{max} is affected by the experimental conditions as well as the properties of the carrier gas. Also, as the distance from the exit plane of the inlet tube increases, the maximum velocity of the jet decreases.

The distribution of velocity across the circular jet can be described by

$$\zeta = 0.244(K')^{1/2}r/(vx) \qquad\qquad\qquad \textbf{Equation 2.16}$$

where r is radial coordinate measured from the jet axis. ζ is a dimensionless parameter and has been used to estimate how the jet broadens as the jet travels to the downstream of the tube. As can be seen from the above equation, ζ decreases as x increases; that is, the jet broadens as the gas moves down the tube.

Two important factors that influence the quality of the crystals are the temperature and the inert gas flow rate. The sublimation temperature is usually set near the melting

point of the desired material, and the temperature gradient needs to be adjusted for a particular material. If very high purity crystals are desired, the temperature gradient needs to be sufficiently small (2-5 °C/cm). In terms of the flow rate, since it has been observed in several organic materials that the slower the growth process, the better the crystal quality, low flow rate is typically preferred.

In addition to the aforementioned solution and vapor growth methods, melt growth method can also be employed to grow some organic single crystals. However, typical melt growth approaches including Czochralski, Bridgman, or floating zone methods,[57] are more commonly used for growing large crystals of inorganic semiconductors because organic materials usually have high vapor pressure and chemical instability around their melting points. Examples of organic materials that have been grown by melt growth methods are those cheap and largely available ones including naphthalene, anthracene, tetracene, etc.

2.3.2 Rubrene Single Crystals

Among all organic materials, rubrene (5,6,11,12-tetraphenyltetracene) sets the performance standard for single crystal OFETs with reproducible intrinsic carrier mobility up to 20 $cm^2V^{-1}s^{-1}$ at room temperature.[33] Also, the carrier mobility in rubrene shows band-like temperature dependence. This section will briefly introduce some important properties of physical vapor transport grown rubrene single crystals, including the crystal structure and morphology, the band structure and transport properties, and the mechanical properties.

The molecular structure of rubrene is shown in Figure 2.11. PVT grown rubrene single crystals adopt an orthorhombic structure with four molecules per unit cell and lattice parameters of $a = 14.44$ Å, $b = 7.18$ Å and $c = 26.97$ Å.[59] Most of the crystals are shaped as elongated "lath", as shown in the optical micrograph in Figure 2.11e. The larger facets are parallel to the *a-b* plane and typical in-plane dimensions are around a few square millimeters for rubrene. The thickness of the crystals can vary over a wide range and is usually controlled by the length of the growth period. The lath-like crystal shape indicates that the growth rate in different crystallographic directions is anisotropic, which is a result of the anisotropy of intermolecular interactions. In general, the larger crystal dimension corresponds to the direction of the strongest interactions, i.e., the strongest overlap between π-orbitals of adjacent molecules. Therefore, the fastest growth direction of lath-like rubrene crystals also exhibits the highest field effect mobilities. The surface morphology of rubrene single crystals can be characterized by atomic force microscopy (AFM). Typical AFM images of pristine rubrene surfaces show flat terrace structures, as shown in Figure 2.11f. The width of the terraces varies from several micrometers to several tens of micrometers. The height of each terrace is around 13-14 Å, indicating that each terrace is a monomolecular step. Also, the terraces tend to be parallel to the fastest growth direction, or the π-stacking direction.
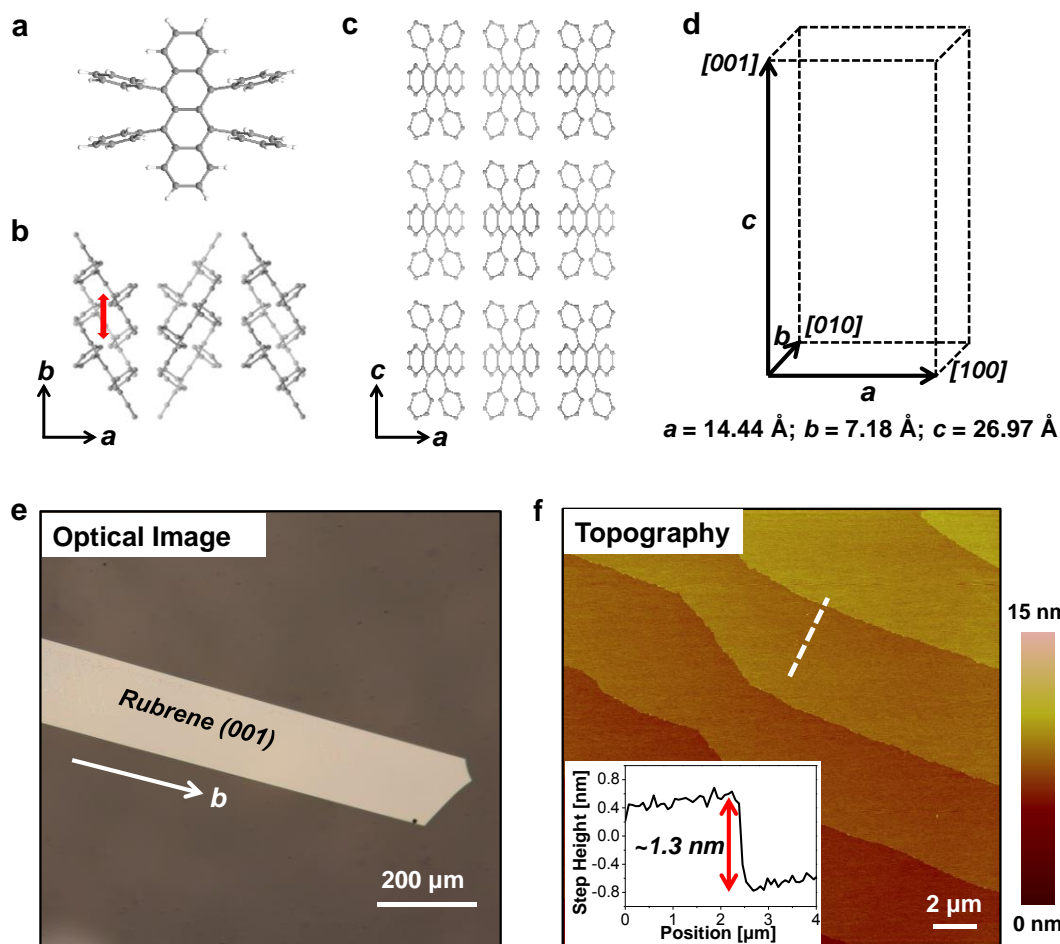
Figure 2.11 Crystal structure of rubrene single crystal.
(a)-(d) Crystal structure of rubrene. (e) Optical image of rubrene single crystal. (f) AFM topography of rubrene single crystal (001) face. Inset: step height profile of the white dashed line.

The origin of the excellent carrier mobilities and the significant mobility anisotropy in rubrene single crystals is believed to be the packing motif which gives rise to unique electronic coupling (Figure 2.11b-d). The electronic coupling between adjacent molecules, or the interchain transfer integral, t, is a key parameter to describe the band-like, intrinsic transport. The computation work carried out by Bredás et al.[60] found that larger transfer integrals in rubrene are along the b direction (π-stacking direction), which

lead to bandwidths of 340 and 160 meV for holes and electrons, respectively. They found that the smaller transfer integrals are along the diagonal directions of rubrene *a-b* plane. The transfer integrals found for all other directions are negligible.

To put the transfer integrals in the context of rubrene packing, we can see that the long molecular axes (the tetracene backbone) in rubrene are embedded in the *a-b* plane. Thus, the long molecular axes of adjacent molecules along the diagonal direction (the herringbone direction) are almost perpendicular. Therefore, the transfer integrals along the diagonal directions are smaller without efficient overlap. Along the *b* direction of rubrene, however, there is significant π-overlap between adjacent molecules with a stacking distance of 3.74 Å. Although this π-stacking distance is quite large, it leads to no displacement along the short molecular axes. The molecules along the *b* direction thus interact strongly with each other and larger transfer integrals are calculated in *b* direction. Along the *a* direction, the distance between adjacent molecules is 14.44 Å, which is too large for any electronic overlap. As a result, a charge carrier travelling along the *a* direction is expected to make its way through the diagonal direction and hence the transfer integral along the diagonal can be used to understand the transport along the *a* direction.

Chapter 3 Scanning Probe Microscopy

3.1 SPM overview

Scanning probe microscopy (SPM) is a family of probe-based surface characterization techniques that images surface features and near-surface physical properties at the length scales of 100 μm to sub-nanometers by sensing the forces between the probe and the sample. The field of SPM began emerging with the invention of scanning tunneling microscopy (STM) and atomic force microscopy (AFM) by Binnig et al. in the 1980's.[61, 62] The past few decades have witnessed a revolution of this field with the development of numerous advanced SPM techniques and novel applications.[63-66] The capabilities provided by SPM to interrogate and manipulate various materials properties at the atomic, molecular, and nanoscale in controlled environments have made SPM a versatile method in surface physics and chemistry, as well as nanoscience and nanotechnology. This chapter will present the fundamental physics, instrumentation, and practical applications of SPM. Particularly, several advanced SPM solutions for novel and improved materials characterization will be introduced in detail, including scanning Kelvin probe microscopy (SKPM), electrostatic force microscopy (EFM), friction force microscopy (FFM), and transverse shear microscopy (TSM).

3.1.1   Principle of SPM

In all SPM techniques, an image of the studied surface is constructed by measuring a local physical quantity related with the interactions between a sharp probe and the sample

surface. Different members of the SPM family differ in the nature of the physical phenomenon involved in the interactions, and hence various physical properties such as conductivity, static charge distribution, local friction, etc., can be measured. A generic SPM setup is shown in Figure 3.1. Before delving into the details of how a SPM works, the typical components of a microscope[67] are introduced below.
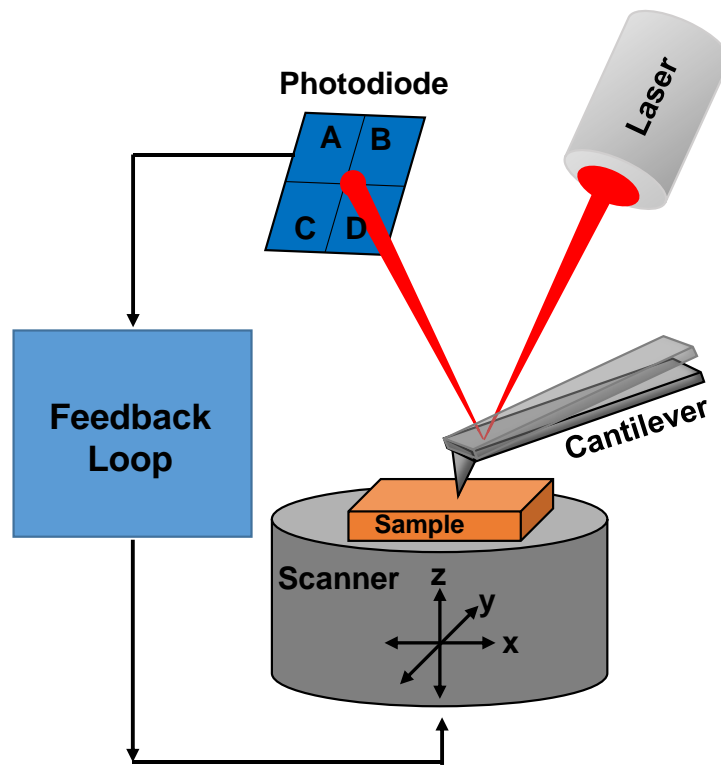
Figure 3.1 Scanning probe microscopy setup.

Piezoelectric Scanner. Piezoelectric scanners are critical elements in SPM. A piezoelectric scanner is made of piezoelectric ceramic materials that changes dimensions in response to an applied electric field and conversely accumulates charges when mechanical stress is applied. Typically, a piezoelectric scanner in SPM can move the sample in the *x*, *y*, and *z* directions using a single tube piezo. The lateral movements of

the scanner can range from tens of angstroms to over 100 microns. In the vertical direction, a piezoelectric scanner can distinguish height differences from sub-angstrom to about several microns. However, along with these essential properties are challenges associated with piezoelectric scanners, namely the xy-z cross-coupling, and the z nonlinearity. Since the unit cell of the crystalline piezoelectric material cannot expand or contract in one direction without changing the others, the movements in x, y, and z in a piezoelectric tube scanner are actually coupled. The cross-coupling between the xy directions and the z direction, in particular, is not programmable to be removed in typical piezoelectric scanners. Thus, the x-y motion can cause unwanted z motion resulting in distortion of the images. Also, the displacement of z is measured by the change of intrinsically nonlinear applied z bias, which is assumed linear. A false curvature of the measured surface is thus resulted.

    Probe. A SPM probe[68] is composed a free-swinging micro-cantilever and a sharp tip. Typical cantilevers are v-shaped or rectangular shaped. The dimensions of the cantilevers are on the scale of microns, usually several microns in thickness, several tens of microns in width, and a few hundreds of microns in length. The radius of the tip is usually on the scale of a few nanometers to a few tens of nanometers. Most SPM probes are made from silicon (Si) or silicon nitride (Si_3N_4). The tip is brought close to the sample surface during SPM operation, and the cantilever is deflected by the interaction. Therefore, two important parameters that characterize a probe are the force constant and the resonant frequency, which have to be chosen according to the particular sample and SPM mode. The surface of the tip can be modified by some conductive or magnetic coatings. Usually,

the back of the cantilever is also modified with reflective coatings in order to facilitate cantilever deflection detection, which will be described below.

Cantilever Deflection Detection. To detect the displacement of the cantilever, a laser beam based cantilever detection scheme is employed. The cantilever reflects the laser beam off it and the reflected laser spot is then displaced in a position sensitive photodetector when the cantilever deflects. As shown in Figure 3.1, the photodetector has four quadrants, each of which outputs a voltage proportional to the intensity of the laser impinging on it. The vertical and lateral displacements of the laser spot caused by the cantilever's deflection and twisting can thus be quantified by the vertical and horizontal differential output of the photodetector. Therefore, the normal and laterals forces due to the tip-surface interactions can be quantified.

Tip-Surface Interaction. The interaction forces between the tip and the sample are key to SPM operation. There can be very different forces dominating at different tip-sample distances[69] as depicted in Figure 3.2. During contact and the surface deformation by the tip, the elastic repulsion force dominates; this approximation is called the Hertz model. At tip-sample distances of the order of several tens of angstrom, the major interaction is the intermolecular interaction, i.e., the Van der Waals force. At the same distance between the tip and the sample and in the presence of liquid films, the interaction is influenced much by capillary and adhesion forces. At larger tip-sample distances, the electrostatic interaction starts to dominate. Depending on different tip-sample distance, there are different SPM imaging modes, namely the contact mode, non-contact mode, and intermittent contact mode.
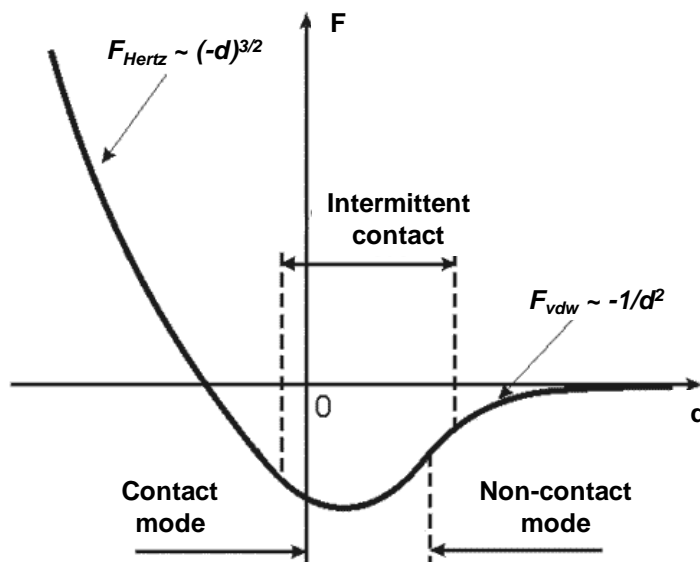
Figure 3.2 Tip-sample interaction. [http://www.ntmdt.com/spm-basics/view/probe-sample-interaction-potential]

With the knowledge of the major components in SPM, the basic operational mechanism of contact mode, for example, can be simply described as follows. A sharp tip integrated with a flexible cantilever is brought close to the surface of the sample. The force between the tip and the surface deflects the cantilever, and the deflection is quantified by a laser beam reflected from the cantilever surface into a split photodetector. The difference between the photodetector signal and the operator-specified set-point drives the feedback circuit to displace the piezoelectric scanner in z direction to null the difference. At the meantime, the piezoelectric scanner moves the sample under the tip in a raster fashion, resulting in a map of the z displacements for a two dimensional area.

41

3.1.2   Operational Modes

As mentioned previously, there are two distance regimes, i.e., contact regime and non-contact regime. The SPM imaging techniques can thus be categorized into contact mode and non-contact mode.[67, 70] The following section presents a detailed description of the two techniques.

Contact mode. Contact mode is also known as DC or quasistatic mode, where the tip makes soft physical contact with the sample surface. The contact force leads to the cantilever to deflect. The deflection of the cantilever (Δx) is proportional to the force (F) acting on the tip, according to Hook's law, $F = -k\Delta x$, where k is the spring constant. The probe used in contact mode is characterized with low spring constant, lower than the effective spring constant holding the atoms of the sample together.

The scenario of contact mode can be better understood with the aid of a force curve,[65] which is a plot of the cantilever deflection versus tip-sample distance. A schematic of a typical force curve is depicted in Figure 3.3. When the tip approaches from the far right side of the curve, where the separation between the tip and the surface is very large, the cantilever exhibits a constant deflection which is determined by the applied force and the spring constant of the cantilever. As the tip travels closer and closer to the surface and just prior to contact, the attractive force accelerates the tip to the surface, illustrated as the sudden increase of the cantilever deflection. After this so-called snap-to-contact, as the tip keeps approaching the surface, the cantilever bends up as depicted in Figure 3.3, and the force increases from 2 to 3. When the tip retracts, the force curve retracts itself. However, the contact is not broken until 4 is reached, where the

pulling force is large enough to snap the tip off the surface. The "stick" of the tip until 4 arises from the adhesion force between the tip and the surface. The adhesion force usually arises from the liquid meniscus layer developed at the sample-tip interface.
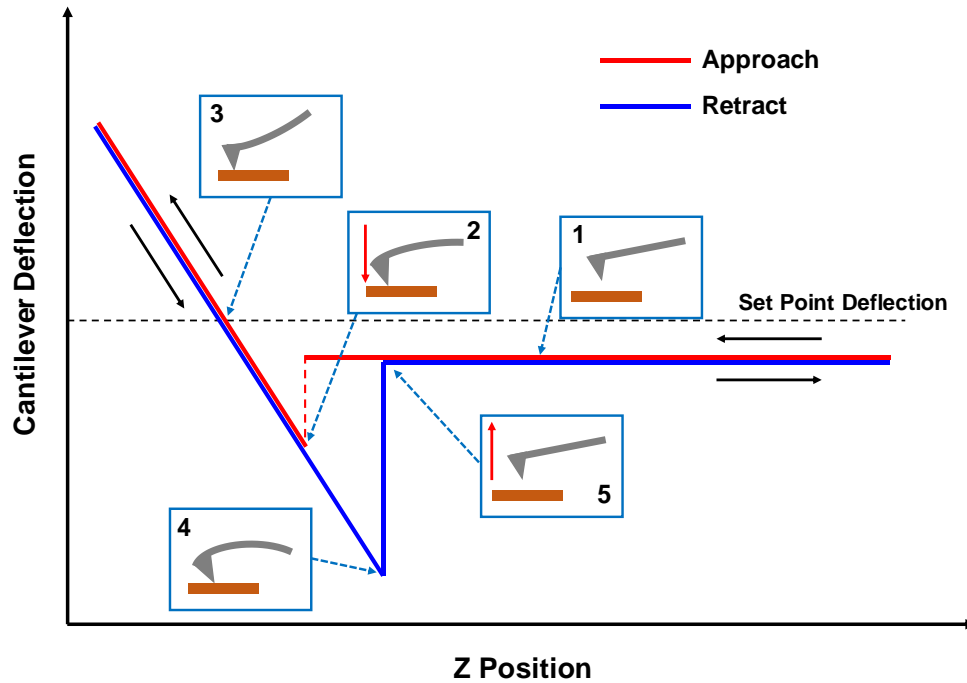
Figure 3.3 Force curve in contact mode AFM.

Contact mode can generate the topographic images in two modes, i.e., constant height mode and constant force mode. The former is typically used for obtaining tiny lattice resolution images. The height of the scanner is fixed so that the spatial variation of the cantilever deflection can be used to directly obtain the topographic data. In the latter, there is a user-defined deflection set-point (a fixed external applied load). Therefore, a constant degree of cantilever bending is maintained so that Z (either sample or tip) is displaced up and down as the tip travels over the hills and valleys of the surface. The

accuracy of how Z displacements trace the topography is determined mainly by the intrinsic speed of the feedback circuit, the user-selected gain settings, and the scan speed.

The drawback of contact mode is that the lateral force exerted on the sample can be quite high and can result in sample damage and/or the movement of relatively loosely attached objects. Therefore, a dynamic AC mode, also known as tapping mode, which oscillates the cantilever during imaging is more desirable as it has little or no contact with the surface and allows nondestructive imaging of soft samples.

Tapping mode. In tapping mode,[71] the cantilever is driven to oscillate at its natural resonance frequency. Thus, instead of being constantly dragged across the sample surface like in contact mode, the tip touches the surface only for a short time in each oscillation cycle. This effectively lessons sample damage that is otherwise common for contact mode. It also better preserves the tip, which is especially important when sample-to-sample comparisons are concerned. Tapping mode is the dominant imaging mode nowadays.
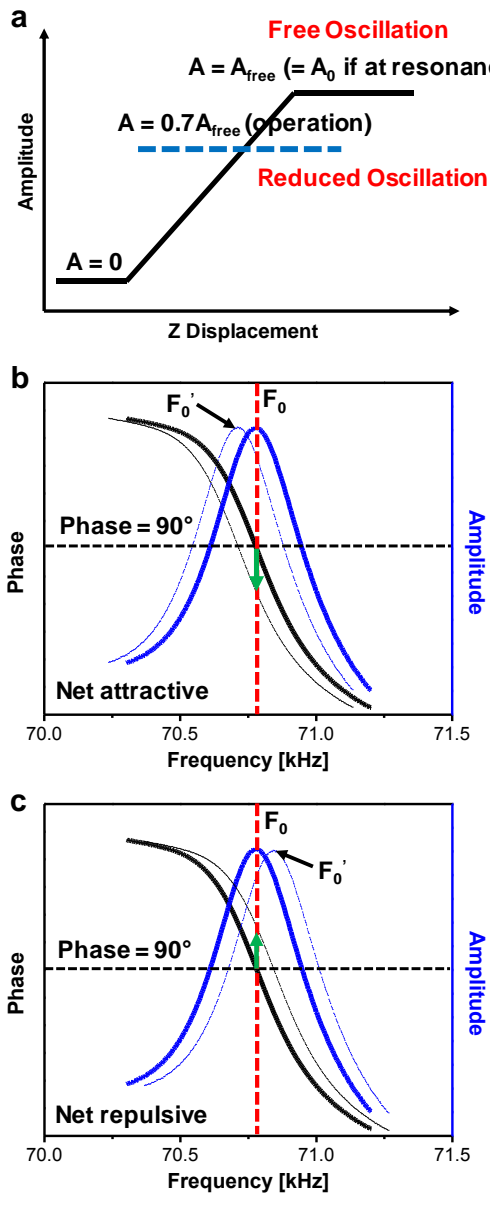
Figure 3.4 Tapping mode amplitude-Z curve and different operation regimes.
(a) Amplitude-Z curve for tapping mode. (b) Impact of net attractive force on the resonant response. (c). Impact of net repulsive force on the resonant response.

Like contact mode, tapping mode can also be understood from the force-distance behavior, but in this case, the "force curve" plots the tip amplitude versus the Z displacement as shown in Figure 3.4a. Before tip approaching, the cantilever oscillates

close to its resonant frequency, and hence the amplitude is equal to the free amplitude (A = A_{free}). As the tip approaches the sample surface, the amplitude is reduced ($A < A_{free}$) due to the force gradients acting on the cantilever including van der Waals force, dipole-dipole interaction, etc., and damping. The amplitude is smaller as the tip is closer to the surface. Similar to contact mode, a user-defined set-point (amplitude) is employed. Instead of amplitude set-point in raw units of Volt, a more meaningful setting is to use the ratio of the set-point amplitude to the free amplitude. When the tip scans across the sample surface, a feedback circuit detects the deviation of the measured amplitude from the set-point amplitude and moves Z up and down to maintain a constant amplitude ratio.

Although force is not directly measured in tapping mode, the nature of the force, whether it is purely attractive or combination, can be used to divide tapping mode into two dynamic interaction regimes. The impact of attractive and repulsive forces on the frequency-dependent resonant response is described in Figure 3.4b and 3.4c. When only attractive force is encountered as the tip oscillates towards and away from the surface, it reduces the effective spring constant (k) of the cantilever since the attractive force is opposite to the restoring force of the cantilever. The resonance frequency (F_0) is thus reduced because F_0 is proportional to the square of k. Therefore, the resonant response curves shifts to the left with net attractive force as shown in Figure 3.4b, and vice versa. Such resonant response shifts necessarily result in a reduced amplitude at the original resonant frequency F_0, which is the key to the instrument operation. Note in actual images, one can use the sign of phase lag to diagnostically determine whether it is net

attractive or net repulsive because phase shifts have different signs for net attractive and net repulsive.

Based on the different interactions between the tip and the sample, more and more advanced SPM techniques that explore different materials properties have been developed. Techniques based on both contact mode and tapping mode will be discussed in the following.

3.2 Lateral Force Microscopy

As mentioned above, the normal force during contact mode is accompanied by large lateral force. The normal force, which gives rise to the deflection of the cantilever in the vertical direction, is used to drive a feedback circuit that generates the topographic information of the sample surface. The lateral force, which causes cantilever deflection in the direction parallel to the surface plane (cantilever twisting), can be measured with lateral force microscopy (LFM). Conventional LFM images the friction forces arising from tip-sample interactions and is thus referred to as friction force microscopy (FFM). Since friction force is very sensitive to the materials composition, FFM can be used to identify materials inhomogeneity at sample surface. Recently, a novel variant of LFM, termed as transverse shear microscopy (TSM), has been developed. It detects the lateral shear forces particular to the tip motion and is sensitive to a tensor shear modulus of the surface material. This section will give a brief introduction to the operational principles and applications of FFM and TSM.

47

3.2.1   Friction Force Microscopy

FFM, a conventional form of LFM, measures the sliding frictional force applied to the cantilever when it moves horizontally across the sample surface in contact mode.[72] The fast scan direction in FFM is perpendicular to the long axis of the cantilever. When there are changes of the surface friction and/or the slope of the surface, the frictional force exerts a torque on the tip, causing twist of the cantilever, as illustrated in Figure 3.5. Therefore, by measuring the lateral cantilever deflection (friction), FFM is capable of detecting the inhomogeneous compositions of the sample surface, as well as imaging edges of abruptly changing slopes at the sample surface.
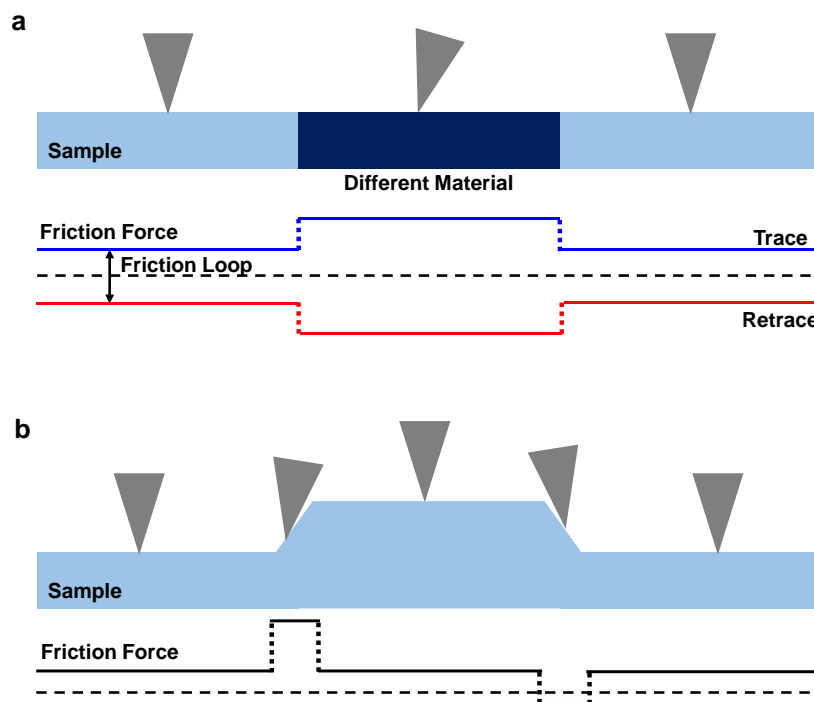
Figure 3.5 Cantilever twisting in FFM and friction.
(a) Contrast caused by change in surface friction. Friction shows scan-direction dependence. The total friction is given by the height of the friction loop. (b) Contrast caused by change in surface topography. Total friction is shown.

In the case where there is difference in the surface composition but the change in surface slope is absent, FFM measures the dissipative frictional force. As depicted in Figure 3.5a, the cantilever may experience larger friction in some areas, leading to larger cantilever twist. The magnitude of the friction, under a constant normal force, is proportional to the frictional coefficient (μ) of the surface material, according to equation, $F = \mu F_{norm}$. In a second case, where there is only change in the surface slope, the cantilever may twist when it encounters steeper slopes, as illustrated in Figure 3.5b. Clearly, the slope produces an off-vertical normal force at the tip-sample contact, whose lateral component contributes to the total lateral force. Therefore, different lateral deflections are expected when the tip scans up and down hill. The lateral twist of the cantilever is detected by a position sensitive photodetector. As introduced above, the photodetector is composed of four quadrants, which are denoted as A, B, C, and D, in Figure 3.1. The lateral signal can thus be expressed by the difference in the signals recorded in the right cells (B + D) and the left cells (A + C); that is, the friction is given by (B + D) - (A + C).

Note that the twist of the cantilever is also dependent on the scan direction since frictional force is exerted in the opposite direction as the relative tip-sample motion. Thus, the frictional force twists the cantilever towards right when the cantilever moves from left to right; whereas, the cantilever twist is towards left when the relative motion between tip and sample is from right to left. As a result of the scan direction dependence of the cantilever twist, there is a so-called "friction loop" as friction data are acquired in

49

both scan directions (trace and retrace). The height of the friction loop, as indicated in Figure 3.5a, is typically used to quantify the magnitude of the friction.

Macroscopically, friction between sliding bodies can be viewed as collective and interdependent mechanical behavior of a multitude of small contacts between shearing surfaces which are constantly formed, deformed, and ruptured.[73] Fundamental understanding of the sliding friction is difficult due to the complexity of the tribological processes. Thus, atomic friction experiments, which measure the forces involved in the sliding of single asperity contact, have been carried out to provide the atomistic picture of friction. By sliding a sharp tip over an atomically flat surface, the sliding is found to adopt an atomic "stick-slip" movement with the same periodicity as the atomic lattice. There are preferred atomic positions for the tip and the lateral force arises when the tip is not above one of the preferred positions. Thus, when the tip is sliding over the surface, the tip will be stuck to a preferred lattice site until the lateral force becomes large enough for the tip to jump to the next preferred position.
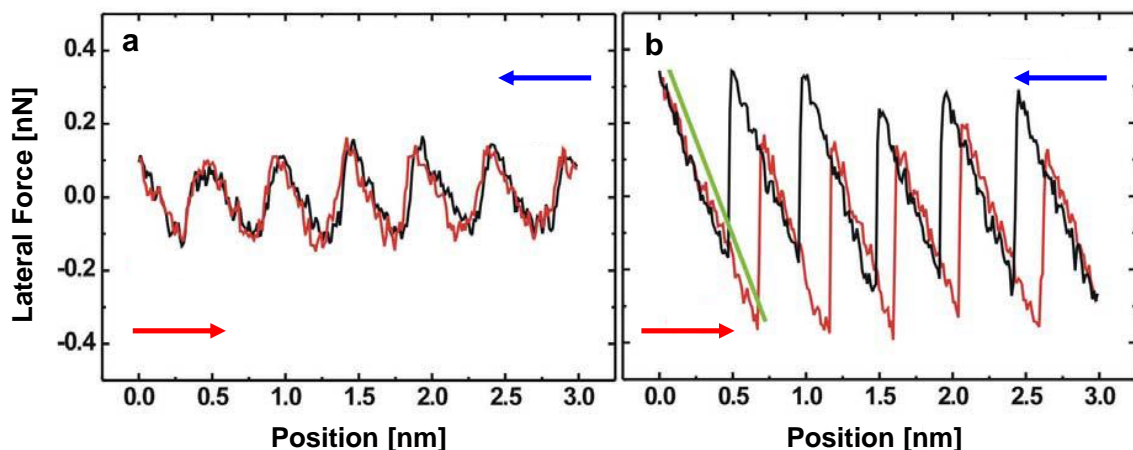
Figure 3.6 Friction measurements over a NaCl (100) surface. [ref 74]
(a) Normal load is negative to compensate the adhesive force between the tip and surface. (b) Small normal load is applied. Atomic stick-slip behavior is demonstrated as the saw tooth-shaped friction signal. Hysteresis between forward and reverse scan quantifies the energy dissipation. The green bar is equivalent to the effective stiffness of the system.

Figure 3.6 shows the lateral force measured when the tip scans over a NaCl (100) surface in trace and retrace.[74] A small normal load is applied in this case. As can be seen, atomic stick-slip behavior gives rise to saw tooth-shaped lateral force signals. Note that there is a hysteresis between trace and retrace, which reflects energy dissipation in the process. Therefore, friction between two sliding bodies is related to energy dissipation and the rise in dissipation can be corresponded directly to the mechanical instabilities on the atomic scale.

FFM has resulted in many interesting applications due to its material and chemical sensitivity, as well as the sensitivity to molecular arrangements and to local structural disorder.[75-82] Figure 3.7 shows an example when FFM can be used to determine the compositions of mixed monolayer systems.[77]

51
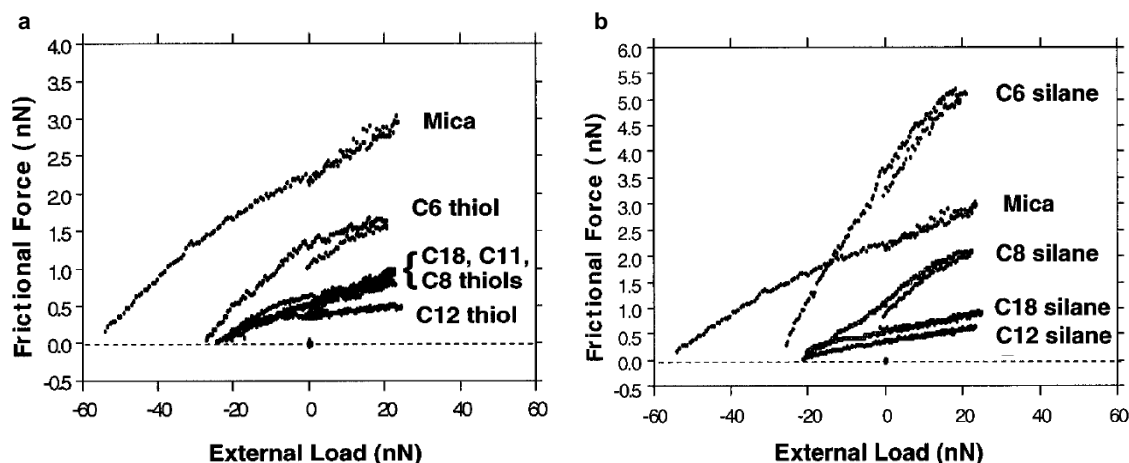
Figure 3.7 Friction as a function load for alkanethiol monolayers on Au and alkylsilane monolayers on mica. [ref 77]

Friction as a function of load curves are measured on the alkanethiol (CH_3-$(CH_2)_{n-1}$-SH, n = 18, 11, 12, 8, 6) monolayers self-assembled on Au and alkylsilane (CH_3-$(CH_2)_{n-1}$-$SiCl_3$) monolayers self-assembled on mica with the same Si_3N_4 tip. The friction curve of freshly cleaved mica is used as the reference. For the alkanethiol monolayers (Figure 3.7a), the friction curves for the C18, C11, and C8 layers are very similar. The curve for the C12 layer lies below all other curves, and the frictional forces for the C6 layer are roughly twice as large. All curves lie below the curve for mica. For the alkylsilane monolayers (Figure 3.7b), C18 and C12 layers show the lowest friction and C8 and C6 layers exhibit the higher friction. The frictional forces for the C6 layer are much larger than those for C8, C18 and C12, and are also larger than that for mica on high loads.

The differences in the frictional forces can be understood by the structural orders of the self-assembled monolayers. For example, the alkanethiol monolayers with n = 18, 12, 11, and 8 are densely packed and well-ordered, whereas no order was observed on the C6

52

layers. Also, when going from a thiol to a silane anchor, disorder increases and thus the silanes exhibit larger friction than the thiols. As a result, the different self-assembled monolayers can be distinguished by friction forces in spite of the identical methyl terminal groups and similar surface energy of these films.

3.2.2   Transverse Shear Microscopy

TSM, a novel variant of LFM, measures a different lateral force than sliding friction, that is, the transverse shear. The operational difference between FFM and TSM lies in the angle between the scan direction and the cantilever long axis (Figure 3.8). In TSM, the tip scans over the surface in a direction parallel to the cantilever long axis so that the lateral torque of the cantilever only originates from the transverse shear, as shown in Figure 3.8a. Work by Last et al.,[83] Puntambekar et al.,[84] and Kalihari et al.[85, 86] have demonstrated TSM as a powerful tool to identify the crystallographic orientation of the sample surface.
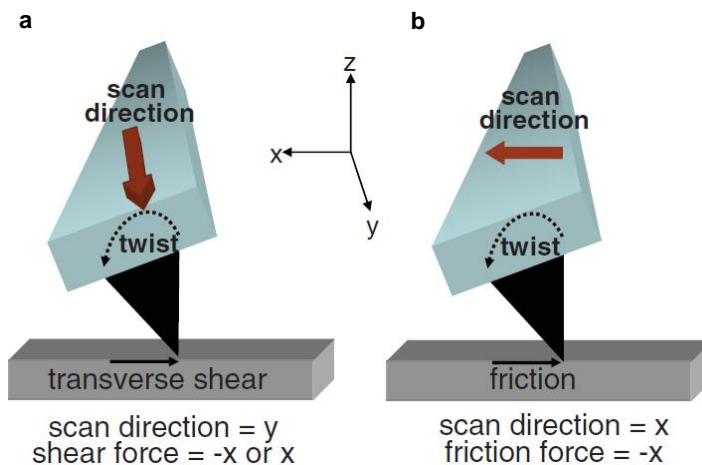
Figure 3.8 Scan direction, cantilever torque, and lateral force of TSM and FFM. [ref 86]

53

Kalihari et al.[85, 86] first reported detailed investigations on the tip-sample shear interactions and the contrast mechanism of TSM by comparing the tip velocity and the temperature dependence of the cantilever twist in TSM and FFM. Key findings of this work are summarized below:

1. TSM signal (trace - retrace) can be either positive or negative whereas the frictional force measured in FFM is always positive. This is because in TSM, the trace scan can result in either clockwise or counter-clock twist and the retrace scan results in the opposite twist. The TSM signal (proportional to trace minus retrace scan) is therefore either positive or negative. However, in FFM, the trace scan always induces a clockwise twist of the cantilever and the retrace scan always induces a counter-clockwise twist. This gives rise to friction signal that is always positive.

2. Transverse shear response is non-activated while friction response is activated. As shown in Figure 3.9d, TSM signal at room temperature is completely independent of the tip velocity. However, friction signal shows a logarithmical increase with velocity at lower velocities due to thermally activated motion of the contact atoms (Figure 3.9b). Friction becomes constant only when the velocities are high enough so that thermal activation ceases to be relevant. Also, at constant tip velocity, increasing the sample temperature decreases the friction loop height while the TSM loop height remains the same (Figure 3.9a and 3.9b).
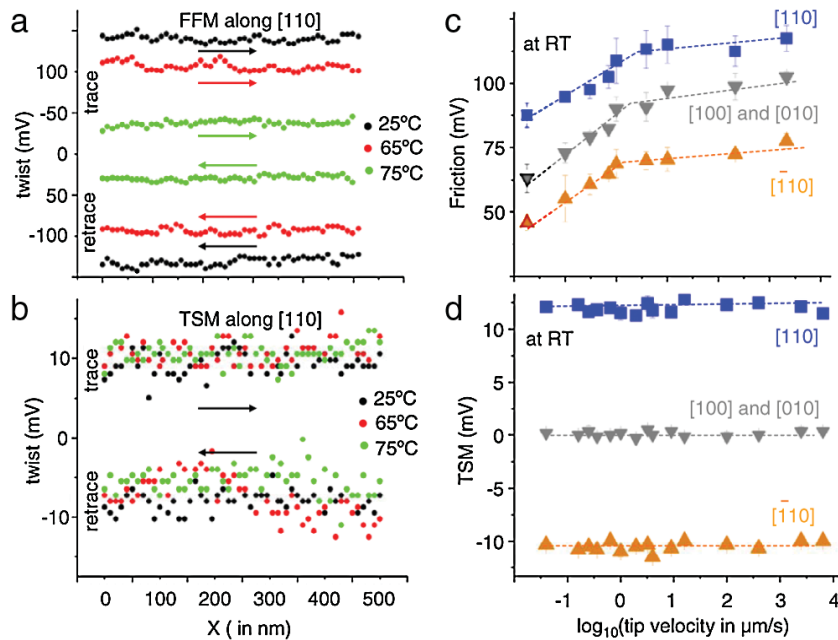
Figure 3.9 Friction and TSM measurements of pentacene. [ref 86]
(a) FFM of pentacene at different temperatures along [110] direction. Friction force is proportional to trace minus retrace. (b) TSM of at different temperatures along [110] direction. (c) Tip velocity dependent friction signal at room temperature. (d) Tip velocity dependent TSM signal at room temperature.

3. TSM signal is related to elastic deformation at the tip-sample interface, which is determined by the in-plane elastic modulus of the surface material. Thus, for materials with elastic anisotropy, TSM contrast shows a crystallographic dependence. Friction, on the other hand, is dominated by the activated, stick-slip behavior, and the effect of elastic deformation is hence largely masked.

Overall, TSM minimizes the torque caused by the activated, stick-slip phenomena as in FFM by scanning the sample in a direction parallel to the long axis of the cantilever. It is therefore sensitive to the elastic deformation at the tip-sample interface, affording the capability of imaging elastic anisotropy at high resolution.

55

3.3 Scanning Kelvin Probe Microscopy and Electrostatic Force Microscopy

Scanning Kelvin probe microscopy (SKPM) and electrostatic force microscopy (EFM) are another two important members in the SPM family. By imaging the surface potential via the Coulomb interactions with high spatial resolution, SKPM and EFM provide two main workhorses for local probing of electrical properties at various organic semiconductor surfaces and interfaces. Moreover, the simultaneously obtained topography data along with the highly resolved electrical and electronic information in both SKPM and EFM allow the examination of structure-property relationships which are central in the Materials Science of organic semiconductors. As a result, SKPM and EFM have been used extensively in the field of organic electronics for characterization of the nanoscale electrical properties at surfaces and interfaces of organic semiconductors.[23, 25, 63, 87-92] The non-invasive nature of SKPM and EFM also enables the investigations of active organic electronics devices.[26, 93-96] In this section, several key technical aspects of SKPM and EFM directly related to their important scientific applications will be introduced, including the instrumentation, the working principles, and the sensitivity/resolution.

3.3.1　Operation Mechanism of SKPM

SKPM, also known as Kelvin probe force microscope (KPFM), was first developed by Nonnenmacher et al.[97] and Weaver et al.[98] It allows to image surface electronic properties, namely the contact potential difference (CPD).[99] The name "Kelvin probe" originates from the macroscopic method developed by Lord Kelvin in 1898 using a parallel capacitor arrangement to explain the formation of built-in CPDs in metals.[100]

An important concept involved in this phenomenon is the work function (Φ), which, simply put, is the minimal energy needed to remove an electron from the electronic ground state in a given material. In metals, Φ is usually defined as the difference in energy between an electron at the vacuum level and that at the Fermi level of the metals. In semiconductors or insulators, Φ can be regarded as the difference in energy between the vacuum level and the most loosely bound electrons inside the solid. When two plates of a capacitor composed of materials with different Φ are electronically connected, electrons flow from the plate with low work function (Φ_1) to that with high work function (Φ_2) until Fermi levels of the two materials reach equilibrium, as shown in Figure 3.10. As a result of the electron transfer, opposite charges are generated on the capacitor, which creates an electric field between the two capacitor plates and a gradient in the vacuum level E_{vac}. The local drop of vacuum level across the gap is thus referred to the CPD and it is equal to the work function difference between two materials. Since the electric field can be easily detected, an external bias (V_c) can be applied to null the electric field as shown in Figure 3.10. At equilibrium, the electric field is zero and V_c is equal and opposite to the CPD, which equals the work function difference between the two

materials. Therefore, with a reference plate (known Φ_1), the work function of the other

plate (Φ_2) can be easily calculated with

$$\Phi_2 \;=\; \Phi_1 - qV_c \qquad\qquad \textbf{Equation 3.1}$$

where q is the elementary charge. This method can therefore be used to determine the

work function of different materials.
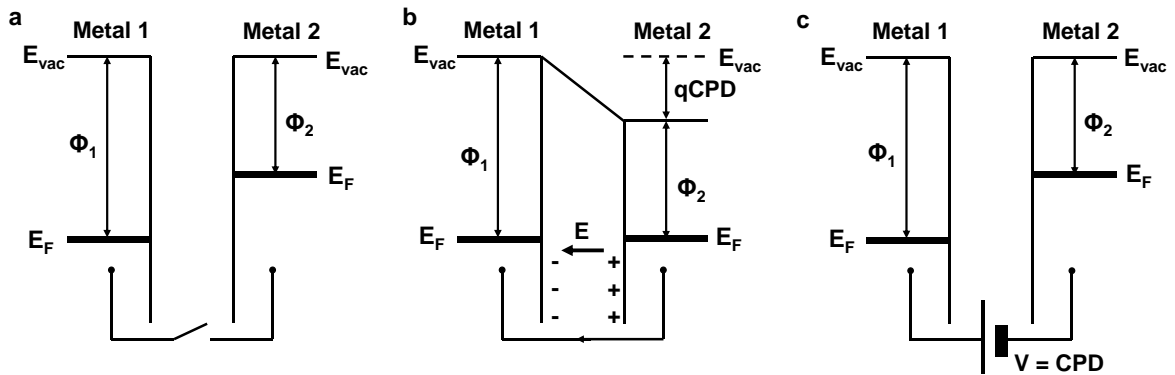
Figure 3.10 Schematic of the Kelvin probe method.
(a) Two metals with different work functions, Φ_1 and Φ_2. (b) When the two metals are electrically connected, Fermi level align, leading to a contact potential difference and an electric field between the two materials. (c) An external potential equal to CPD is applied to remove the electric field.

The Kelvin probe method was later optimized by Zisman,[101] who adopted a vibrating

reference surface instead of a stationary reference. Since the oscillation of the reference

plate induces change of the capacitance (C) and hence the voltage at the reference, a

small alternating current is induced, and is given by:

$$I = (V_c + V_{CPD})\,\frac{dC}{dt} \qquad\qquad \textbf{Equation 3.2}$$

where V_c is applied between the two plates until the current goes to zero such that

$V_c = -V_{CPD}$. Although the Kelvin probe method provides high electrical resolution, the

measured Φ is an average of the local work functions over the entire plate (or probe) surface which typically ranges from several tens of micrometers to several millimeters. It is therefore impossible to discern any local variations of the work function by Kelvin probe.

SKPM shares similar principle with the Kelvin Probe. However, by replacing the reference plate with a very sharp tip (several tens of nanometers), SKPM allows the measurement of Φ with high spatial and electrical resolution. Also, instead of measuring current as in traditional Kelvin probe method, SKPM detects the electrostatic force that is directly related to the electric field. This is because the reduction of capacitor plate size (from a macroscopic plate to the apex of a sharp tip) greatly suppresses current generation and leads to poor sensitivity.
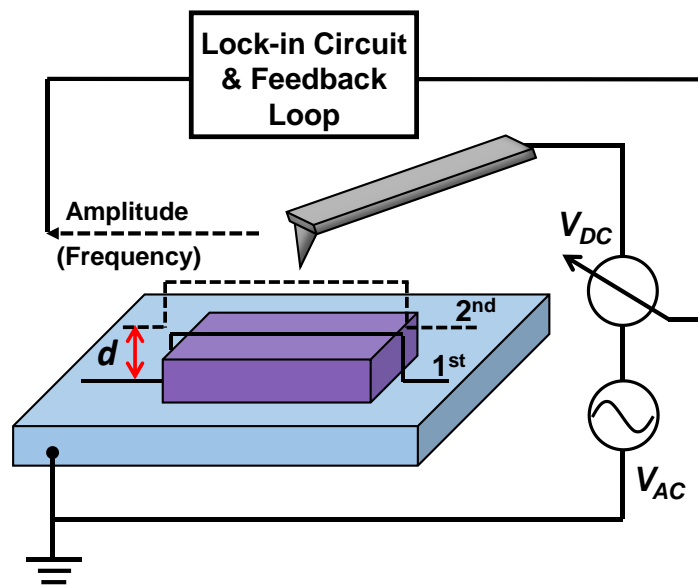
Figure 3.11 Schematic of scanning Kelvin probe microscopy.

A typical two-pass (or lift mode) SKPM setup is shown in Figure 3.11. In the first pass, a conductive tip scans the sample surface in normal tapping mode to obtain the topographic data. The tip is then lifted a constant height (d) above the topography such that the tip only interacts electrostatically with the sample surface, i.e., the short range van der Waals interaction is eliminated. Importantly, in the second pass, the mechanical oscillation is turned off and an alternating external bias (V_{AC}) at frequency ω, as well as a DC bias (V_{DC}) is applied to the tip. Therefore, the voltage (ΔV) between the tip and the sample is given by:

$$\Delta V = -V_{DC} + V_{CPD} + V_{AC}\sin(\omega t)$$

Equation 3.3

Thus, with the energy of a parallel plate capacitor $U = \frac{1}{2}C\Delta V^2$, the electrostatic force exerted on the tip due to the electric field can be written as:

$$F = -\frac{dU}{dz} = -\frac{1}{2}\frac{dC}{dz}\Delta V^2 = F_{DC} + F_\omega + F_{2\omega}$$

Equation 3.4

where the spectral components are

$$F_{DC} = -\frac{1}{2}\frac{dC}{dz}\left((V_{CPD} - V_{DC})^2 + \frac{1}{2}V_{AC}^2\right)$$

Equation 3.5

$$F_\omega = -\frac{dC}{dz}(V_{CPD} - V_{DC})V_{AC}\sin(\omega t)$$

Equation 3.6

$$F_{2\omega} = -\frac{1}{4}\frac{dC}{dz}V_{AC}^2\cos(2\omega t)$$

Equation 3.7

Here, the ω component of the electrostatic interaction is used to measure the CPD. As can be see, when F_ω is zero, V_{DC} is equal to V_{CPD}. Therefore, a two-dimensional CPD map can be obtained by recording V_{DC} at each pixel as the tip raster scans the surface. The CPD, which is equal to the work function difference between the tip and the sample, can

60

be used to determine the work function of the sample given that the tip work function is known. As mentioned above, the sharp tip employed in a SKPM setup affords SKPM the capability of imaging subtle variations of work function in high spatial resolution. More details about the sensitivity and resolution of SKPM will be discussed later in this chapter.

3.3.2 Operation Mechanism of EFM

EFM is another important electrical characterization technique and shares very similar principles with SKPM. As described above, SKPM uses an external DC bias to compensate the electric field and thus to directly measure the CPD. EFM, on the other hand, does not compensate the electric field; instead, it directly records the electrostatic force gradients and frequency shifts. Therefore, EFM is simpler and higher imaging speed can be achieved by avoiding the DC feedback loop. Also, higher spatial resolution can be achieved by EFM.[102] However, such advantages of EFM also come with a major drawback, i.e., the lack of quantitative measurement of CPD.

The setup of a typical two-pass EFM is depicted in Figure 3.12. As in SKPM, the topography is scanned in the first pass and the second pass is performed at a constant distance above the topographic trajectory so that there is only long-range electrostatic interaction between the tip and the sample. However, unlike in SKPM, the tip is still mechanically oscillating in the second pass and a constant DC bias (V_{DC}) is applied to the tip. The oscillating frequency shift of the cantilever ($\Delta\omega$) or the phase lag ($\Delta\varphi$), arising from the electrostatic force gradient, is recorded.
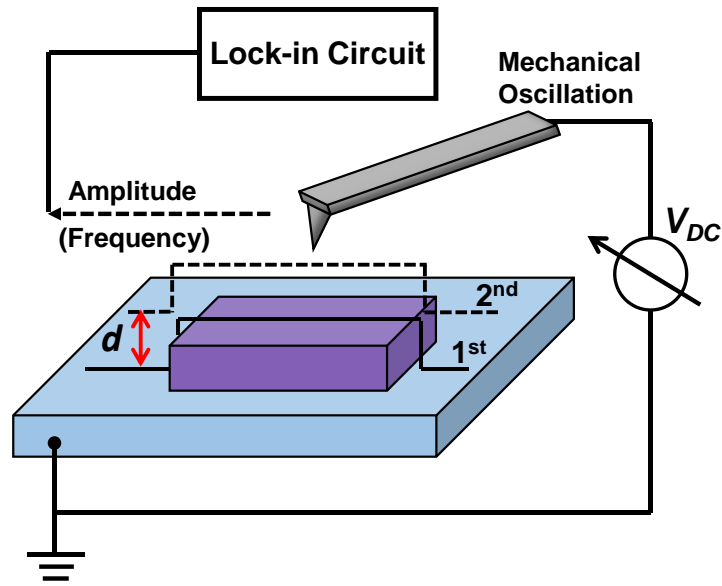
Figure 3.12 Schematic of electrostatic force microscopy.

The frequency shift and the phase lag can be written as

$$\Delta\omega = -\frac{\omega_0}{2k}\frac{dF}{dz}$$ **Equation 3.8**

$$\Delta\varphi = -\frac{Q}{k}\frac{dF}{dz}$$ **Equation 3.9**

where ω_0 is the resonant frequency, k is the spring constant, and Q is the quality factor of the cantilever, which is defined as the ratio of energy stored in the cantilever to the energy supplied by a generator per cycle to keep signal amplitude constant at the resonant frequency.

Recall that the electrostatic force (F) is a function of the first order gradient of the tip-sample capacitance, as well as the voltage difference between the tip and the sample. Therefore, the frequency shift and the phase lag as a result of the electrostatic force can be rewritten as

$$\Delta\omega = \frac{\omega_0}{4k}\frac{d^2C}{dz^2}(V_{DC} - V_{CPD})^2 \qquad\qquad \textbf{Equation 3.10}$$

$$\Delta\varphi = \frac{Q}{2k}\frac{d^2C}{dz^2}(V_{DC} - V_{CPD})^2 \qquad\qquad \textbf{Equation 3.11}$$
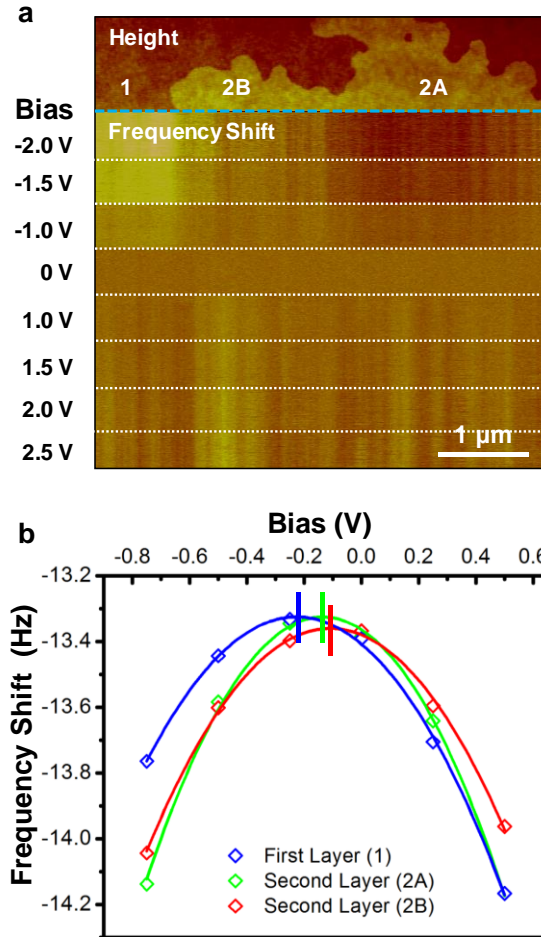
Figure 3.13 Determination of the CPDs in different domains of pentacene bi-layers by EFM frequency shifts at different applied biases.
(a) EFM frequency shift image of pentacene bi-layer at biases from -2V to 2.5 V. (b) Plot of EFM frequency shift as a function of tip bias for the three different domains. The peaks of the parabolas indicate the CPDs of the different domains.

Clearly, both the frequency shift and the phase lag are sensitive to the CPD with a parabolic dependence. Therefore, by measuring $\Delta\omega$ (or $\Delta\varphi$) at a number of different DC biases (V_{DC}) and plotting $\Delta\omega$ (or $\Delta\varphi$) as a function of V_{DC}, the CPD can be obtained as the voltage at the vertex of the parabola, as illustrated in Figure 3.13. A comparison between SKPM and EFM is summarized in Table 3.1.

Table 3-1 Comparison of operation mechanism between SKPM and EFM.

SKPM	EFM
Conductive Tip, Non-contact Mode	Conductive Tip, Non-contact Mode
Electrostatic Interactions	Electrostatic Interactions
AC Bias + DC Feedback Applied	Constant DC Bias Applied
Electrostatic Force Detected ($\sim dC/dz$)	Electrostatic Force Gradient Detected ($\sim d^2C/dz^2$)
Surface Potential Recorded	Frequency Shift/Phase Lag Recorded
Direct CPD Measurement	Indirect CPD Measurement

3.3.3   Sensitivity and Resolution

Both SKPM and EFM are always performed in non-contact AC mode, in which the tip oscillates with respect to the sample, such that a superior signal-to noise ratio can be achieved. However, there are also some factors that limit the sensitivity and resolution of SKPM and EFM, including the capacitive convolution and surface contaminations, as will be discussed in this following.

First of all, it is important to note that instead of the simple capacitor model introduced above that considers electrostatic interactions only between the sample and the nanometer-sized region under the tip apex, the real interactions in a SKPM/EFM system is more extensive. The electrostatic forces between the overall probe and the surface can be contributed by the capacitive coupling from the surface to the cantilever and the tip cone, as well as the tip apex.[103] This is because the electrostatic interaction has a long-range character. Therefore, the cantilever, for example, contributes strongly to the total force although it is relatively far away from the sample surface. To understand the electrostatic interaction in a complex tip-sample system, a theoretical approach was proposed by Colchero et al.,[104] in which the corresponding interaction between the surface and three basic units of the probe, i.e., a macroscopic cantilever, a mesoscopic tip cone, and a noanometric tip apex was analyzed. They found that each of the units makes different contribution to the total electrostatic force due to their specific geometry and position with respect to the sample surface. Therefore, instead of the simplified single capacitor, there are indeed multiple capacitors in parallel.

In such a complex system, the electrostatic force can be approximated as

$$F(z) = \int_S dS \frac{\varepsilon_0}{2} E^2(x, y, z) \cong \frac{\varepsilon_0 U^2}{2} \int_S dS \frac{1}{a^2(x, y, z)} \qquad \textbf{Equation 3.12}$$

where ε_0 is the dielectric constant in vacuum, and the integration is over the surface area (S) of the sample. The above approximation is based on linear decay of the electric potential along the field lines (approximated as segments of circles). In this case, the electric field on the sample is $E_{approx} = U_0/a(x, y, z)$, where U_0 is the voltage between the

tip and the sample and *a(x, y, z)* is the arc length of the circular segment coming from the tip and ending at point *(x, y)* at the sample surface. Note that this assumption is valid if the distance between the probe and the surface is no larger than the physical dimension of the probe.
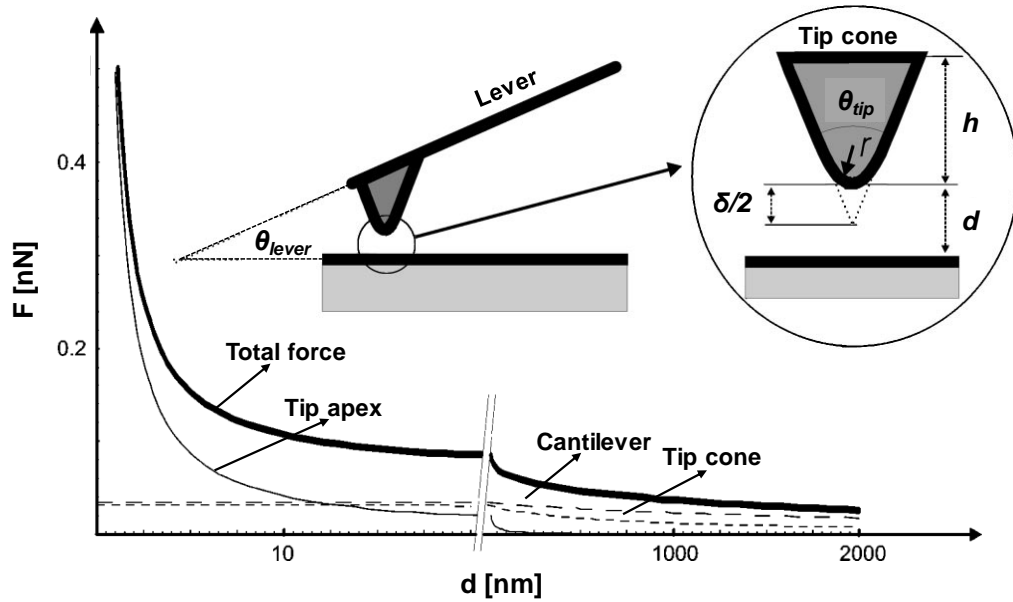
Figure 3.14 Electrostatic force as a function of tip-sample distance. [ref 104]
The parameters corresponding to the effective metallic probe interacting with the surface are $U = 1$ V, and $l = 100$ μm, $w = 1$ μm, $\theta_{lever} = \pi/8$, $h = 2.5$ μm, $\theta_{tip} = \pi/8$, and $r = 20$ nm.

By assuming certain geometry, shape, and *a(x, y, z)*, the individual contribution of the cantilever, tip cone, and tip apex to the electrostatic force can be calculated according to Equation 3.13, Equation 3.14, and Equation 3.15, respectively. The cantilever is characterized with length *l*, width *w*, and angle θ_{lever}; the tip is shaped as a truncated cone with height *h* and opening angle θ_{tip}; and the tip apex is characterized with radius *r*. The electrostatic forces are given as follows:

66

$$F(z)_{lever} \sim \frac{lw}{h^2}$$

$\qquad$ **Equation 3.13**

$$F(z)_{cone} \sim \ln\left(\frac{h}{d}\right)$$

$\qquad$ **Equation 3.14**

$$F(z)_{apex} \sim \frac{1}{d}$$

$\qquad$ **Equation 3.15**

In the case of a typical conductive probe and a flat conductive sample, the total electrostatic force and the individual component from the cantilever, tip cone, and tip apex can be calculated and plotted in Figure 3.14. Clearly, the contribution from the tip apex dominates only for small distances. For larger distances, the total interaction is dominated by the contribution from the cantilever and the tip cone. Much worse lateral resolution will result because the measured electrical property is now a weighted average over the macroscopic area of the cantilever and the mesoscopic area of the cone. It has also been shown by numerical simulations that the cantilever dominates the local electrostatic interaction when the apex size is too small and the accuracy of the measured potential can be improved by using a long and slender but slightly blunt tip supported by a cantilever of minimal width and surface area.

The total electrostatic force shown above also explains that EFM, which detects the electrostatic force gradient, typically exhibits better resolution.[104] Figure 3.15 shows the electrostatic force gradient as a function of the tip-sample distance with the same parameters. As can be seen, the relative contribution of the tip apex to the total electrostatic force is increased dramatically, whereas the interaction induced by the cantilever and the tip cone is strongly reduced. This is due to the different distance

dependence of $F_{apex}(d)$, $F_{lever}(d)$, and $F_{cone}(d)$ on the range that is experimentally important. $F_{apex}(d)$ is strongly dependent on distance but $F_{lever}(d)$, and $F_{cone}(d)$ are not.
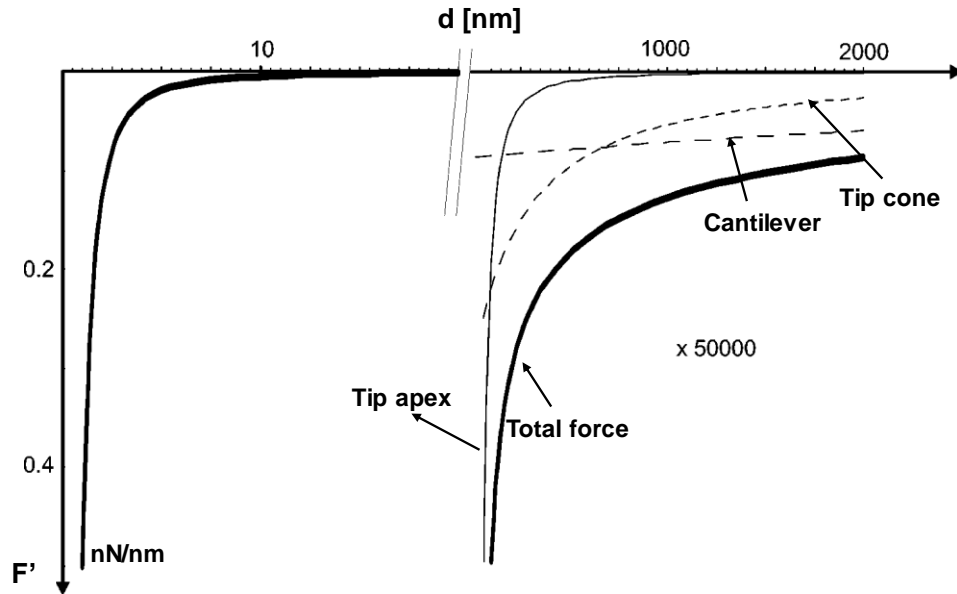
Figure 3.15 Electrostatic force gradient as a function of tip-sample distance. [ref 104]

In addition to the probe geometry and the position of the probe to the sample, there are other factors that could affect the sensitivity and resolution of SKPM and EFM. Examples include:

1. Tip coating. Metal coated tips, although are most commonly used, exhibits poor stability can produce measurement errors. This is because the metal coating, which acts as a reference, is unstable and can be damaged during the measurement. Apparently, a constantly changing reference can greatly affect the accuracy of the measurement. One approach to overcome this issue is to use un-coated tips such as highly doped semiconducting tips. A comparison of metal coated tips and semiconducting tips by Jacobs et al.[105] is shown in Figure 3.16. The CPD acquired by

the metal tip shows significantly larger sudden offset jumps along the vertical slow scan axis. This is due to abrasion of the metal coating, which substantially changes the tip.
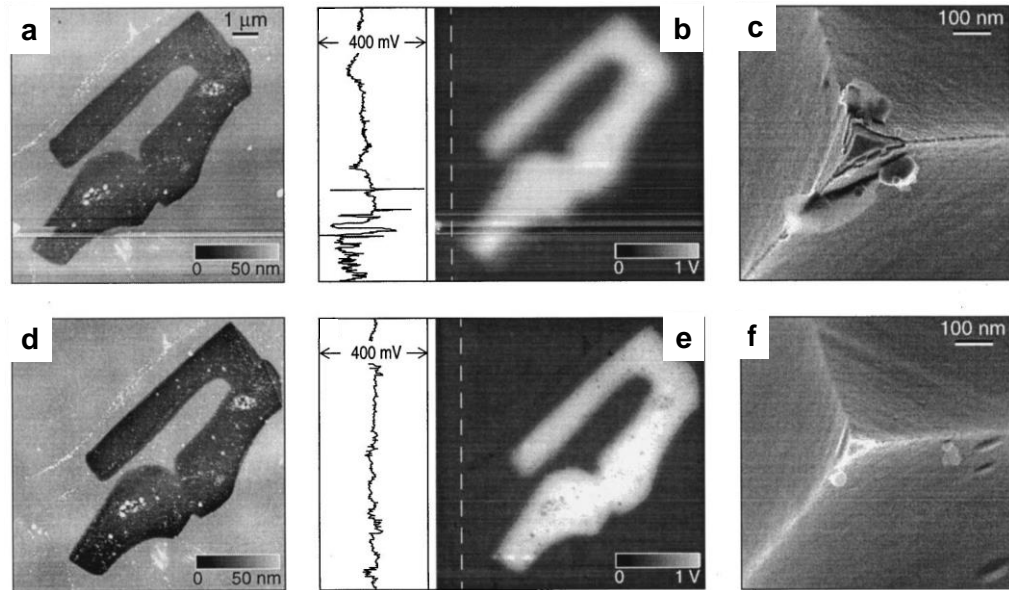
Figure 3.16 Comparison of metal-coated tips vs semiconducting uncoated ones. [ref 105] (a) Topography and (b) CPD of metal film imaged with metal-coated tip. (c) Metal tip after imaging the metal film. (d) Topography and (e) CPD of metal film imaged with uncoated semiconducting tip. (f) Semiconductor tip after imaging the metal film.

2. Environmental Factors. Water and oxygen are the two main environmental factors that affect SKPM and EFM measurement because the work function is highly sensitive to water adsorption and oxide layers. For instance, Sugimura et al.[106] demonstrated that adsorption of water layer on the silicon wafer shields the surface potential contrast (~50 mV) between the p and n type regions of the wafer, as illustrated in Figure 3.17. There is no detectable surface potential contrast between the p and n regions on samples covered with hydrophilic oxide when the imaging is carried out in air with relative humidity of 54%. The contrast increases to larger than

50 mV when the samples become more hydrophobic after thermal annealing. However, when SKPM imaging is performed in a dry nitrogen atmosphere with relative humidity less than 0.6%, about 50 mV surface potential contrast between the p and n regions can be distinguished even on samples covered with the hydrophilic oxides. Therefore, in order to obtain highly resolved and most accurate data, the measurements need to be performed in controlled environments, e.g., glove boxes and ultrahigh vacuum.
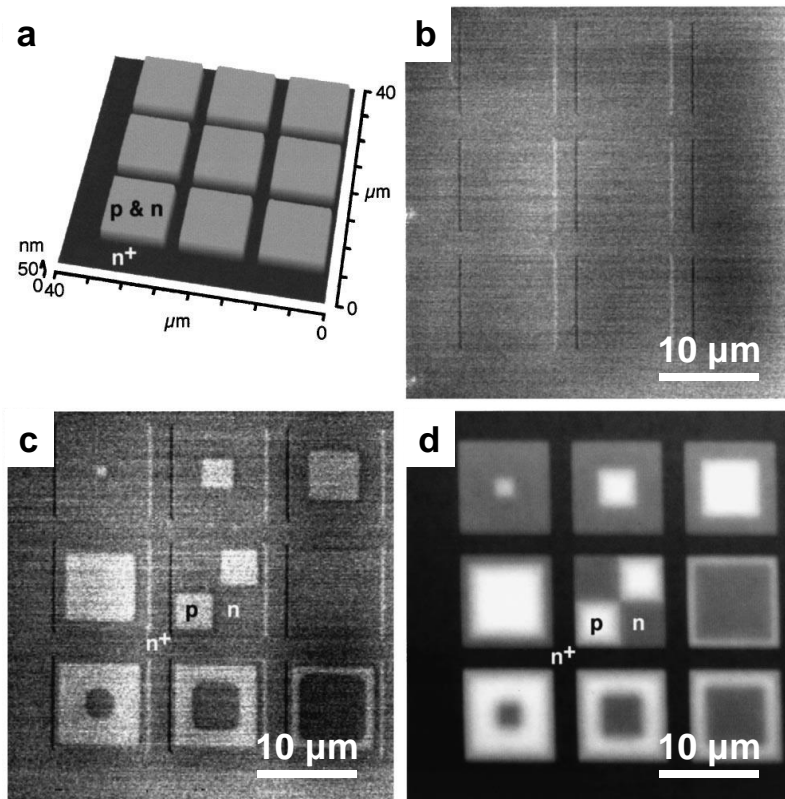
Figure 3.17 Topography and SKPM image of p-n structure. [ref 106]
(a) Topography and (b) SKPM image of a hydrophilic surface obtained in air with 54% relative humidity. (c) SKPM image obtained when the sample is heated at 100 °C for three hours. (d) SKPM image of a hydrophilic surface obtained in air with less than 0.6% relative humidity.

Chapter 4 Electronic Polarization at Pentacene/Polymer Dielectric Interfaces

4.1 Overview

Interfaces between organic semiconductors and dielectrics may exhibit interfacial electronic polarization, which is equivalently quantified as a contact potential difference (CPD), an interface dipole, or a vacuum level shift. In this work, we report quantitative measurements by Scanning Kelvin Probe Microscopy (SKPM) of surface potentials and CPDs across ultrathin (1-2 monolayer) crystalline islands of the benchmark semiconductor pentacene thermally deposited on a variety of polymer dielectrics (e.g., poly(methyl methacrylate), polystyrene). The CPDs between the pentacene islands and the polymer substrates are in the range of -10 to +50 mV. They depend strongly on the polymer type and deposition temperature, and the CPD magnitude is correlated with the dipole moment of the characteristic monomers. Surface potential variations within 2 monolayer (3 nm) thick pentacene islands are ~15 mV and may be ascribed to microstructure (epitaxial) differences. Overall, the microscopy results reveal both strong variations in interfacial polarization and lateral electrostatic heterogeneity; these factors ultimately should affect the performance of these interfaces in devices. This work has been published as *Y. Wu, G. Haugstad and C. D. Frisbie, The Journal of Physical Chemistry C, 118, 2487-2497 (2014).*

4.2 Introduction

It is well known from photoelectron spectroscopy that interfaces between organic semiconductors and metals (O/M interfaces) or between two organic semiconductors (O/O interfaces) can exhibit significant polarization, i.e., a vacuum level shift, or contact potential difference (CPD) may be present at the interface.[29, 107-114] Interfacial polarization, which may be due to interface dipoles or charge transfer,[109, 111, 115, 116] is important because the resulting electric fields exert a strong influence on electronic structure and energy level alignment (i.e., the semiconductor density of states, DOS). For example, interface dipoles can cause a shift of the highest occupied molecular orbital manifold (HOMO band) compared to the organic semiconductor bulk, and such shifts or 'band-bending' are critical to the electrical performance of O/M and O/O interfaces in devices such as solar cells,[117-119] light-emitting diodes,[120, 121] and transistors.[122]

Interfaces between organic semiconductors and insulators (O/I interfaces), on the other hand, are also important for devices, particularly organic field effect transistors (OFETs),[123-128] but they are more challenging to investigate by photoelectron spectroscopy because of electrostatic charging. Consequently, less is known about O/I CPDs, though this knowledge is important for obtaining a better microscopic picture of charge transport in OFETs.

Scanning Kelvin probe microscopy (SKPM) offers an attractive alternative to photoelectron spectroscopy for recording vacuum level shifts and CPDs at O/I interfaces.[96, 129-134] In SKPM, surface potentials (work functions) are recorded and mapped; differences in surface potentials between two materials in contact with each

other (e.g., a patchy film on a substrate) gives the CPD. Significantly, SKPM is not as susceptible to electrostatic charging as it does not rely on electron photoemission but rather on capacitive coupling between a sharp probe and the sample.[135, 136] This makes SKPM readily applicable to O/I interfaces. In addition, high resolution surface potential maps by SKPM can be correlated directly with simultaneously recorded topographic images, which allows assessment of how subtle microstructural features impact the interfacial electrostatics. Surprisingly, relatively little work has been reported in the literature concerning application of SKPM (or a related technique, electrostatic force microscopy) to organic interfaces, especially O/I interfaces.

In this work, we have carried out surface potential mapping by SKPM on ultrathin islands of the benchmark organic semiconductor pentacene grown on polymer dielectrics in order to quantify electronic polarization at different pentacene/dielectric interfaces (see Figure 4.1). The influence of polymer type and deposition conditions, i.e., the substrate temperature, on CPDs has been examined. There is good correlation between the CPD magnitudes and the dipole moments of the characteristic monomers of the polymer substrates. Furthermore, the surprising *intra*-layer surface potential variations of the crystalline pentacene islands are correlated with microstructure. Specifically, we propose that *intra*-island surface potential domains reflect differences in epitaxial order. Overall, the visualization of electronic polarization through spatially-resolved measurements of surface potentials and CPDs provides an effective approach to understanding fundamental electronic processes and electrostatic complexity at organic interfaces.

73
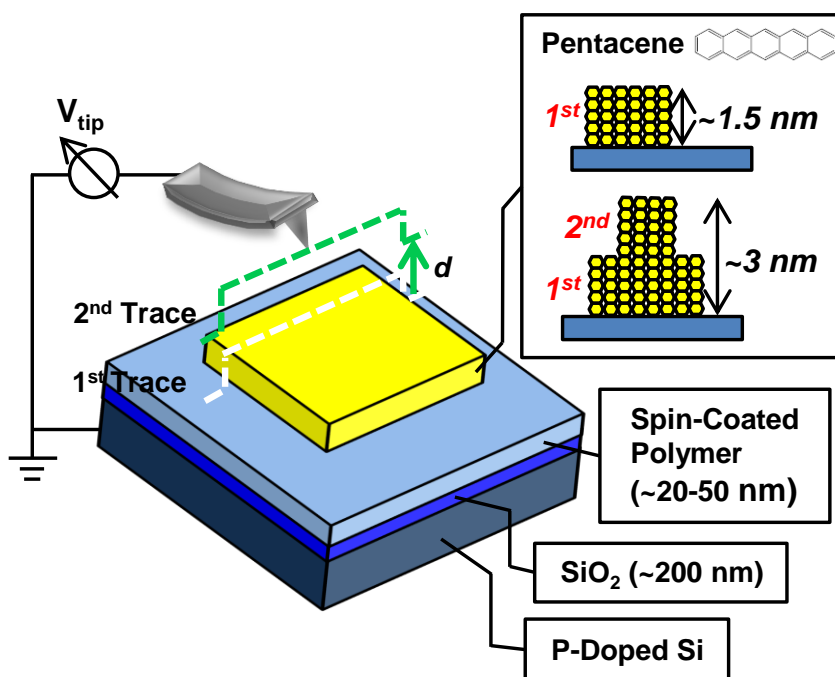
Figure 4.1 Schematic of surface potential mapping by SKPM of ultrathin (1-2 monolayers) pentacene films deposited on a variety of polymeric substrates.
Pentacene was thermally deposited on polystyrene (PS), poly(methyl methacrylate) (PMMA), poly(α-methyl styrene) (PαMS), poly(4-vinyl phenol) (PVPh), along with *para*-substituted PS derivatives, including poly(4-methylstyrene) (PMS), poly(4-tert-butylstyrene) (PtBS), poly(4-bromostyrene) (PBS), and poly(4-chlorostyrene) (PCS). The polymer films were fabricated by spin-coating corresponding polymer solutions onto SiO_2/p++ silicon wafers. A conductive probe scans across the sample surface in a two-pass "lift mode" with a constant lift height of 10 nm, and simultaneously records the topography and surface potential of the sample.

4.3 Effect of Substrate Type on CPD

Crystalline pentacene islands were grown by thermal deposition in a vacuum chamber at 10^{-6} Torr onto a variety of polymer films. Four common polymer dielectrics for OFETs, including PS, PMMA, PαMS, and PVPh, were selected as substrate materials. Notably, the convenience of spin coating relatively smooth surfaces with root-

mean-square (RMS) roughnesses below 0.5 nm over the lateral scale of interest (~20 μm) facilitated the formation of dispersed micron-sized, monolayer thick pentacene islands.

Figure 4.2 Topography, surface potential, and potential histogram of pentacene sub-monolayer islands grown on four common polymer dielectrics.
(a) Topography, surface potential, and potential histogram of pentacene sub-monolayer

on PS. The bright islands in topography represent pentacene grains. They exhibit very similar surface potential compared to PS as shown in the surface potential image. The potential histogram shows the potential distribution peaks of PS and pentacene which are <5 mV apart. (b) Topography, surface potential, and potential histogram of pentacene sub-monolayer on PMMA. The topography shows bright pentacene grains on dark substrate. Pentacene grains have more negative surface potential than PMMA. The CPD (~-20 mV) is defined as the peak surface potential difference between that of pentacene and polymer and is the same for elsewhere. (c) Topography, surface potential, and potential histogram of pentacene sub-monolayer on PαMS. Bright pentacene islands and dark PαMS substrate are shown in topography. The pentacene islands display more positive surface potential than the substrate. Histogram analysis gives a CPD of ~+20 mV. (d) Topography, surface potential, and potential histogram of pentacene sub-monolayer on PVPh with pentacene islands being brighter in both topography and surface potential. According to the potential histogram, the CPD is ~+15 mV.

Figure 4.2 displays representative topography and corresponding surface potential images of monolayer pentacene islands grown on PS, PMMA, PαMS, and PVPh films. All substrates were kept at room temperature during film deposition. Very similar grain morphology was observed for all samples, characterized as dendritic to compact islands with measured heights corresponding to one standing pentacene molecule (~1.5 nm). It is well known that pentacene molecules grown on inert substrate adopt a herringbone, edge-to-face packing motif and the molecules stand nearly vertically in each layer with the [001] direction being approximately perpendicular to the substrate.[52, 137] Thus, there are no face-on molecules in all investigated pentacene sub-monolayers and the darker (lower) regions in the topographic images correspond to bare polymer.

The surface potential images in Figure 4.2 show substantial differences for islands grown on different substrates. Note that all the surface potential measurements presented in this work were carried out using the same probe, which is necessary for meaningful comparisons. Moreover, surface potential of bare polymer films was measured prior to

pentacene deposition and no significant changes of tip-polymer CPDs were observed upon pentacene deposition. In the case of the PS substrate (Figure 4.2a), the surface potential of the pentacene islands is very close to that of PS. Thus, in this case, within the resolution of SKPM,[103, 138, 139] the pentacene grains are almost indistinguishable in the surface potential image. However, significant pentacene-to-substrate surface potential contrast exists in the three other samples. Pentacene displays more negative surface potential than PMMA (Figure 4.2b). Pentacene grains grown on PαMS (Figure 4.2c) and PVPh (Figure 4.2d), on the other hand, show more positive surface potential with respect to the substrates. Both the magnitude and sign of the surface potential contrast change with the polymer substrate type.

Quantitative analyses of the surface potential images are shown in the histograms in Figure 4.2. Instead of conventional histogram analysis which simply counts all data points in an image and typically generates a broad distribution, here independent histogram analyses were performed individually for pentacene islands and the substrates. This procedure diminishes the "edge effects", i.e., the capacitive convolution caused by the finite probe size.[103] That is, those data points located near island boundaries (as determined from the height images) were intentionally neglected during image analyses. Following this approach, two well-defined peak positions are evident in the potential histograms in Figure 4.2. We take the CPD to be the difference in surface potentials between the pentacene islands and the substrate, i.e., the CPD $= V_{pentacene} - V_{polymer}$, where $V_{pentacene}$ and $V_{polymer}$ are the peak surface potentials (approximately the mean surface potentials) in each domain. The CPDs range from ~+5 mV for pentacene/PS interfaces to

~±20 mV for the others. Again, it is interesting that both the sign and the magnitude of the CPDs depend on the polymer type.

To investigate the role of the polymer substrate more systematically, the same SKPM measurements were performed using a family of *para*-substituted PS polymers (PSX) as the substrates: PS, PMS, P*t*BS, PBS, and PCS. The monomers of these polymers have systematically varying permanent dipole moments (μ) that depend on the *para*-substituent, as calculated using the software *ChemDraw*: μ_{CS} (2.38 D) $> \mu_{BS}$ (1.82 D) $> \mu_S$ (0.08 D) $> \mu_{tBS}$ (-0.37 D) $> \mu_{MS}$ (-0.49 D). The topography and surface potential of sub-monolayer pentacene films grown on PS and the four types of *para*-substituted PS at room temperature are compared in Figure 4.3. Again, similar morphology was observed in all cases, but with the island shape slightly varying from more compact to more dendritic from Figure 4.3a to 4.3e. The surface potential and CPDs varied significantly across the sample set. Unlike pentacene/PS interfaces, all four other pentacene/PSX interfaces exhibited significant CPDs. Pentacene displayed slightly more negative surface potential (~-10 mV) than PMS (Figure 4.3a) and P*t*BS (Figure 4.3b), whereas pentacene grown on PBS (Figure 4.3d) and PCS (Figure 4.3e) showed distinctively more positive surface potential than the substrates (~+30-50 mV). The potential histograms clearly reveal the surface potential distributions of pentacene and the substrate. The peak separation reveals the different CPD values.

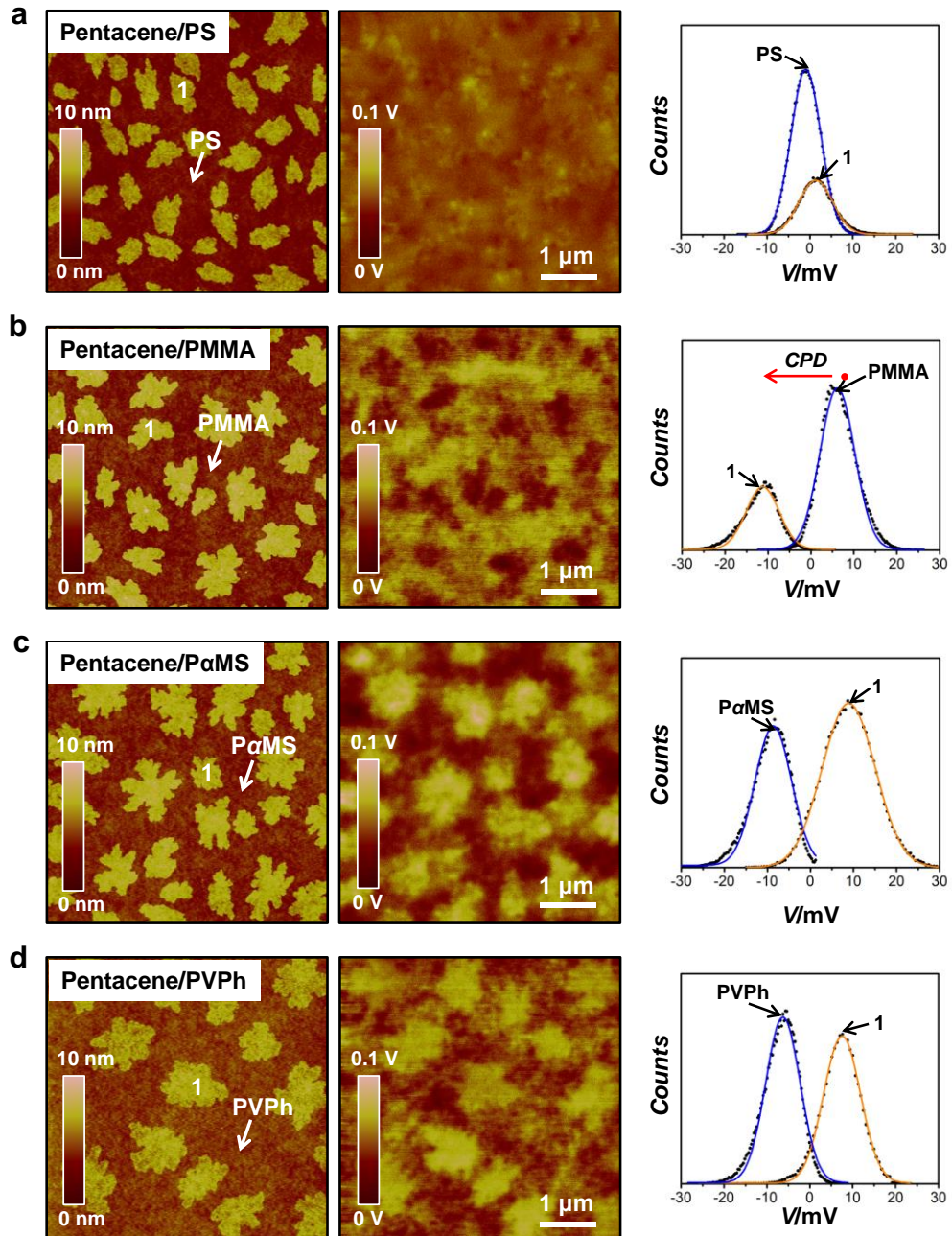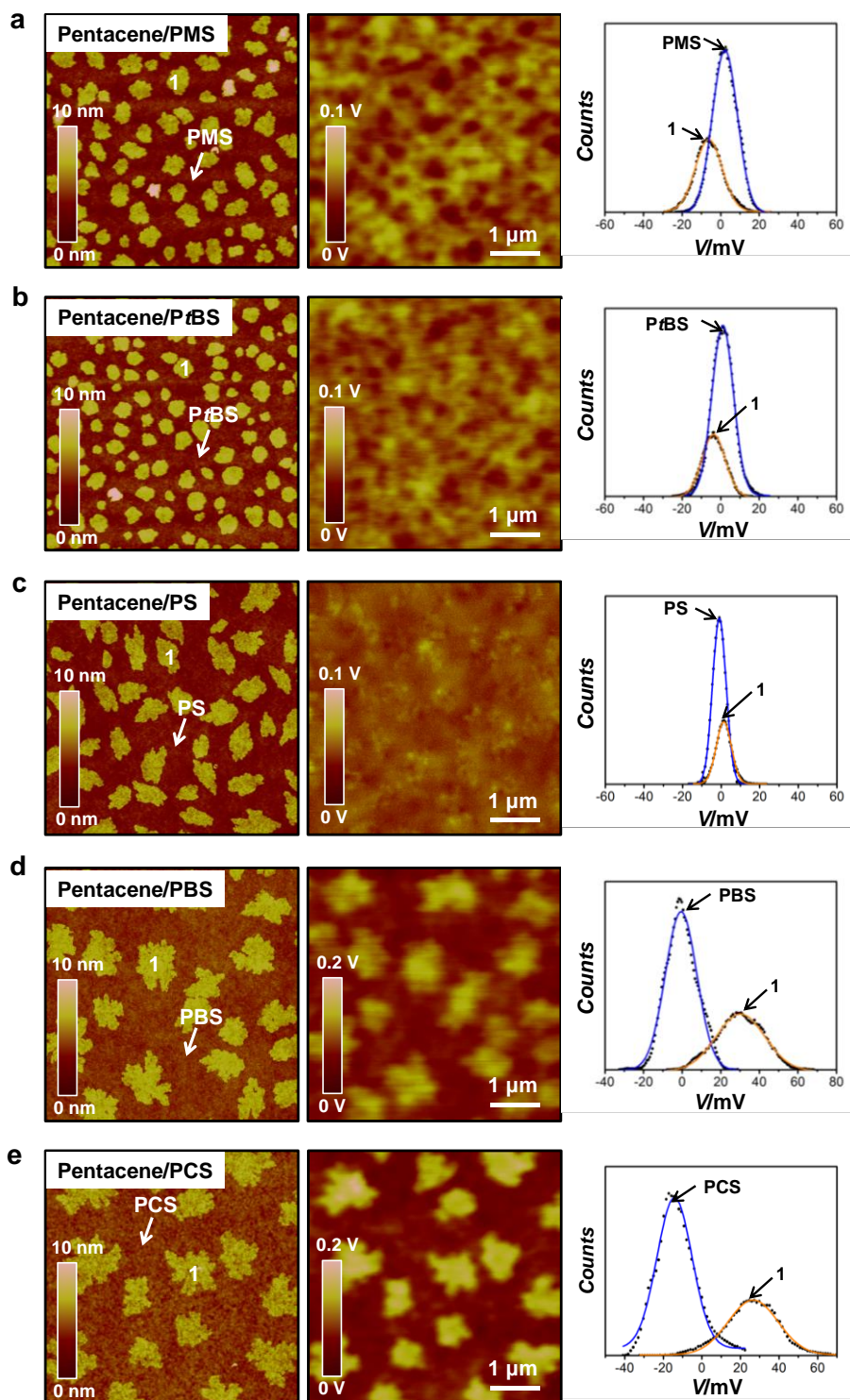**Figure 4.3 Topography, surface potential, and potential histogram of pentacene sub-monolayer islands grown on PS and *para*-substituted derivatives of PS.**
(a) Topography, surface potential, and potential histogram of sub-monolayer pentacene on PMS.

Pentacene islands exhibit more negative surface potential than PMS and the CPD is ~-10 mV. (b) Topography, surface potential, and potential histogram of sub-monolayer pentacene on P*t*BS. Pentacene grains have slightly more negative surface potential than P*t*BS, giving rise to CPD of ~-5 mV. (c) Topography, surface potential, and potential histogram of pentacene sub-monolayer on PS. The pentacene islands display very similar surface potential with respect to the substrate and the CPD is <+5 mV. (d) Topography, surface potential, and potential histogram of pentacene sub-monolayer on PBS with pentacene islands showing more positive surface potential than PBS. The potential histogram shows CPD of ~+30 mV. (e) Topography, surface potential, and potential histogram of pentacene sub-monolayer PCS and pentacene grains are more positive in surface potential than PCS. The CPD is ~+40 mV according to the potential histogram.

The CPD data is summarized in Figure 4.4. The CPDs between pentacene and the corresponding substrate are plotted using the histogram peak positions from six measurements of at least two different samples. The CPD data have been ordered according to the dipole moments of the substrate monomers which are shown on the *x*-axis of the plot. It is striking that the CPD between pentacene and the substrate can be as large as +50 mV in the case of pentacene/PCS interfaces. Also, it is clear that the CPD varies systematically, essentially linearly, with the dipole moment of the characteristic monomers. That is, the surface potential of pentacene islands relative to the substrate (or the CPD) is negative on alkyl-substituted PS, positive on halogen-substituted PS, and close to neutral on PS. The case of P*α*MS is interesting as the monomer has a significant dipole (~0.3 D) approximately perpendicular to the phenyl ring, yet the CPD still falls reasonably close to the trend line. Furthermore, pentacene/PMS and P*t*BS interfaces exhibit smaller CPD magnitudes than pentacene/PBS and PCS interfaces, consistent with the fact that the dipole moments (relative magnitudes) of MS (~0.49 D) and *t*BS (~0.37 D) are much smaller than that of BS (~1.82 D) and CS (~2.38 D).
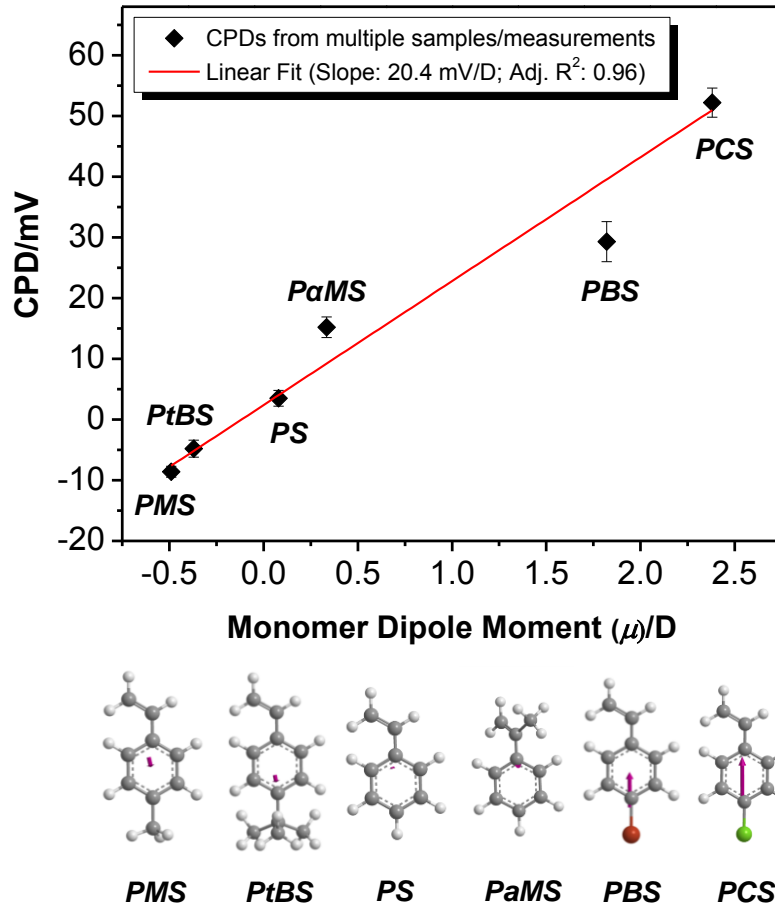
Figure 4.4 Quantitative summary of CPDs as a function of the monomer dipole moment.
All the films were deposited when the substrates were at room temperature. The plotted CPDs
were calculated using the surface potential peaks of pentacene and substrate, respectively, from
potential histograms of at least two different samples in six measurements. The dipole moments
of the monomers were calculated using the software *ChemDraw*. The CPD varies essentially
linearly with the dipole moment of characteristic monomers.

The probable origin of the polarization in the pentacene/polymer systems is induced

polarization of pentacene molecules, not charge transfer. This could be attributed to static

dipoles associated with the polymer surface or so-called cooperative dipoles formed by

specific non-covalent interactions between polymer chains and the pentacene molecules.

Pentacene is known to have large inherent polarizability along its long axis due to the 22

anisotropically delocalized π-electrons in its backbone.[140] We imagine that pentacene molecules in contact with PCS, for example, could be polarized by the strong dipole moment of the CS monomer. There may also be non-covalent interactions between pentacene and the substituent Cl.[141] Either effect, or both, could then induce a dipole in pentacene. Overall, it is clear that the interfacial polarization we observe is directly related to the nature of the substrate.

It should be noted that the linear relationship in Figure 4.4 should be viewed as approximate and applicable to the homologous series of PS polymers we have investigated. The dipole moments have been calculated for the monomers using *ChemDraw* and we have verified their approximate correctness where possible by comparison to the literature values.[142, 143] Furthermore, as shown in Appendix Figure A1.7, CPD data for PMMA and PVPh do not fall on the trend line. The behavior of these more hydrophilic substrates (see water contact angle data in Appendix Table A1-1) appears to be different than the behavior of the PS series polymers. Nevertheless, the overall trend in Figure 4.4 suggests a good correlation between the monomer dipole of the PS polymers and the CPD. We have also carefully excluded other possible contributions to the systematic CPD results, such as the dielectric constant and glass transition temperature of the polymers. Further investigations of other effects including polymer polarizability would also be interesting but we view them as less likely contributors to the CPD trend.

Energy level diagrams are also helpful to further interpret the surface potential and CPD results. According to the above results, films with distinctive CPDs between

pentacene and substrate fall into two categories with pentacene islands being either more negative or more positive than the substrate. The energy level diagrams for these two cases are illustrated in Figures 4.5a and 4.5b, respectively.
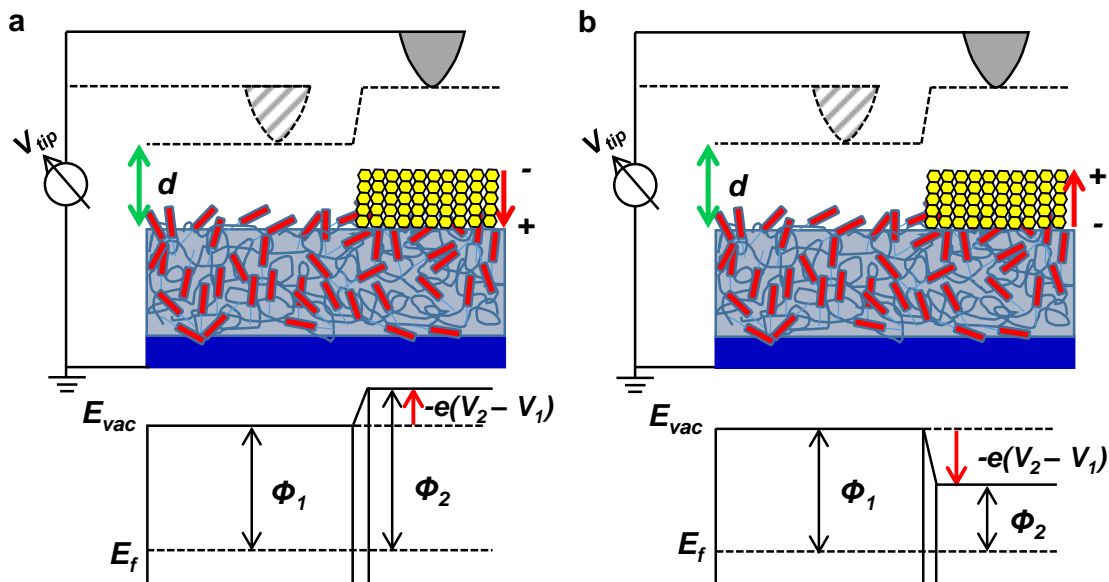
Figure 4.5 Energy level diagram illustration of the surface potential measurement.
(a) Pentacene molecules are polarized in a way that the positive end of the dipole points into the surface, which leads to an upward shift of the vacuum level (E_{vac}). Additional negative bias thus has to be applied when the probe scans from bare polymer to the pentacene islands and it equals the CPD ($CPD = V_2 - V_1$), and darker pentacene grains on brighter substrate are shown in the surface potential map. A net dipole moment pointing into the polymer surface can be deduced. (b) Pentacene molecules are polarized with the positive end of the dipole pointing out of the surface, resulting in a downward vacuum level shift. When the probe scans from bare polymer to pentacene islands, additional positive bias equal to CPD ($CPD = V_2 - V_1$) is applied so that the surface potential map shows brighter pentacene grains on darker substrate. This implies that the polymer surface has net dipoles pointing out of the surface.

A more negative surface potential atop the pentacene islands compared to the bare polymer (e.g., PMS and PtBS) suggests an energy band diagram as shown in Figure 4.5a. The regions covered by pentacene islands have a smaller CPD relative to the SKPM tip (more negative surface potential) than the bare polymer so that the alignment of Fermi

level results in an upward shift of the vacuum level (E_{vac}) from bare polymer to pentacene-covered polymer. The induced dipole must have its positive end pointing into the surface, which is possible when there are net static dipoles at the polymer surface (due to the MS and tBS monomers) that are oriented in the same direction. In contrast, for PBS and PCS samples, the pentacene islands are positive, i.e., they have a larger CPD relative to the SKPM tip, and thus the vacuum level shifts downward over pentacene, Figure 4.5b. This then implies that dipoles with their positive ends point out of the surface. As mentioned above, the origin of the interface dipoles could be static dipoles associated with oriented monomers at the polymer surface, or it is possible that a non-covalent bond forms between the halogen atom in the polymer and the hydrogen atom in pentacene.[141] Either mechanism could shift the π-electrons in pentacene such that the positive end of the induced dipole is pointing out of the surface.

4.4 Effect of Growth Temperature on CPD

The impact of deposition conditions on the surface potential has also been examined. Specifically, the substrate temperature during pentacene deposition was systematically varied and the surface potential of as-deposited films was measured by SKPM. Figure 4.6 shows one example of isolated pentacene islands deposited on PBS. Since the desorption of pentacene becomes more favorable or even dominant when the substrate temperature exceeds 70 °C, the substrate temperature study was constrained within the temperature range of room temperature (27 °C) to 60 °C with an increment of about 10 °C.

84
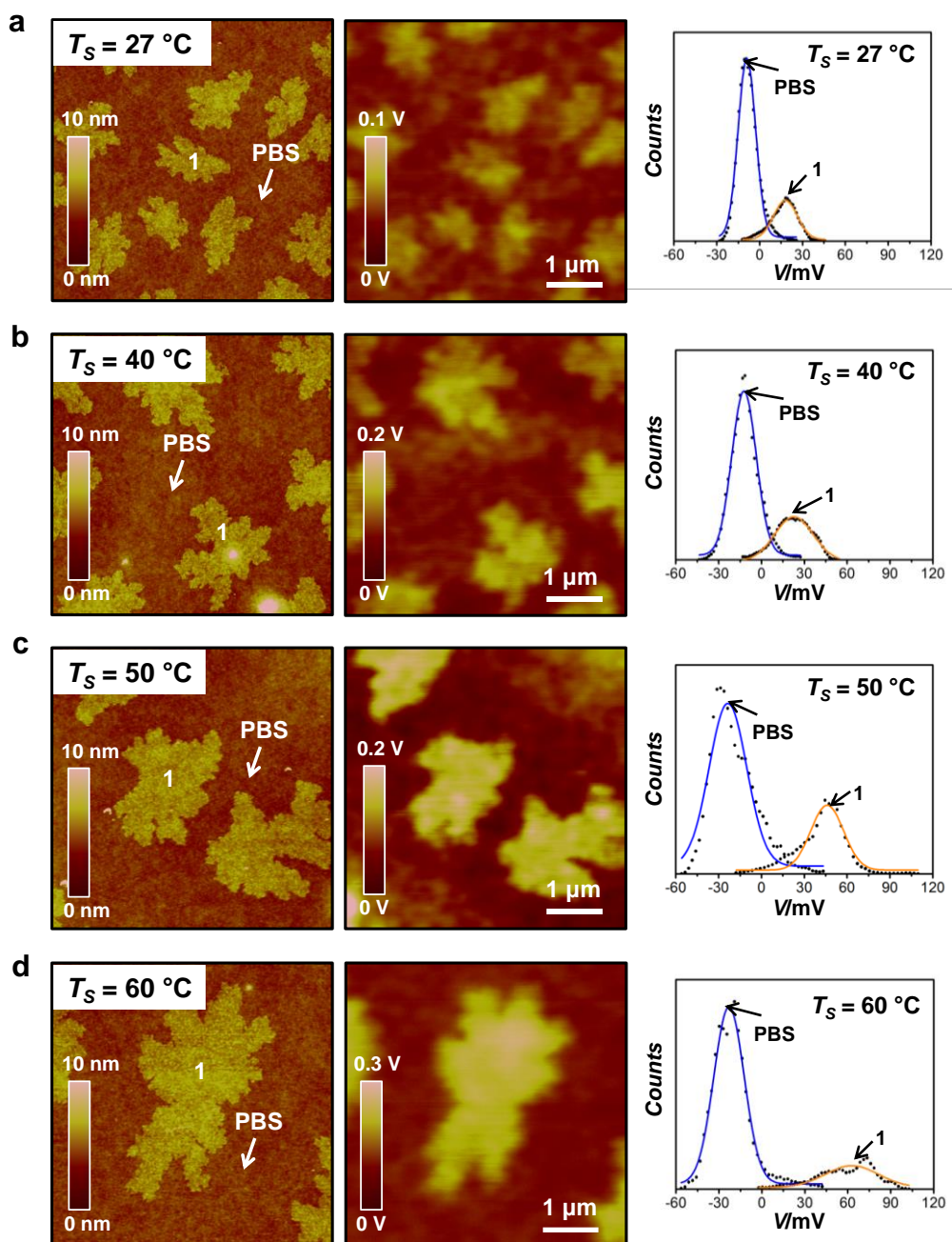
Figure 4.6 Topography, surface potential, and potential histogram of sub-monolayer pentacene grown on PBS at different substrate temperature (T_S).

(a) Topography, surface potential, and potential histogram of pentacene sub-monolayer grown at $T_S = 27$ °C. Pentacene islands displays more positive surface potential than the substrate and the histogram analysis gives CPD of ~+30 mV. (b) Topography, surface potential, and potential histogram of pentacene sub-monolayer deposited at $T_S = 40$ °C. The pentacene grains show more positive surface potential than PBS and the CPD is ~+45 mV as shown in the histogram. (c) Topography, surface potential, and potential histogram of pentacene sub-monolayer deposited at

T_S = 50 °C. The pentacene grains show more positive surface potential than PBS. The histogram gives CPD of ~+75 mV. (d) Topography, surface potential, and potential histogram of pentacene sub-monolayer deposited at T_S = 60 °C. Pentacene displays more negative surface potential than the substrate with the CPD being ~+90 mV.

Clearly, the substrate temperature strongly impacts the grain size and nucleation density as demonstrated in the topographic images. The films tend to have larger grains but smaller nucleation densities with elevated substrate temperature owing to thermally facilitated diffusion of pentacene molecules at higher substrate temperature.[48, 137, 144] Importantly, the substrate temperature significantly impacts the surface potential of the films as illustrated in the images and the potential histograms in Figure 4.6. As the substrate temperature increases, the pentacene surface potential shifts positively.

Figure 4.7 shows the extracted CPDs versus growth temperature. There is an overall positive increase ranging from ~+30 mV at room temperature to ~+90 mV at 60 °C. The causes of this CPD increase with growth temperature may include structural changes in either the pentacene or polymer layers, or thermally-induced strain in pentacene, for example. It is important that the effect is significant, i.e., there is a +60 mV increase in CPD upon changing the deposition temperature from room temperature to 60 °C, but the precise cause of this effect will require further investigation. Similar substrate temperature studies were carried out for pentacene grains deposited on other substrates (see Appendix Figure A1.6). For all cases the CPDs consistently exhibited sensitivity to the growth substrate temperature, though the trends with temperature varied.
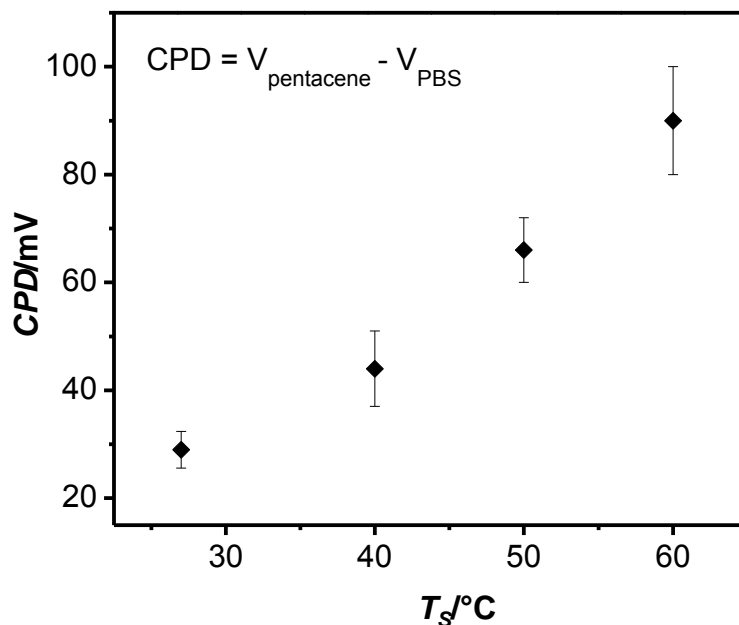
Figure 4.7 Quantitative summary of CPDs for samples deposited on PBS at different substrate temperature (T_S).
The plotted CPD is defined as the surface potential difference between pentacene grains and PBS and each CPD was obtained from the histograms of at least two different samples in six measurements. Significant increase of CPD can be seen with increasing T_S.

4.5 Effect of Interlayer Microstructure on CPD

Pentacene exhibits Stranski-Krastanov (wetting layer plus island) growth behavior[48] on all polymer substrates investigated here. SKPM was employed to record surface potentials in the second layer islands which grow on a completely closed monolayer. Figure 4.8 shows the result for ~3 nm thick pentacene films deposited on the four common polymer substrates (i.e., PS, PMMA, PαMS, and PVPh) at room temperature.
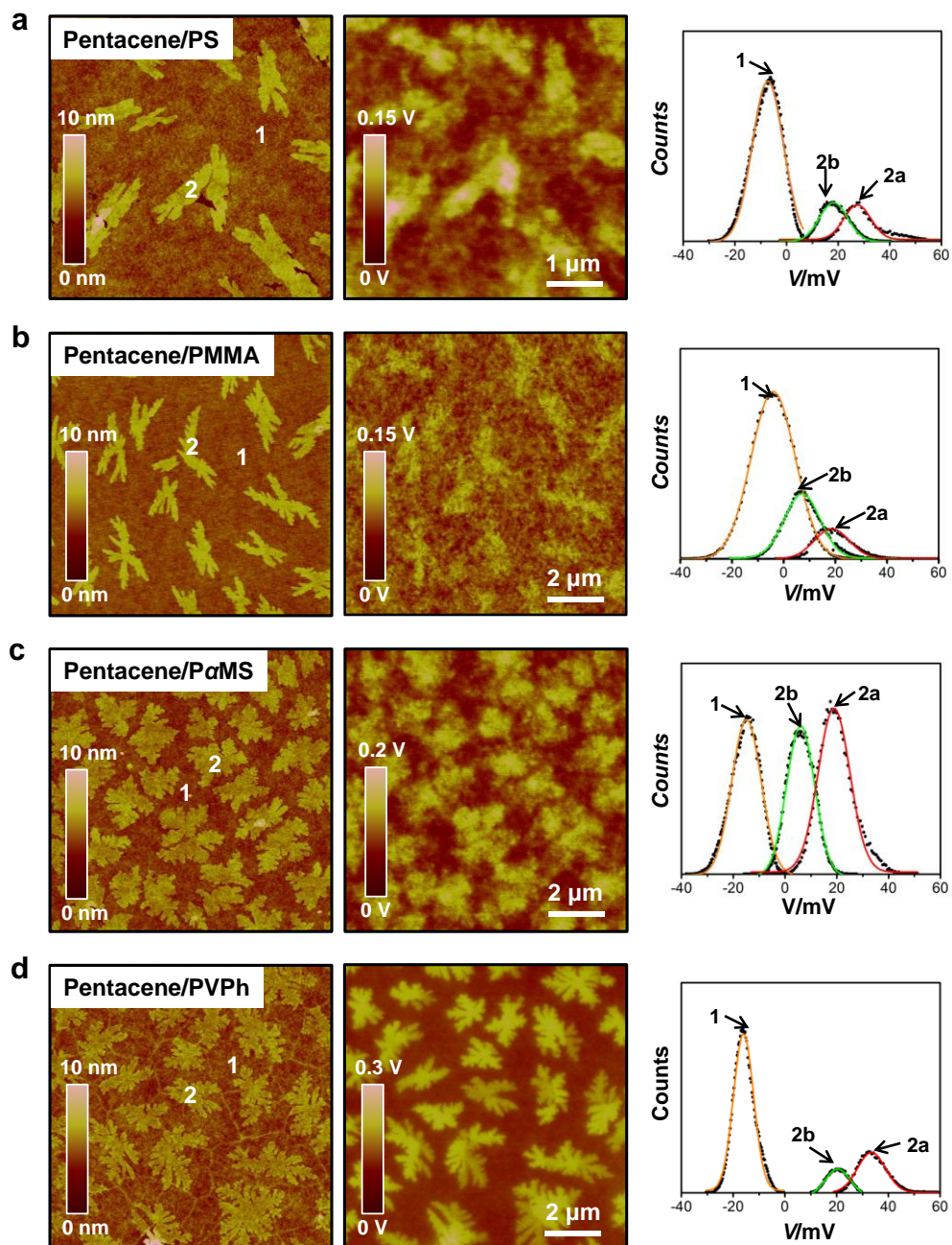
Figure 4.8 Topography, surface potential, and potential histogram of pentacene two-layer films grown on four common polymer dielectrics.

(a) Topography, surface potential, and potential histogram of pentacene film on PS with low coverage of second layer. Pentacene second layer islands exhibit more positive surface potential than the first layer. The potential histogram also gives two distinct domains of the second layer (red and green curves in the histogram). (b) Topography, surface potential, and potential histogram of pentacene two layer film on PMMA with

some second layer grains nucleating on top of fully closed first layer. Pentacene second layer shows more positive surface potential than the first layer but the difference is less than 10 mV. The potential histogram also shows two distinct potential domains of the second layer. (c) Topography, surface potential, and potential histogram of pentacene film on PαMS with complete first layer and some second layer grains. Pentacene second layer grains show more positive surface potential than the first layer. The potential histogram also shows two distinct potential domains of the second layer. (d) Topography, surface potential, and potential histogram of pentacene on PVPh with some second layer grains and fully closed first layer. Pentacene second layer shows more positive surface potential than the first layer and there are two distinct potential domains within the second layer.

All films exhibit similar morphology with dendritic second layer grains growing on top of a fully closed first layer. It is immediately evident from Figure 4.8 that the surface potentials of the second layer islands, although they vary with the substrates in magnitude, are always positive relative to the closed first layer. This is true even for the film grown on the PMMA substrate, which exhibited a negative CPD for the first monolayer (see Figure 4.2). Positive surface potentials are expected in the case of pentacene grown on PαMS and PVPh, because in those cases the first pentacene monolayer had a positive CPD and one could anticipate that polarization in the underlying pentacene first layer should induce a similar polarization in the second layer. The origin of positive surface potential for second layer islands on PMMA, on the other hand, might be structural changes (e.g., crystalline order) in the second layer relative to the first. Surface potentials (work functions) are known to be very sensitive to crystal structure and defect densities.[27, 145, 146] We will return to this point below.

Closer inspection of the images in Figure 4.8 reveals that the *intra*-layer potential landscapes are more complex in the second layer than for the first layer. Specifically,

89

there are two potential domains, 2a and 2b, in the second layer islands. This is particularly evident for the PαMS and PVPh substrates, Figures 4.8c and 4.8d, respectively, where the difference in potential between 2a and 2b domains is extraordinarily clear.
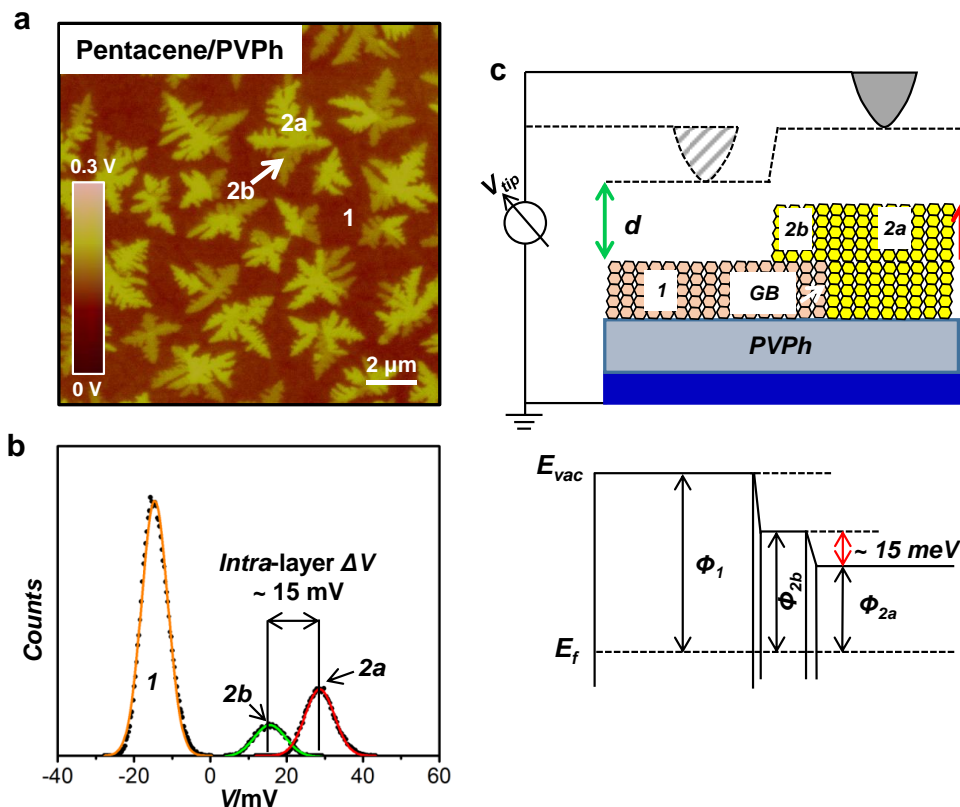
Figure 4.9 *Intra*-layer surface potential difference of pentacene two-layer film on PVPh.
(a) Surface potential of pentacene two-layer film on PVPh with fully coalesced first monolayer and a few dendritic second islands. There are two different surface potential domains within the second layers, indicated as 2a (more positive surface potential) and 2b (less positive surface potential) domains. (b) Histogram shows surface potential variations of pentacene film shown in (a). Surface potential difference (ΔV) between 2a and 2b domains (red and green curves) is ~15 mV. (c) Energy level diagram illustration of the surface potential measurement film in (a). Pentacene second layer molecules are polarized with the positive end of the dipole pointing out of the surface, leading to a downward vacuum level shift. For the 2a domain, which is epitaxial relative to its underlayer, the vacuum level shift is ~15 meV more downward than the 2b domain which overgrows to a different first layer grain.

Figure 4.9a shows the surface potential image of pentacene films grown on PVPh with 2a and 2b domains unambiguously resolved. The potential histogram (Figure 4.9b) clearly illustrates that the *intra*-layer surface potential difference is ~15 mV. The corresponding energy diagram is shown in Figure 4.9c. According to the potential histograms in Figure 4.8, this difference is indeed independent of the substrate type, in contrast to the aforementioned inter-layer surface potential contrast which shows a strong substrate-dependence. More importantly, the *intra*-layer surface potential difference is also independent of the deposition condition, i.e., substrate temperature (see Appendix Figure A1.8), which is again different from the inter-layer surface potential difference.

Such *intra*-layer surface potential variation has also been observed in our previous studies in pentacene films grown on SiO_2.[147, 148] We have proposed that the potential domains 2a and 2b result from differences in homoepitaxy, i.e., that 2a is an epitaxial domain and 2b is non-epitaxial.[148] We have based this on friction force microscopy (FFM) results that consistently show that the 2a domain has lower friction (is more ordered) than the 2b domain.[148] Similar friction/surface potential relationships were observed in pentacene/polymer films examined here as shown in Figure 4.10. It is important to note that our new results here show that the 2a and 2b friction and potential domains occur regardless of the substrate type, i.e. whether the substrate is SiO_2 or a variety of different polymer films. Further investigations have been carried out to determine whether the potential and friction domains are really different epitaxial domains, which will be discussed in Chapter 5.
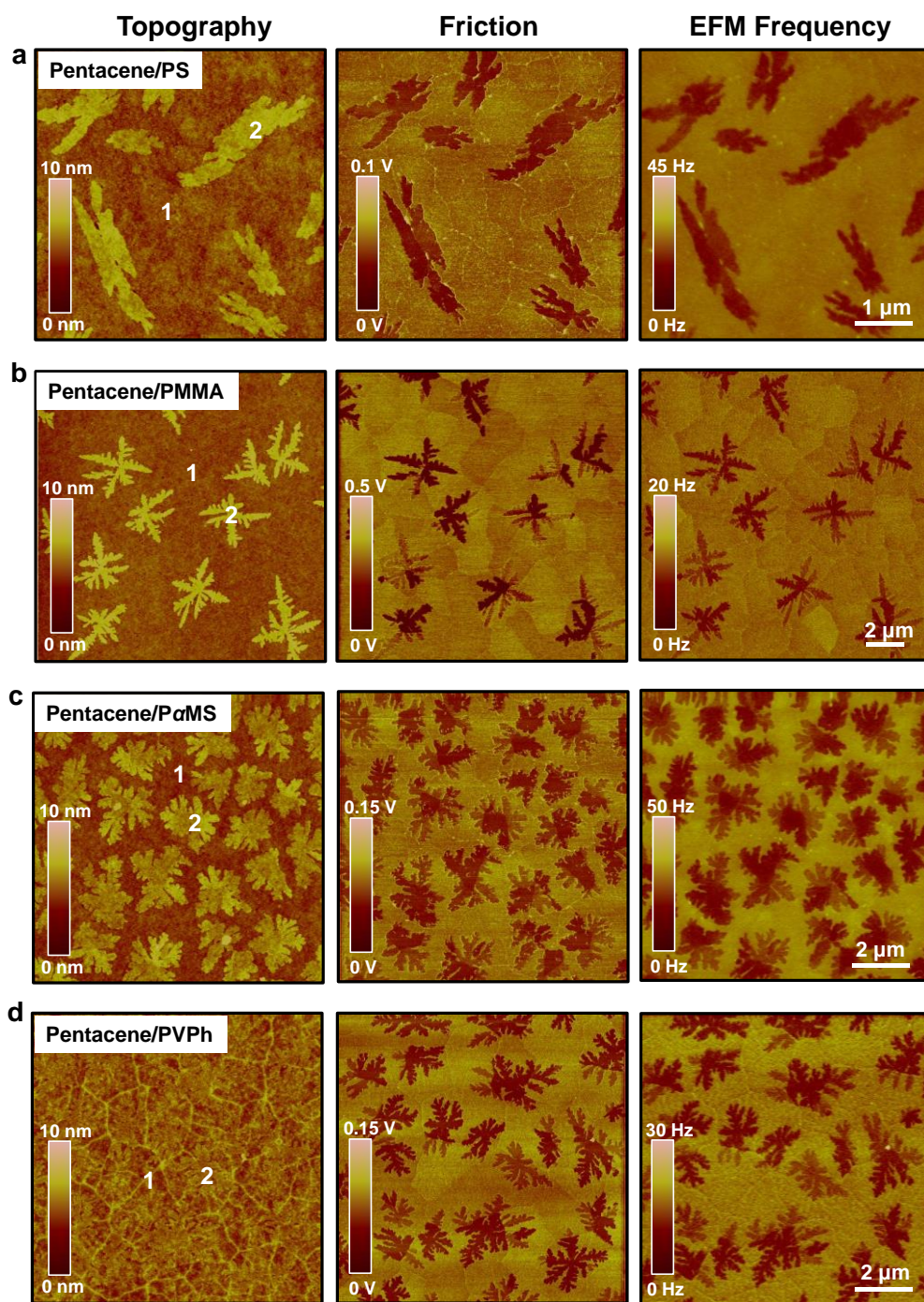
Figure 4.10 Topography and corresponding friction and electrostatic force microscopy (EFM) frequency images of two-layer pentacene films.
(a) Topography, friction and EFM frequency images of two-layer pentacene films on PS. The brighter friction signal corresponds to smaller friction and the brighter frequency contrast represents more negative surface potential. It is the same elsewhere. (b) Topography, friction and

EFM frequency images of two-layer pentacene films deposited on PMMA. (c) Topography, friction and EFM frequency images of two-layer pentacene films on PαMS. (d) Topography, friction and EFM frequency images of two-layer pentacene films on PVPh.

The correlation of crystalline order with surface potential (work function) is intriguing and we propose that it could be understood by the strain effects on work function. For example, a correlation between more positive surface potential (lower work function) and order may mean that second layer islands are uniformly more ordered on all substrates, as these islands always have more positive surface potentials. On the other hand, compared with the first monolayer of pentacene that directly grow on top of amorphous substrates, the second monolayer is significantly less strained. Similarly, the distinct surface potentials observed within the second layer of pentacene films may be attributed to different *inter*-layer strains associated with epitaxy and non-epitaxy. The strain minimized registry of epitaxy is found to exhibit more positive surface potential thank non-epitaxy. The detailed relationship between strain and work function is introduced in Chapter 6. For the purpose of this chapter, it is important to note that the possible use of surface potential mapping to identify domains of more or less order would be extremely useful for understanding microstructure of crystalline soft materials.

4.6 Conclusion

We have carried out quantitative SKPM measurements on ultrathin pentacene films (1-3 nm) thermally deposited on different polymer dielectrics. Systematic investigation of monolayer thick pentacene islands on polymers reveals that the CPDs of the

pentacene/polymer interfaces strongly depend on the substrate type and deposition condition, i.e., substrate temperature. Furthermore, SKPM of two layer thick pentacene films grown on different substrates shows that the surface potential of the second layer pentacene islands is always positive relative to the underlying first monolayer, probably owing to a more ordered structure in the second layer. Intra-layer surface potential differences have been consistently observed in all pentacene films and are believed to arise from microstructure/epitaxial variations. Our investigations reveal important factors that influence the interfacial electronic properties in a benchmark O/I interface and also raise important open questions of how microstructure (e.g., homoepitaxy) affects electronic properties in soft, polarizable organic semiconductor materials. In closing, it is worthwhile noting that surface potential (work function) variations will result in band-edge fluctuations, which in turn imply a disordered landscape for charge carriers at O/I interfaces.

4.7 Experimental

4.7.1   Sample Preparation

All the pentacene films were prepared by thermal evaporation of the source material pentacene (Fluka, 99.8%) onto different dielectric polymer substrates with the chamber pressure $\leq 2 \times 10^{-6}$ Torr and a deposition rate ~0.01 Å/sec. A quartz crystal microbalance (QCM) was used to control the film coverage by targeting ~30-40% coverage for pentacene sub-monolayers and ~120-130% for pentacene two-layer films. The polymer

substrates included polystyrene (PS), poly(methyl methacrylate) (PMMA), poly(α-methyl styrene) (PαMS), poly(4-vinyl phenol) (PVPh), and *para*-substituted PS, namely poly(4-methylstyrene) (PMS), poly(4-tert-butylstyrene) (PtBS), poly(4-bromostyrene) (PBS), and poly(4-chlorostyrene) (PCS). The properties of these polymers are summarized in the Appendix Table A1-1. All the substrates were prepared by spin coating corresponding polymer solutions (PMMA, PαMS: 10wt% polymer/1,2-dichloroethane solution; PS, and PS derivatives: 5wt% polymer/toluene solution; PVPh: 5wt% polymer/ethanol solution) onto thermally grown SiO_2 (~200 nm) on p-doped silicon wafers (2000 rpm, 30 sec) and baked at 90 °C for 1 hour to remove residual solvent. According to atomic force microscopy (AFM) measurements, all the spin coated polymer films have thicknesses around 20-50 nm. The substrate temperatures were varied from room temperature (27 °C) to 60 °C for different depositions.

4.7.2   Scanning Probe Microscopy

All the SPM measurements were performed with a Bruker Nanoscope V Multimode 8 Scanning Probe Microscope inside an argon-filled glove box with oxygen level <5 ppm. SKPM has been utilized to measure the surface potential of as-deposited pentacene films. To allow comparison between different cases, the same tip was used throughout all the measurements. SKPM is a non-contact SPM method capable of probing the local surface potential distributions while simultaneously mapping the topography. Commonly, it operates in a two-pass interleave mode or "lift mode". In the first pass, the specimen is scanned by a sharp conducting probe in regular attractive regime dynamic mode for

topography. To stabilize performance in the attractive regime, the cantilever is driven at a drive frequency slightly larger than the fundamental resonant frequency, and the setpoint amplitude is about 90% of the free amplitude. In the second pass, the probe is lifted for a constant height above the surface and the surface is scanned over again along the same topographic trajectory to preserve constant average distance between probe and sample. In the operational procedure of the second pass, the mechanical vibration of the cantilever is zeroed, whereas an AC voltage is applied to induce the vibration of the cantilever. The vibrational amplitude is nulled with a feedback circuit that adjusts an additional DC voltage bias of the tip (per surface location) to match that of the local surface; this local surface potential is directly recorded as this DC voltage. The attractive regime dynamic mode is preferred for our SKPM measurement (i.e., in the first pass that generates the topography image) since it better preserves the probe and thereby allows meaningful surface potential comparison among different films by eliminating probe-to-probe variation. Note that the same probe (tip/cantilever) was used for all the SKPM measurements shown here but these results were representative of a large body of experiments using different probes. The typical probes were from Mikromasch USA (DPER 18, Pt coated, resonant frequency 60-90 kHz, spring constant 2.0-5.5 N/m, and tip radius 30 nm). The lift height during the second pass was 10 nm, which was beyond the range where van der Waals force comes into play. The applied AC voltage in SKPM was 0-+6 V in amplitude.

4.7.3   Histogram Analysis

All histogram analyses were performed using freeware *Gwyddion*. To obtain well-defined surface potential distributions for different surface regions instead of one broad potential distribution for all the regions, individual regions were selectively masked using surface potential thresholding. (For those surface potential images with worse differentiation, masks were created via thresholding of the simultaneously obtained topography image and then applied to the surface potential images.) Histogram analysis was performed for the masked regions and all extracted histograms for different surface regions were overlaid in graphs to compare the surface potential distributions within a given image. (A detailed example is provided in the Appendix A1.) An alternative method was to extract the histogram from an entire image and perform single- or multi-peak Gaussian curve fits to distinguish the potential distributions from different regions. A comparison of the histograms obtained from the two methods is made in the Appendix A1. Importantly, it is meaningless to compare the absolute position of each peak among different histograms since a plane fit has been applied the images that offsets the absolute peak position in order to bring the average of all peaks in a histogram to the zero-position.

4.7.4   Dipole Moment Calculation

ChemBio3D Ultra 13.0 integrated with ChemBioDraw Ultra 13.0 was used to compute dipole moments of the monomers for different polymers. The molecular structure of each monomer was built by ChemBioDraw and then displayed in 3D by

ChemBio3D. The dipole moment of corresponding structure was then computed by the *ab initio* electronic structure calculation program GAMESS interface which is included in the software.

Chapter 5 Homoepitaxial Growth Modes in Textured, Polycrystalline Ultrathin Pentacene Films on Dielectrics

5.1 Overview

As introduced in Chapter 4, homoepitaxial growth modes likely affect the interlayer electrostatic coupling and the surface energetics of device-active organic films. However, detailed knowledge of the homoepitaxial growth modes in organic semiconductor thin films is still largely missing due to the lack of effective characterization tools. This chapter presents a convenient approach to characterize explicitly the homoepitaxial growth modes of pentacene bilayers thermally deposited on different dielectrics by combining two scanning probe microscopy (SPM) imaging modes, i.e., friction force microscopy (FFM) and transverse shear microscopy (TSM). It is found that pentacene second layer grains consistently exhibit a mosaic of homoepitaxial modes (commensurism, coincidence, and non-epitaxy) regardless of the substrate type and deposition condition. Among different homoepitaxial modes, a coincident twist epitaxy is more frequently observed. This combined FFM/TSM technique offers a feasible way to identify complex microstructural motifs such that a deeper understanding of growth and structure-property relationships in organic semiconductor thin films is possible. This work has been published as *Y. Wu, V. Kalihari, G. Haugstad, and C. D. Frisbie, Physica Status Solidi b, 252, 1291-1299 (2015).*

5.2 Introduction

Polycrystalline organic semiconductor thin films are of significant interest due to their applications as active components in electronic devices, e.g., field effect transistors (FETs).[4, 122, 149-153] Many electrical properties of these active layers, such as carrier mobility and work function, are closely related to order/disorder of the film microstructure.[154-158] The role of grain boundaries (GBs) has already been extensively discussed.[159-163] However, much less investigated is the role of homoepitaxial growth modes. Homoepitaxy in crystalline organic semiconductor films describes the *interlayer* epitaxial relationship between the organic overlayer and underlayer. It is associated intrinsically with the layered and polycrystalline nature of many thermally deposited organic molecular films. Although molecular epitaxy of soft organic materials has been of growing interest over the past two decades, the focus of the field has been primarily on heteroepitaxy of organic molecular layers on organic/inorganic crystalline substrates.[164-171] Homoepitaxy of a molecular overlayer deposited on an existing crystalline underlayer of the same material on common dielectric insulators is still largely unexplored. However, this knowledge is critically important for understanding the interlayer electrostatic coupling and the surface energetics of device-active organic semiconductor thin films, especially within the first few monolayers of the film close to the organic/insulator interface as we have demonstrated previously.[147, 148]

The major hindrance for thorough understanding of homoepitaxy in organic semiconductor thin films lies in the lack of effective characterization tools. Applications of conventional electron diffraction based characterization techniques, such as reflection

high energy electron diffraction (RHEED) and low energy electron diffraction (LEED),[168-170, 172-174] can be problematic for the investigation of organic films on insulators due to charging. Also, the existence of any microscopic variation is hard to discern with diffraction techniques because these usually sample a large area. Scanning probe microscopy (SPM), on the other hand, offers an attractive alternative for identifying local homoepitaxy in organic semiconductor thin films on insulators. Previously, our group identified different homoepitaxial modes in pentacene thin films deposited on SiO_2 by transverse shear microscopy (TSM).[148] TSM is an unconventional lateral force microscopy (LFM) technique that produces crystallographic orientation dependent contrast.[85, 86, 147, 148, 175, 176] Therefore, in theory, the overlayer and underlayer grain orientations can be determined unambiguously according to their particular TSM signals. This then allows identification of the homoepitaxial mode[164] (e.g., commensurism vs. coincidence). In reality, however, this method typically requires repeated imaging with systematic rotations of the sample. The intrinsic noise floor of the instrument, which is usually comparable to the relatively small TSM signal, also significantly increases the minimum number of TSM images needed for reliable analysis. It is thus helpful to develop more convenient methods to examine homoepitaxial modes in soft, textured crystalline organic layers.

In this chapter, we carried out concurrent friction force microscopy (FFM) and TSM imaging to characterize the homoepitaxial modes of individual domains within the second layer of pentacene films thermally deposited on SiO_2 and a polymer dielectric, poly(methyl methacrylate) (PMMA), at different substrate temperatures. The

homoepitaxial landscapes of all investigated films exhibit a mosaic characteristic, i.e., there are mixed homoepitaxial modes, including commensurism, coincidence, and non-epitaxy (i.e., incommensurism and also non-coincidence), within the pentacene second layer at the micrometer length scale. Among different homoepitaxial modes, a coincident twist epitaxy, which by definition is a more relaxed epitaxial condition with only partial registry of the overlayer and underlayer,[164] was more frequently observed.

5.3 Characterization of Grain Orientations by TSM

As mentioned above, previous studies in our group demonstrated that TSM exhibits orientation dependent contrast and thus offers the capability of identifying the homoepitaxial modes in crystalline organic thin films.[148] As shown in Figure 5.1a, in the case of (001)-textured pentacene thin films, the TSM signal depends systematically on the relative alignment (θ) between the scan direction and the crystallographic orientation (e.g., [100] direction) in the (001) plane of any pentacene grain. Specifically, TSM gives the brightest signal (*ii*) when the probe scans parallel to the pentacene [110] direction; it gives the darkest signal (*iv*) when the scan direction is along the $[\bar{1}10]$ direction. Intermediate contrast (*i* and *iii*) is more complex as it does not correspond to one single crystallographic direction. Instead, it can be obtained when the probe is scanning along either the [100] direction or the [010] direction. Dark-to-intermediate and intermediate-to-bright contrasts are similarly complicated as each is associated with two independent crystallographic directions.
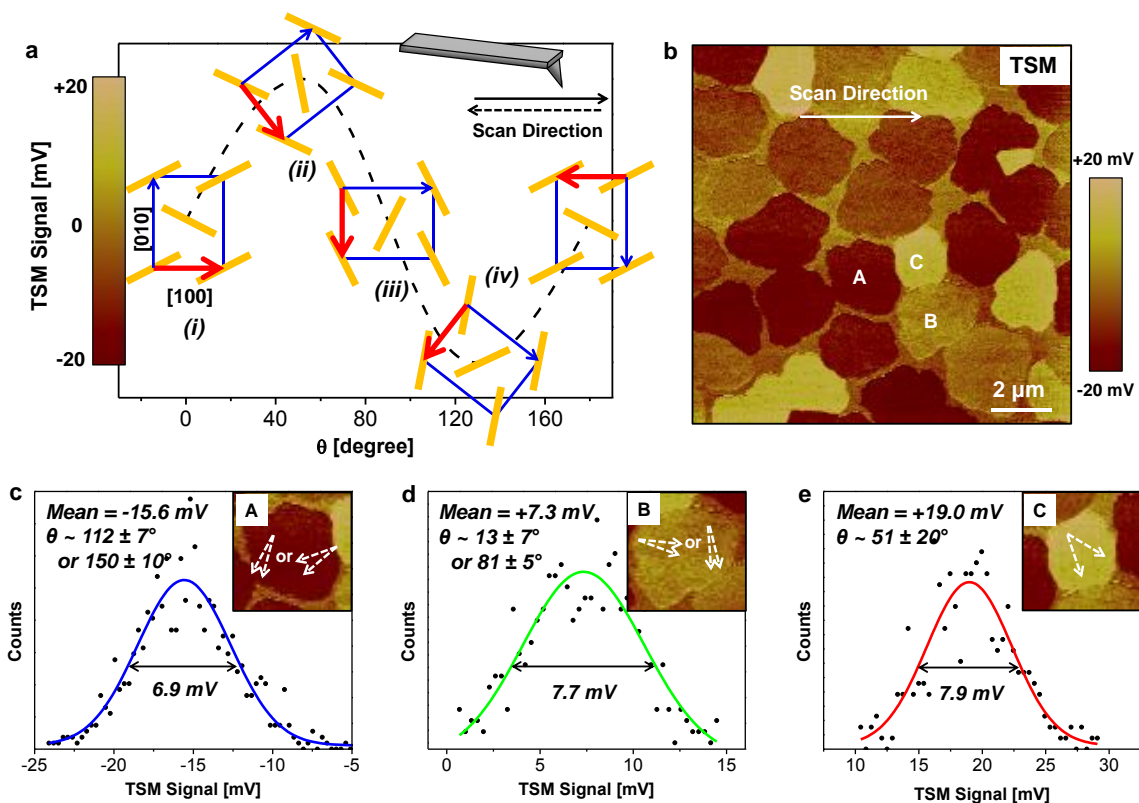
Figure 5.1 Pentacene grain orientation determined by TSM.
(a) Schematic relationship between TSM contrast and pentacene grain orientation. For this figure, the scan direction is fixed and θ is defined by the angle between the forward scan direction and the pentacene [100] direction (red arrow). The grain orientations with the most positive, the most negative, and intermediate TSM signals are depicted with the corresponding pentacene monolayer unit cell structure in the a-b plane. (b) TSM image of sub-monolayer pentacene film thermally deposited on PMMA. Different grains (e.g., grain A, B, and C) show different TSM signal levels. (c) TSM signal histogram of grain A with a FWHM of ~7 mV. The range of possible [100] orientations is indicated by dashed arrows in the inset. (d) TSM signal histogram of grain B. The possible range of [100] orientations determined by the TSM signal are shown in the inset by dashed arrows. (e) TSM signal histogram of grain C. The possible [100] orientations determined by TSM signal are shown by dashed arrows in the inset.

This situation is well exemplified by TSM imaging of pentacene on PMMA. Note that our previous detailed TSM work involved pentacene on SiO_2,[85] which is not an ideal substrate for organic FETs applications compared to polymer dielectrics.[125, 177] As shown in Figure 5.1b, pentacene forms polycrystalline monolayer-thick compact grains on

PMMA, very similar to pentacene deposited on SiO_2.[85, 137, 176] More importantly, the TSM image of pentacene on PMMA also displays the full contrast spectrum among different pentacene grains, indicating that the sensitivity of TSM to the crystallographic orientation of pentacene is qualitatively the same for PMMA and SiO_2 substrates. However, it is non-trivial to assign specific orientations to grains in Figure 5.1b based on the TSM signal with the lack of an unambiguous one-to-one correspondence between the TSM signal and crystallographic orientation. More complicated is the intrinsic noise of the measurement, manifested as the finite peak width in the TSM signal histograms for individual grains in Figure 5.1c-e. The peak width characterized by the full width at half maximum (FWHM) up to 10 mV is comparable to the total TSM signal, which results in a relatively large spread of possible [100] orientations determined by TSM as shown in Figure 5.1c-e and Figure A2.1 in Appendix. Therefore, in order to explicitly index the crystallographic orientation of each pentacene grain, multiple TSM images must be obtained as a function of systematic rotation of the sample. This protocol would require even more imaging in order to decipher the homoepitaxial modes in *two-layer* films since grains of both overlayer and underlayer are involved.

5.4 Characterization of Homoepitaxial Growth Modes by TSM/FFM

In order to straightforwardly determine homoepitaxial modes with minimal imaging, concurrent FFM and TSM were carried out. FFM and TSM can be performed on the

104

same SPM set up, and the only operational difference between the two is the scan angle, i.e., the angle between the fast scan direction and the cantilever long axis. The scan angle is 90° for FFM and 0° for TSM. Although it is impossible to index the exact homoepitaxial modes with a single image by either technique, a combination of the two provides sufficient information for quick assignments of the homoepitaxial modes, as will be shown later.

An example of TSM imaging on pentacene two-layer films thermally deposited on PMMA is shown in Figure 5.2. Both topography and TSM images were simultaneously acquired. According to the topography image, under the low flux growth conditions, pentacene forms dendritic second layer grains on top of a complete first layer, which is known as Stranski-Krastanov growth behavior (wetting layer plus island growth).[48] The TSM images, at first glance, display much richer contrast than the topography images with grain orientations of both layers clearly resolved. A closer look at the TSM images reveals that there are two distinct types of second layer grains based on the interlayer TSM contrast. The type A second layer grain, as denoted in Figure 5.2b, cannot be distinguished easily from the first layer as it shows very similar or identical TSM contrast as the underlying first layer. The type B grain (a large part of it), on the other hand, exhibits sharp TSM contrast with respect to the first layer underneath.
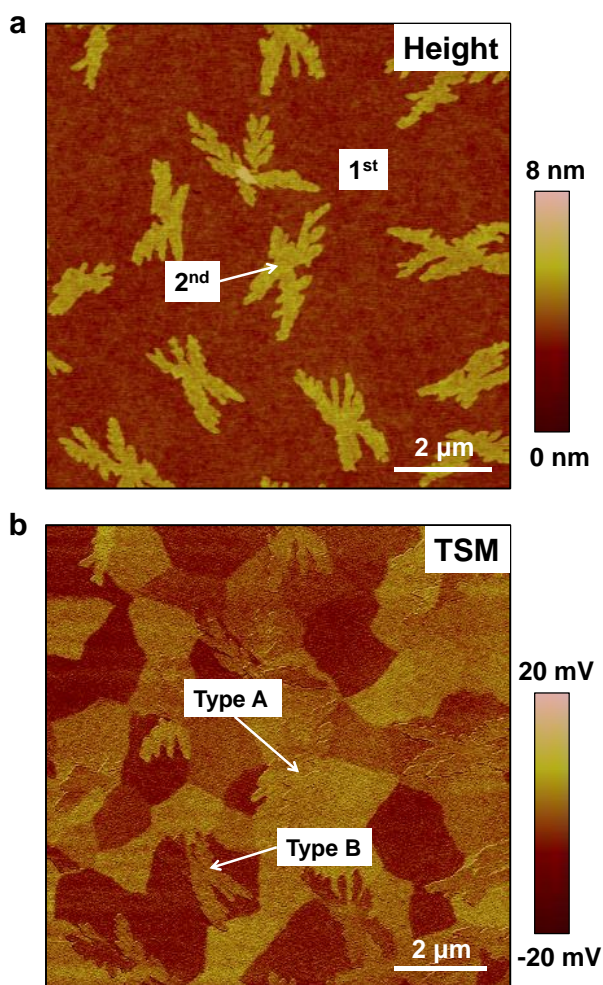
Figure 5.2 Topography and corresponding TSM images of pentacene two-layer films grown on PMMA.
(a) Topography of pentacene on PMMA showing continuous first monolayer and dendritic second layer grains. (b) Simmultaneously acquired TSM image of film in (a) with grains of both layers showing rich contrast. Two types of second layer grains are labeled. Type A grain: second layer grain which has almost the same TSM signal as the underlying first layer; possibly commensurism or non-epitaxy is adopted. Type B grain: second layer grain with distinct TSM signal than the underlying first layer and it is either non-epitaxial or coincident with respect to the first layer.

Unambiguous assignments of the homoepitaxial modes are impossible based on

Figure 5.2b alone since both layers could have a spread of orientations according to the

106

TSM signals and the relationship between the actual orientations is unknown. For example, the type A grain is either commensurate, in which case its actual orientation is exactly the same as that of the underlayer, or it is incommensurate if the actual orientations of the two layers misalign with each other. For example, the underlayer could correspond to (*iii*) in Figure 5.1a and the overlayer could be (*i*); both orientations give the same TSM contrast and yet there would clearly be no commensurate registry between the two layers. The type B grain, although it must exhibit a different orientation than the first layer, is not unambiguously non-epitaxial as coincident epitaxy also exhibits different interlayer grain orientations. Even with these uncertainties, it is conclusive from the TSM image that there are *mixed homoepitaxial modes* in the pentacene second layer for films deposited on both PMMA and SiO_2. Similar observations are also made for pentacene films grown at different deposition conditions, i.e., different substrate temperatures (see Figure A2.2 in Appendix).

An example of high resolution friction imaging of pentacene two-layer films is given in Figure 5.3. The pentacene second layer exhibits striking friction variation even within the same pentacene grain, whereas the first layer displays minimum friction contrast. Unlike the TSM signal which varies continuously from the darkest to the brightest, friction of the pentacene second layer only shows two distinct signals, denoted as low friction (LF) and high friction (HF), respectively. It is important to note that the low friction domain is well confined within the grain boundaries (GBs) of the first layer right beneath the center of the second layer dendrite, where the second layer grain nucleated. Where the arms of the second layer dendrite have grown so as to cross the grain boundary

in the first layer, these portions of the arms display much higher friction. Clearly, the change of the friction signals is strongly associated with the interlayer relationship, or homoepitaxy.
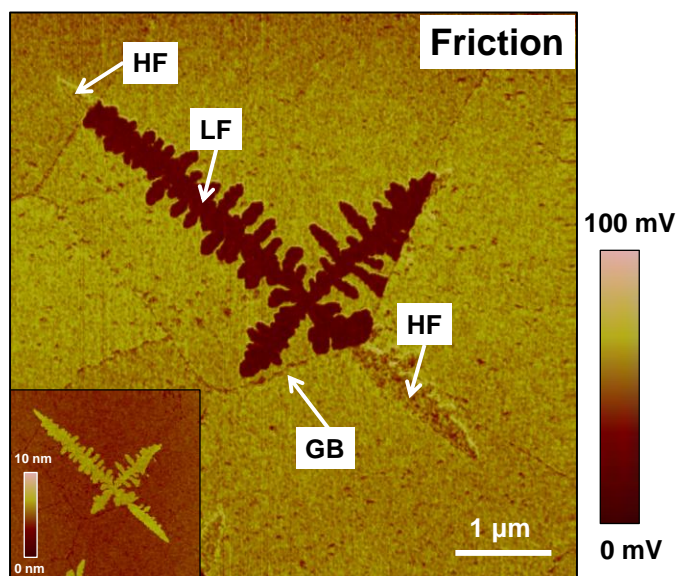
Figure 5.3 High resolution friction image illustrating friction variations within the same pentacene second layer grain.
There are low friction (LF) and high friction (HF) domains coexisting in the same second layer grain. The more ordered LF domain is confined within the grain boundary (GB) of the first layer right beneath the center of the second layer dendrites (i.e., nucleation center), indicating that the second layer grain initially nucleated atop of the first layer epitaxially. The transition from LF (more ordered) to HF (less ordered) occurs when the arms of the dendrites span across the GB of the underlying first layer, implying the loss of epitaxy. Inset: height image obtained simultaneously with friction and no information about the specific epitaxial modes is revealed.

It is known that friction signals obtained from FFM are directly related to the degree of order/disorder in a molecular film,[72, 77, 81, 82, 178, 179] i.e., less ordered molecular arrangements generally lead to higher friction due to the presence of a larger number of dissipative modes. Therefore, it is reasonable to assign the low friction (more ordered) domains as epitaxial and the high friction (less ordered) domains as non-epitaxial. The

transition from low friction to high friction is hence an indication of the loss of epitaxy. This important conclusion is also supported by combined TSM and FFM imaging described below. Such transitions repeatedly occur when a second layer grain overgrows a first layer grain where it nucleated to cover a neighboring first layer grain. This situation is common and reflects the evolution of homoepitaxial relationships during film growth. Note also that similar friction maps have been obtained for pentacene two-layer films thermally deposited on a number of polymeric substrates, such as polystyrene (PS) and poly(α-methyl)styrene (PαMS).[180] This suggests that similar growth modes are commonly adopted by pentacene thin films thermally deposited on a variety of organic or inorganic dielectrics. More importantly, it also strongly validates friction as a general indicator for epitaxy and non-epitaxy in such polycrystalline two-layer organic films.

By combining the information obtained from friction and TSM images, the homoepitaxial modes can be determined conveniently. This is the central thesis of our current work. Figure 5.4a and 5.4b show the friction and TSM images of a pentacene two-layer film grown on PMMA. For instance, a domain of non-epitaxy can be identified easily according to Figure 5.4a and 5.4b, i.e., high friction and large TSM contrast. Similarly, for the grain in the lower part of Figure 5.4a and 5.4b, epitaxy is identified by low friction despite the distinct TSM signals between the overlayer and underlayer. Evidently, the overlayer grain has a coincident epitaxial relationship with the underlayer, in which there is a defined angle of twist in the interlayer relationship.[164] Slightly more complicated is the domain on the top part of Figure 5.4b. It exhibits similar TSM signal strength to the underlying first layer, which reflects either a commensurate or

incommensurate (coincident or non-epitaxial) relationship as discussed above. In Figure 5.4a, the friction contrast of the same domain clearly shows low friction, which rules out non-epitaxy. In addition, the TSM signal indicates that the crystallographic orientations of both layers are close to (*ii*) as in Figure 5.1a, suggesting an absence of coincident registry. Thus, we can determine that the homoepitaxial mode of this domain is commensurism. Such different homoepitaxial modes (commensurism, coincidence, and non-epitaxy) observed in pentacene two-layer films on PMMA agree well with our previous observation in pentacene films on SiO_2.[148] But instead of repeated TSM imaging and analysis of a large number of images at different azimuthal sample orientations, the homoepitaxial modes are more simply identified by capturing single TSM and FFM images of the same area. Only a change of scan angle by 90° is required to switch back and forth from the two imaging modes. Also, contrast variations on the sub-micrometer scale are clearly distinguished. It is also worth noting that the total signal range of FFM images is often 5-10 times larger than TSM images, and thus FFM images usually have a much higher signal/noise ratio than TSM images, yielding sharper contrast.
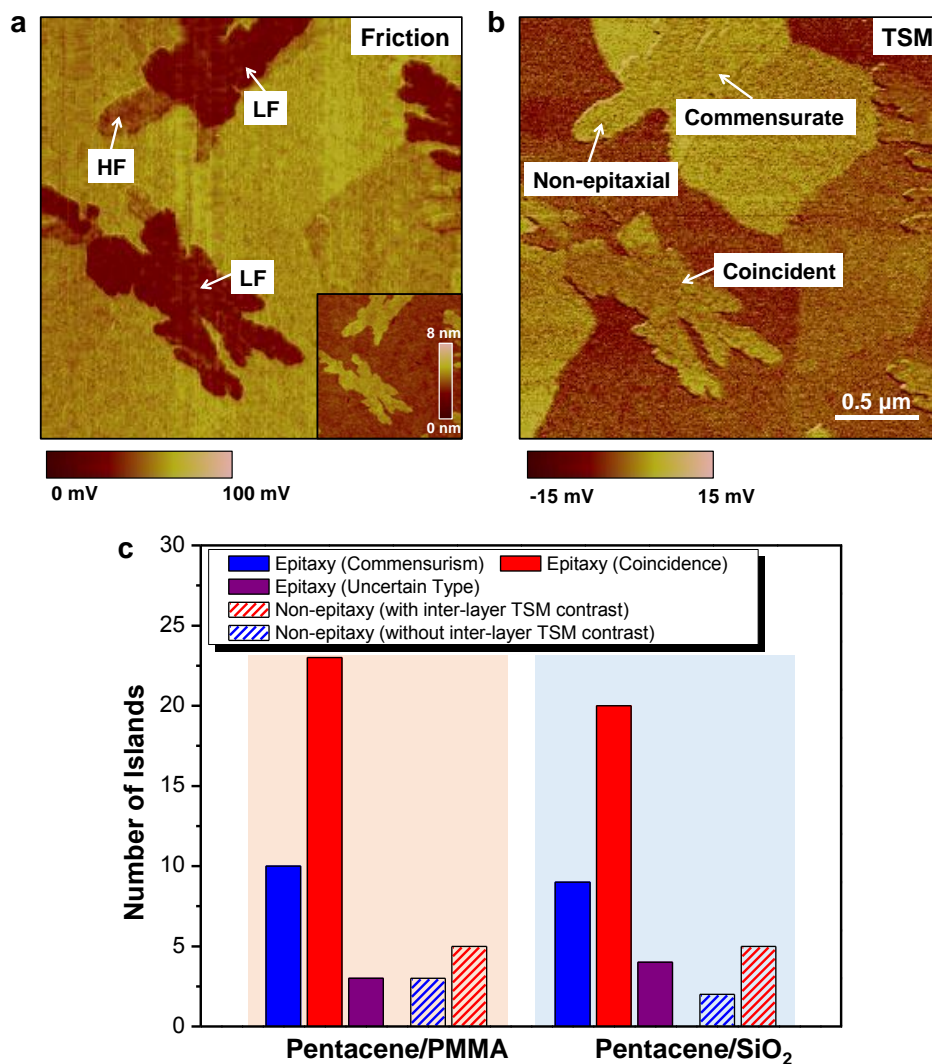
Figure 5.4 Determination of epitaxial modes with the combination of friction and TSM contrasts.
(a) Friction image of pentacene two-layer film on PMMA with epitaxial (LF) and non-epitaxial (HF) domains labeled. Inset: simultaneously obtained height image. (b) TSM image of the same film in a. Commensurate, coincident, and non-epitaxial domains are determined with the aid of friction in a. (c) Statistical analysis of different epitaxial modes adopted by pentacene second layer grains for films deposited on PMMA and SiO$_2$.

In summary, the rules for epitaxial assignments are as follows:

1. Coincidence: low friction of the overlayer domain and, simultaneously, distinguishable TSM contrast between the overlayer and the underlayer;

2. Commensurism: low friction of the overlayer domain and, simultaneously, no interlayer TSM contrast (bright on bright or dark on dark in TSM image);

3. Non-epitaxy: high friction; The TSM contrast is not important;

4. Uncertain (possible coincidence/possible commensurism): low friction of the overlayer domain and, simultaneously, no interlayer TSM contrast (intermediate on intermediate in TSM image).

With the convenience of this combined FFM/TSM route, we were able to perform a statistical analysis to examine the relative population of different homoepitaxial growth modes in the second layer of pentacene films deposited on different dielectrics. For each substrate, corresponding FFM and TSM images (about 10 pairs) acquired in random areas of pentacene bilayers from multiple depositions were studied. Note that only the *initial* homoepitaxial modes adopted by the second layer grains were counted, i.e., second layer grains growing across the first layer grain boundaries were not considered. Also, second layer grains nucleating very close to or right atop of grain boundaries in the first layer (43% of grains in pentacene/PMMA and 35% of grains in pentacene/SiO$_2$) were excluded in this analysis since the initial homoepitaxial growth mode is hard to determine. As displayed in Figure 5.4c, populations of different homoepitaxial types are determined with relatively small uncertainty and there is no apparent difference between films on PMMA and SiO$_2$. For both types of films, the majority of second layer grains are epitaxial (either commensurate or coincident), indicating that initial registry (commensurism) or partial registry (coincidence) of the second layer with respect to the first layer is generally adopted when the second pentacene layer nucleates on top of the

112

first layer grains. It is also interesting to note that the population of coincident grains is slightly more dominant.

5.5 Commensurism and Coincidence in Pentacene Bi-Layers

A better understanding of the coincident epitaxy requires knowledge of the twist angle between the second layer and the first layer. Statistical analysis was thus carried out for the coincident grains underlying Figure 5.4c to obtain the average magnitude of interlayer TSM signal difference (Δ). As shown in Figure 5.5a, Δ is a distribution with the center being very close the maximum TSM signal difference, which is the difference between the brightest and the darkest signals (40 mV in this case). According to the orientation dependence of TSM signals shown in Figure 5.1a and the uncertainty from the instrument noise, the twist angle between the overlayer and underlayer, i.e., $\Delta\theta$, is approximately 70-80°. Smaller Δ values are also obtained in coincident grains when both overlayer and underlayer deviate from the peak and valley positions in Figure 5.1a and yet $\Delta\theta$ remains the same.

The two proposed homoepitaxial modes are shown schematically in Figure 5.5c and 5.5d, respectively. It is generally accepted that thermally deposited pentacene adopts a so-called "thin film phase", which is a strained structure compared to the pentacene bulk phase.[43, 48, 52, 172, 181] The strained structure may be stabilized by the minimized pentacene-substrate area of the thin film phase; the molecules stand more upright.[52, 181] It may also be attributed to the electrostatic energy associated with the large dipole moment induced

in pentacene molecules as it is known that interfaces between pentacene/SiO_2 and pentacene/polymers exhibit strong electrostatic polarization.[180] That is, perhaps the more upright, strained pentacene growth is stabilized by electrostatic energy. Whatever the reason, the compressed state of the pentacene layer immediately adjacent to the substrate is known.[48, 52, 181] The crystallography of the second layer, however, has not been explicitly determined to the best of our knowledge, though an abrupt change of the lattice parameters is unlikely. For lack of a better alternative, we assume that the second layer adopts the same structure as the first layer. Therefore, in commensurate epitaxy, as shown in Figure 5.5c, the [100] direction of the overlayer aligns precisely with that of the underlayer. In coincident epitaxy, however, the [100] directions of the overlayer and underlayer exhibit a twist of approximately 70-80° as determined above. Geometrically, in order to realize such a partially registered interlayer relationship, the [110] diagonal of the second layer aligns with the [$\bar{1}$10] diagonal of the first layer, as depicted in Figure 5.5d. Note in Figure 5.5b that the angle between the two diagonals in a monolayer unit cell is 76°. This alignment can also be justified by the maximized interlayer TSM contrast observed in a large number of coincident domains, which, according to Figure 5.1a, occurs when the orientations of the two layers correspond to (*ii*) and (*iv*), respectively. Since such a coincident twist epitaxy is commonly found to compete with commensurism in pentacene two-layer films, we speculate that it might relieve some strain in the compressed pentacene thin film structure. Regardless, both commensurate and coincident epitaxial modes represent registry between the pentacene overlayer and underlayer, and are more energetically favorable in the growth of pentacene bilayers on dielectrics.

114
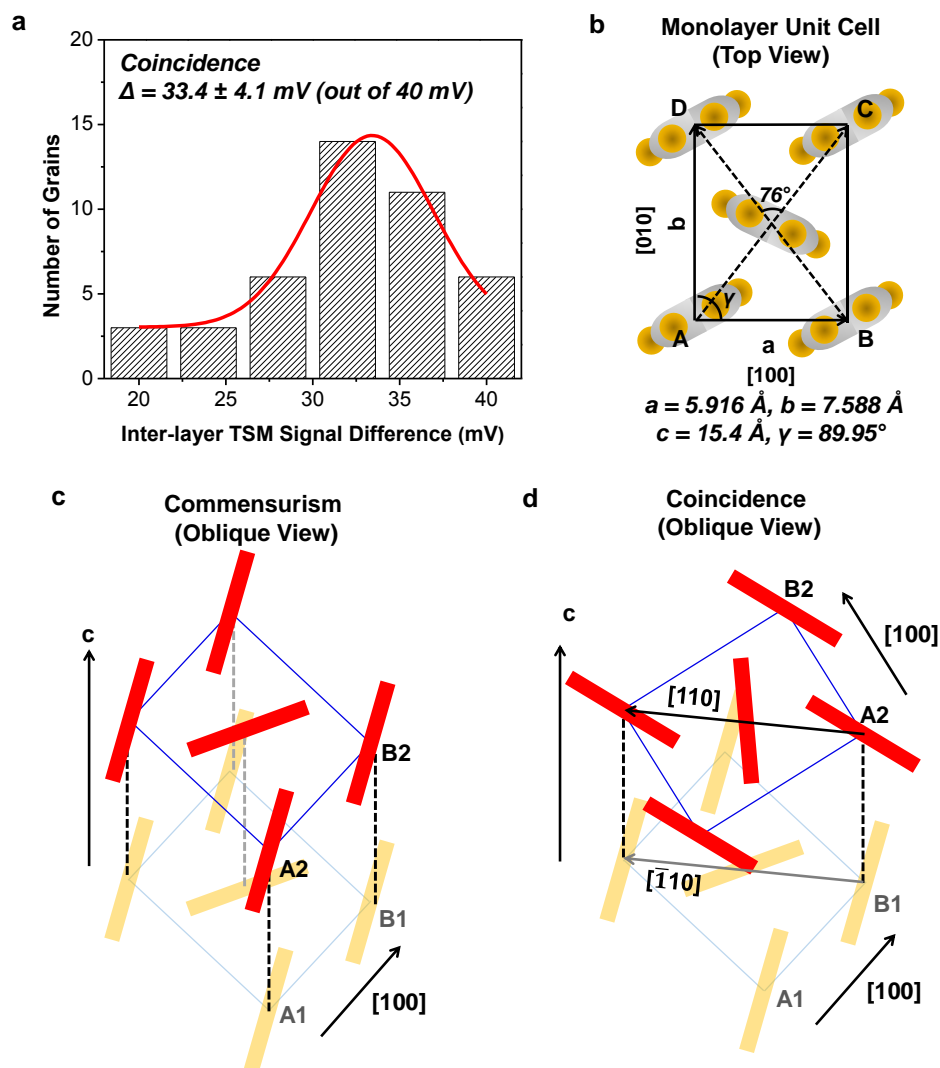
Figure 5.5 Commensurism and coincidence epitaxy adopted by pentacene second layer grains.
(a) Interlayer TSM contrast for commensurate grains in Figure 4(c). The total TSM signal difference (from the brightest to the darkest) is 40 mV. The average magnitude of TSM signal difference between the overlayer and underlayer (Δ) is close to 0 mV for commensurate second layer grains (errors are within the instrument noise floor). (b) Interlayer TSM contrast in coincident grains in Figure 4(c). The total TSM signal difference is 40 mV. Δ is close to 40 mV. (c) Top view of pentacene monolayer unit cell structure. [Ref. 45 & 47] (d) Oblique view of commensurism in pentacene bilayers. All the second layer molecules align precisely with the first layer ones. (e) Oblique view of coincident epitaxy in pentacene bilayers. There is a 70-80° twist between pentacene second layer and first layer such that there is only partial registry between the two layers, i.e., the [110] diagonal of the second layer aligns with the [$\bar{1}$10] diagonal of the first layer.

5.6 Lattice Imaging of Pentacene Bi-Layers

As an attempt to explicitly determine homoepitaxial types in complementary with the combined TSM/FFM method, significant efforts were made to obtain lattice-resolved images of individual pentacene layers by imaging, e.g., in-liquid contact mode atomic force microscopy (AFM).[182-186] Dating back to 1989, AFM was found to possess lattice-resolved imaging capability when operating in water.[182] As is known, both the AFM tip and the sample are typically covered with an adsorbed water layer and other contaminates in air, which produce a large adhesion force when the tip and sample are in contact.[187, 188] This force thus makes the contact area between the tip and sample too large to achieve high resolution. However, when both the cantilever and the sample are immersed in an isotropic liquid environment as illustrated in Figure 5.6a, the large adhesion force is eliminated and the applied force to the sample could be better known and controlled. Molecular resolution or lattice resolution is thus possible. Extensive lattice resolution imaging has been reported by a number of research groups.[183-185, 189] For example, Ward and colleagues have imaged crystalline growth of organic metals on electrode surfaces.[186, 189, 190] Lattice imaging has also been exploited to investigate Langmuir-Blodgett films,[191] self-assembled monolayers (SAMs),[192] etc. But to the best of our knowledge, lattice imaging in liquid on vapor deposited organic semiconductor thin films has never been reported.
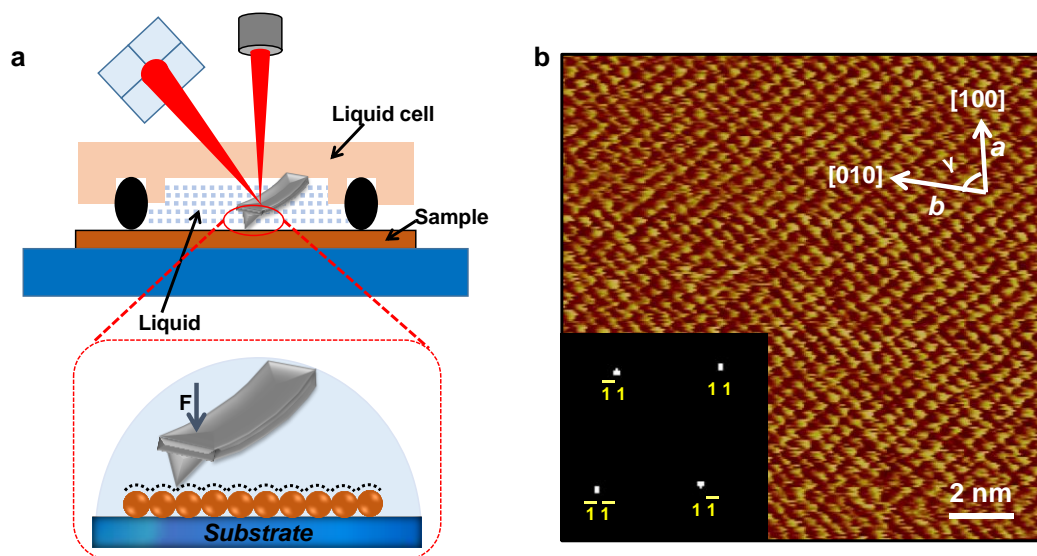
Figure 5.6 In-liquid lattice imaging of pentacene bi-layers.
(a) Schematic of in-liquid contact mode lattice imaging. Both the cantilever and the sample are immersed in a liquid cell filled with liquid. Compared to conventional imaging in air, the liquid provides an isotropic environment which eliminates the large capillary force formed upon the contact of the probe and sample. (b) An example of lattice image (friction mode) obtained for the pentacene second layer. The inset shows a 2D FFT pattern of the lattice image with less intense signals filtered. The lattice parameter extracted from this example is a ~5.7 Å, b ~6.9 Å, and γ ~77°. The liquid used to obtain this image was ethanol.

Figure 5.6b shows that it is possible to resolve lattice structures of thermally deposited pentacene films by careful optimization of the imaging conditions. Specifically, ethanol was used as it is a common, less-toxic, and less-corrosive solvent. DI water was also evaluated since it better preserves pentacene film integrity compared to ethanol. The trade-off of water lies in the much larger tip-sample attractive interactions, leading to noisy images. The inset of Figure 5.6b displays the 2-D fast Fourier transform (FFT) spectrum of the corresponding lattice image. The most intense signals form an oblique ring structure, which shows the symmetry of the reciprocal lattice of pentacene. The lattice parameters extracted from the reciprocal lattice are a: 5.7 Å, b: 6.9 Å, and γ: 77°,

respectively. In comparison, the lattice parameters for pentacene thin film phase determined by grazing incidence X-ray diffraction (GIXD) are a: 5.9 Å, b: 7.8 Å, and γ: 90°.[52] Apparently, the unit cell structure obtained from lattice imaging is distorted, arising from the scanner drift and the surface/tip contaminates.
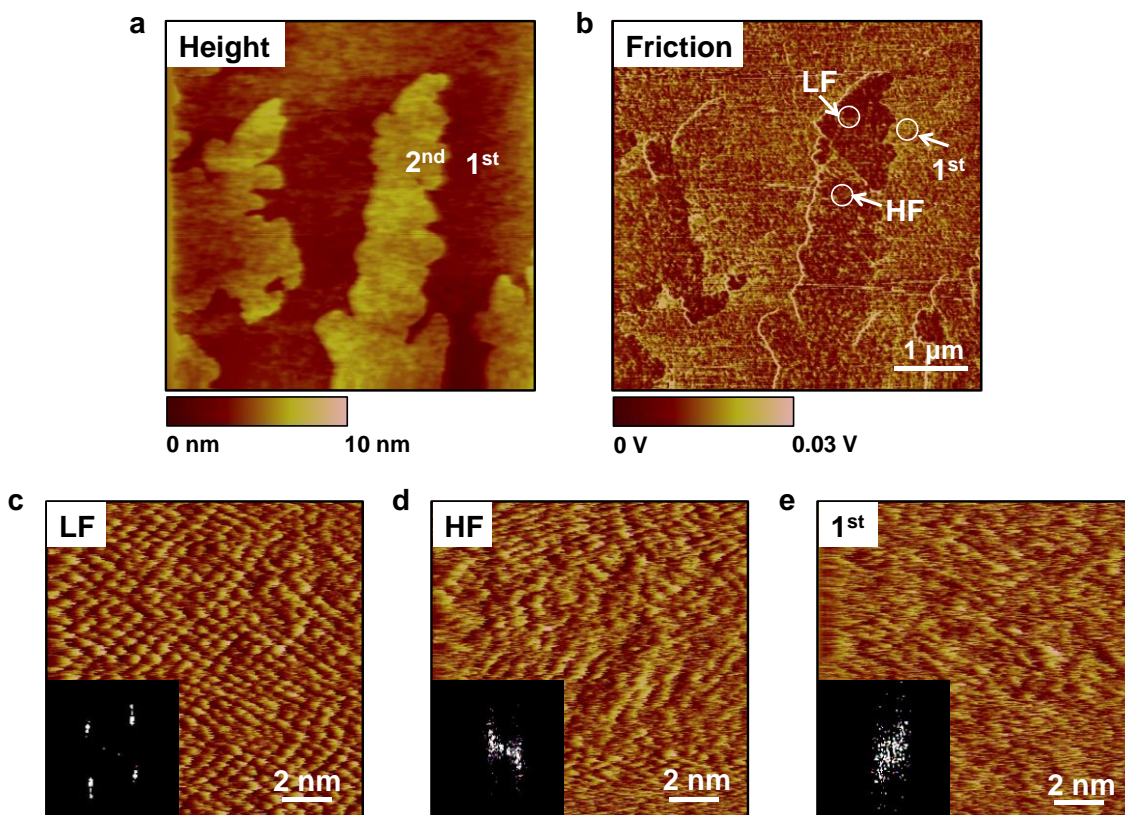
Figure 5.7 Height, friction, and lattice images of pentacene bi-layers grown on SiO$_2$.
(a) Height image of pentacene two-monolayer films grown on SiO$_2$. (b) Simultaneously obtained friction image. It is interesting to notice that the HF and LF regions can still be distinguished in liquid but the magnitude of friction contrast significantly decreased because the applied force in this case was smaller. The circled areas were zoomed in to obtain the lattice images. (c) Lattice image of LF domain exhibiting reasonable resolution. The 2D FFT spectrum shows symmetry reasonably close to the reciprocal lattice of pentacene monolayer structure. The lattice parameters determined from the FFT spectrum are ~10% off compared to that of the monolayer structure. Note that friction mode was consistently employed in this work since it typically gives better lattice resolution. (d) Lattice image of HF domain. The lattice cannot be clearly resolved and the 2D FFT image shows noisy signals. (e) Lattice image of the first layer. The lattice resolution is also poor similar to that in (d).

118

Furthermore, we found that given the substantial measurement noise, lattice-resolved images were only obtained from the low friction domains of the second layer, but not from any other domains of the film regardless of how optimized the imaging condition was, as shown in Figure 5.7. This result is consistent with the epitaxial nature of the low friction domain, but unfortunately we were not able to unambiguously identify different homoepitaxial modes by direct lattice imaging.

5.7 Conclusion

In conclusion, we have carried out concurrent FFM and TSM imaging to investigate homoepitaxy in pentacene bilayers thermally deposited on two common dielectric substrates, PMMA and SiO_2. The two SPM imaging modes are mutually complementary and integration of the two enables convenient identification of different homoepitaxial modes in pentacene second layer domains. It is observed that pentacene second layer grains consistently exhibit a mosaic of homoepitaxial modes regardless of the substrate type and deposition condition. The majority of the second layer grains adopt a commensurate or coincident epitaxial relationship with the first wetting layer. Coincident epitaxy, characterized as a crystallographic twist between the overlayer and underlayer, is comparable to commensurism in all the investigated films. Collectively, we demonstrate that homoepitaxial growth modes contribute significantly to the microstructural inhomogeneity in pentacene crystalline thin films deposited on dielectrics. With the combined FFM/TSM technique, such microstructural motifs can be feasibly identified

such that a deeper understanding of growth and structure-property relationships is possible.

5.8 Experimental

5.8.1   Sample Preparation

All pentacene films were prepared by thermal evaporation of the source material pentacene (Fluka, 99.8%) onto different substrates with chamber pressure $\leq 2\times 10^{-6}$ Torr and a deposition rate ~0.01 Å/sec. A quartz crystal microbalance (QCM) was used to control the film coverage by targeting ~50-60% coverage for pentacene sub-monolayers and ~120-130% for pentacene two-layer films. The SiO_2 substrates used in this study were thermal oxides grown on p-doped Si with a thickness of 200 nm. The substrates were cleaned by acetone prior to use. Poly(methyl methacrylate) (PMMA) substrates were prepared by spin coating corresponding polymer solutions (10wt% PMMA/1,2-dichloroethane) onto SiO_2 (2000 rpm, 30 sec) and baking at 90 °C for 1 hour to remove residual solvent. According to atomic force microscopy (AFM) measurements, all the spin coated PMMA films have thicknesses around 20-50 nm. Two different substrate temperatures were selected (27 °C and 50 °C) for different depositions.

5.8.2   Friction Force Microscopy and Transverse Shear Microscopy

FFM is a contact mode SPM technique where the local variations in the sliding friction between the probe and the sample are mapped together with topography. The fast scan direction of the probe is perpendicular to the long axis of the cantilever. TSM is a variant of FFM which has the fast scan direction parallel to the long axis of the cantilever. The local variations in transverse shear force between the probe and the sample are thus imaged along with topography. All FFM and TSM measurements were performed with a Veeco Nanoscope IIIA Multimode 5 Scanning Probe Microscope inside an argon-filled glove box with oxygen level <5 ppm. The probes used for all measurements were silicon rectangular-shaped cantilevers with integrated contact mode probes fabricated by Mikromasch, USA (HQ:CSC37/Al BS, force constant ~0.3 N/m). The tip scan rate for a 20×20 μm image was 20 μm/s. All the FFM and TSM images shown in the figures are the forward trace scans. All images were analyzed by freeware *Gwyddion*.

5.8.3   In-liquid Lattice Imaging

In-liquid lattice imaging was carried out on an Agilent 5500 AFM/SPM microscope with a PicoScan 3000 controller and a liquid cell. Contact mode was adopted in this imaging technique with soft silicon nitride V-shaped cantilevers with integrated contact mode probes fabricated by Mikromasch, USA (HQ:CSC38/Al BS, force constant ~0.03 N/m). The probes were plasma cleaned prior to use.[44] Different liquids were used

including ethanol, DI water, and 50wt% ethanol-water mixture for the purpose of good lattice resolution or good film integrity, or both. The applied force used was around 1-5 nN and the imaging speed for a 20 nm × 20 nm was about 20-30 Hz. All lattice images were analyzed by freeware *Gwyddion.*

Chapter 6 Strain Effects on the Work Function of an Organic Semiconductor

6.1 Overview

Establishing fundamental relationships between strain and work function (WF) in organic semiconductors is important not only for understanding the electrical properties of organic thin films, which are subject to both intrinsic and extrinsic strains, but also for developing flexible electronic devices. Here we investigate tensile and compressive strain effects on the WF of rubrene single crystals. Mechanical strain induced by thermal expansion mismatch between the substrate and rubrene is quantified by X-ray diffraction. The corresponding WF change is measured by scanning Kelvin probe microscopy. The WF of rubrene increases (decreases) significantly with in-plane tensile (compressive) strain, which agrees qualitatively with density functional theory calculations. An elastic-to-plastic transition, characterized by a steep rise of the WF, occurs at ~0.05% tensile strain along the rubrene π-stacking direction. The results provide the first concrete link between mechanical strain and the WF of an organic semiconductor and have important implications for understanding the connection between structural and electronic disorder (charge traps) in soft organic electronic materials. This work is published as *Y. Wu, A. R. Chew, G. Rojas, G. Sini, A. Belianinov, S. V. Kalinin, H. Li, C. Risko, J.-L. Bredas, G. Haugstad, A. Salleo and C. D. Frisbie, Nature Communications 7, (2016).*

6.2 Introduction

Strain is known to play a critical role in the physical properties of many conventional inorganic semiconductors. For example, strain modifies the band structure and carrier mobilities of group IV materials including Si and Ge, as well as III-V materials such as GaAs.[193-197] Consequently, controlled introduction of strain is widely employed to engineer the transport and optical properties of these semiconductors for enhanced device performance.[198, 199] Similarly, in soft organic semiconductors that serve as the active components in many organic electronic devices,[2, 150, 200-202] tensile and compressive strains modify the material electronic properties and function. An intriguing example is the observation by Bao and colleagues that the charge mobility in films of the benchmark organic material TIPS-pentacene is enhanced under lattice compression.[203] Controlling and understanding strain effects is thus particularly important for device applications of organic semiconductors, especially in the area of flexible electronics, where externally applied strains are routine. Both strain-resistant and strain-sensitive device responses[204-208] are desirable in flexible circuits, and better knowledge of strain-property relationships will facilitate flexible device designs.

Importantly, better understanding of strain-electrical property relationships is also critical for theoretical models of transport in organic semiconductors. Virtually all organic semiconductor films exhibit intrinsic non-uniform strains arising from lattice or thermal expansion mismatch with the substrate, the presence of defects, or post deposition treatments such as thermal annealing.[209-212] Non-uniform strains in turn lead to variations in intermolecular electronic coupling and thus to local differences in

bandwidths and band gaps,[213, 214] i.e., "raggedy" valence (conduction) band edges, which can also create shallow charge trap (tail) states. There is therefore the intriguing possibility that residual microstrain is a significant cause of charge carrier trapping in organic semiconductors. Proving this would be a major conceptual step in clarifying the link between structural and electronic disorder, a long-sought goal for organic electronics. However, a challenge is that, as far as we are aware, the quantitative connection between electronic structure and mechanical strain has never been established in these materials.

Here we take a considerable step in this direction by measuring the effect of tensile and compressive strains on the work function (WF) of a prototypical p-type organic semiconductor for the first time. The WF is defined as the energy difference between the vacuum level (E_{vac}) and the Fermi level (E_F), i.e., WF = E_{vac} - E_F. Strain can modify E_{vac} and E_F of a semiconductor by changing the band edge positions, the dopant levels in the band gap, or the surface dipoles. Thus, strain impacts the WF. In a p-type crystal of π-conjugated organic molecules in which the Fermi level is pinned (fixed doping level), strain effects on E_F can be pictured, to a first approximation, as follows: compressive strains increase the frontier orbital (e.g., HOMO) overlap of adjacent molecules, leading to a wider valence band,[213] a higher E_F, and a lower WF. Conversely, tensile strains increase the separation between molecules, lowering orbital overlap and decreasing valence bandwidth and E_F, thus increasing the WF. Note that with fixed doping level, the WF change can be directly translated to the change of the ionization potential (IP = E_{vac} -

E_{HOMO}), which is a more commonly adopted term for describing the electronic structure of intrinsic organic semiconductors.

Our measurements focus on p-type rubrene single crystals, which serve as a model material platform for many fundamental studies of organic semiconductor physics due to their exemplary transport properties, i.e., the highest reproducible charge-carrier mobilities to date have been achieved in single crystal rubrene field-effect transistors (FETs).[33] By adhering thin rubrene crystals onto substrates with coefficients of thermal expansion (CTEs) distinctly different from rubrene and varying the temperature, we systematically induce large and controlled tensile or compressive strains in rubrene crystals and quantify the elastic portion by X-ray diffraction (XRD). The corresponding WF of rubrene, measured by temperature-dependent scanning Kelvin probe microscopy (SKPM), is found to increase (decrease) with the in-plane tensile (compressive) strain. The measured changes in WF (ΔWF) are qualitatively confirmed by density functional theory (DFT) calculations, and verify that indeed small elastic strains <0.1% can lead to ΔWF surpassing the room temperature thermal energy kT = 25 meV. Furthermore, we find that the onset of tensile plastic strain leads to even larger increases of WF with strain. These findings constitute a definitive link between structural deformation and electronic disorder in a model organic semiconductor.
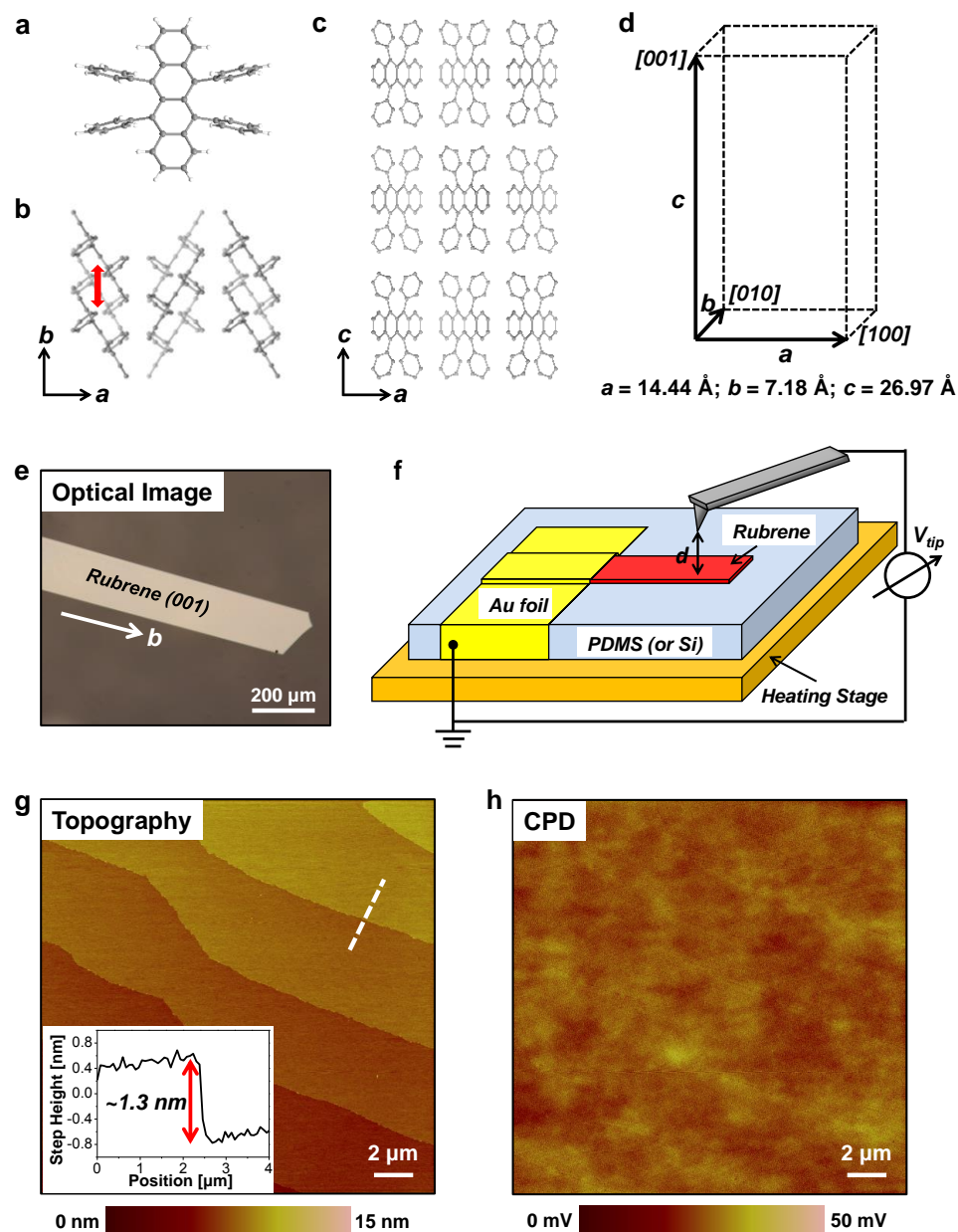
Figure 6.1 Crystal structure and SKPM measurement of rubrene single crystals.
(a) Molecular structure of rubrene. (b) Crystal structure in the *a-b* plane; red arrow: π-stacking interaction. (c) Crystal structure in the *a-c* plane. (d) Orthorhombic structure and lattice parameters of rubrene. (e) Optical micrograph of as-grown rubrene crystal. (f) SKPM setup for CPD measurement. The sample sits on top of a heating stage and is grounded through gold foil. The lift height (*d* = 50 nm) is used in the "interleave" pass. (g) Topography of rubrene single crystal shows typical terrace structure and each terrace has height corresponding to one molecular layer. Inset: Step height profile of the dashed line. (h) CPD image obtained simultaneously with topography shows nearly homogeneous CPD across the surface.

6.3 Rubrene Single Crystals

The crystal structure of rubrene single crystals grown from the vapor phase is shown in Figure 6.1a-d. The crystals adopt an orthorhombic structure and slipped π-stack packing motif with the π-stacking direction along the b axis.[59] The optical micrograph (Figure 6.1e) shows a lath-like single crystal with the largest facet being the (001) plane and the longest direction aligned with the b axis. Thin rubrene crystals (~2 μm) are then laminated on poly(dimethylsiloxane) (PDMS) or silicon (Si) substrates for XRD and SKPM measurements. PDMS is chosen for its significantly larger CTE (~300×10^{-6} K^{-1}) than that of rubrene (~10-80 $\times$ 10^{-6} K^{-1})[215, 216] in order to induce tensile strain in laminated rubrene crystals upon increasing the temperature. Si, on the other hand, is chosen to induce compressive strain since it has a much smaller CTE (3-4 $\times$ 10^{-6} K^{-1}) than that of rubrene. Table 6.1 lists the CTE values of rubrene, PDMS, and Si.

Table 6-1 CTE of rubrene, PDMS, and Si.

	Rubrene[215]			PDMS[217]	Si[218]
	a	b	c		
CTE (10^{-6} K^{-1})	78	16	20	300	3-4

Figure 6.1f shows the scheme of the SKPM measurement, which operates in a two-pass "lift mode" to acquire images of topography and the contact potential difference (CPD) between the tip and the sample.[219] The CPD is related to the WF of the tip and the sample by $q\text{CPD} = \text{WF}_{tip} - \text{WF}_{sample}$, where q is the elementary charge. Therefore, with the same tip acting as the reference, the measured CPD change reflects the WF change of

the sample, i.e., $q\Delta\text{CPD} = -\Delta\text{WF}_{\text{sample}} = -\Delta\text{WF}$.[22, 180] Typical topography and CPD images

of a rubrene (001) surface obtained by SKPM at room temperature are shown in Figure

6.1g and 6.1h, respectively. The topography image shows a surface with several

molecularly flat terraces, which extend over a distance of several micrometers. The

height of each terrace obtained from the profile of the white dashed line, as shown in the

inset of Figure 6.1g, is approximately 13 Å, which coincides with one-half of the c axis

unit cell parameter. This is in agreement with previous observations of rubrene molecular

steps and confirms that there are two nonequivalent molecular planes in the rubrene

crystal unit cell.[220] The CPD map (Figure 6.1h), on the other hand, is almost featureless.

The local CPD variations, characterized by the root-mean-square (RMS) CPD roughness,

are less than 3 mV for this 20×20 μm^2 area. The CPD map thus suggests that the rubrene

(001) surface is electrostatically homogeneous, in accordance with the high structural

order of rubrene single crystals. It also demonstrates the high voltage resolution of

interleave-based SKPM (about 1 mV), which allows small WF changes of the sample to

be resolved.

6.4 Strain Quantification

In order to quantify the elastic strain induced in rubrene crystals, temperature-

dependent XRD measurements were carried out. By recording the 2θ shifts of rubrene

(0012), (113), and (313) peaks as a function of temperature and calculating the

corresponding d-spacings, d_{0012}, d_{113}, and d_{313}, the total elastic strains (ε^{total}) along the

rubrene *a*, *b*, and *c* axes at different temperatures were computed (see Appendix A3), which are composed of both induced mechanical strain ($\varepsilon^{elastic}$) and thermal strain ($\varepsilon^{thermal}$), i.e., $\varepsilon^{total} = \varepsilon^{elastic} + \varepsilon^{thermal}$.
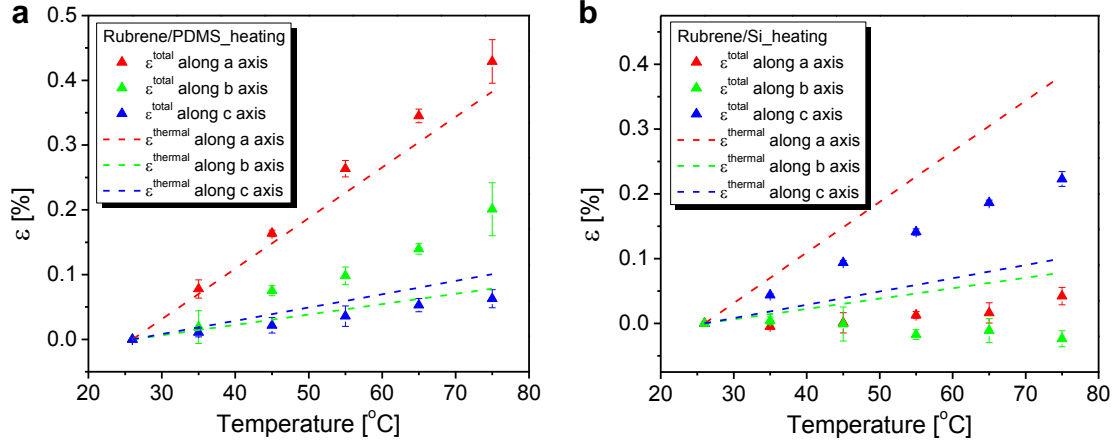
Figure 6.2 Total elastic strain in rubrene single crystals laminated on PDMS and Si at different temperatures quantified by XRD.
(a) Average total elastic strains ε^{total} of rubrene along *a*, *b*, and *c* axes as a function of temperature for crystals laminated on PDMS, which are different from the corresponding thermal strains $\varepsilon^{thermal}$ expected for free rubrene crystals (dashed lines). (b) Average ε^{total} of rubrene along *a*, *b*, and *c* axes as a function of temperature for crystals laminated on Si, different from the corresponding $\varepsilon^{thermal}$ predicted for free rubrene crystals (dashed lines).

Figure 6.2a and 6.2b show the average ε^{total} for rubrene on PDMS and rubrene on Si, respectively, when the samples were heated from room temperature to 75 °C. Also shown are the calculated thermal strains $\varepsilon^{thermal}$ for free crystals using the reported CTEs.[215] Clearly, the two types of samples show distinct strain behaviors with increasing temperature. In Figure 6.2a, rubrene crystals laminated on PDMS exhibit slightly larger ε^{total} along the *a* axis and much larger ε^{total} along the *b* axis compared to $\varepsilon^{thermal}$ estimated for free crystals. ε^{total} along the *c* axis of rubrene on PDMS, however, is slightly smaller than the estimated $\varepsilon^{thermal}$ for free crystals. On the other hand, crystals on Si show

essentially the opposite behavior, namely much smaller ε^{total} in the a-b plane and much larger ε^{total} along the c axis than the corresponding $\varepsilon^{thermal}$ predicted for free rubrene.
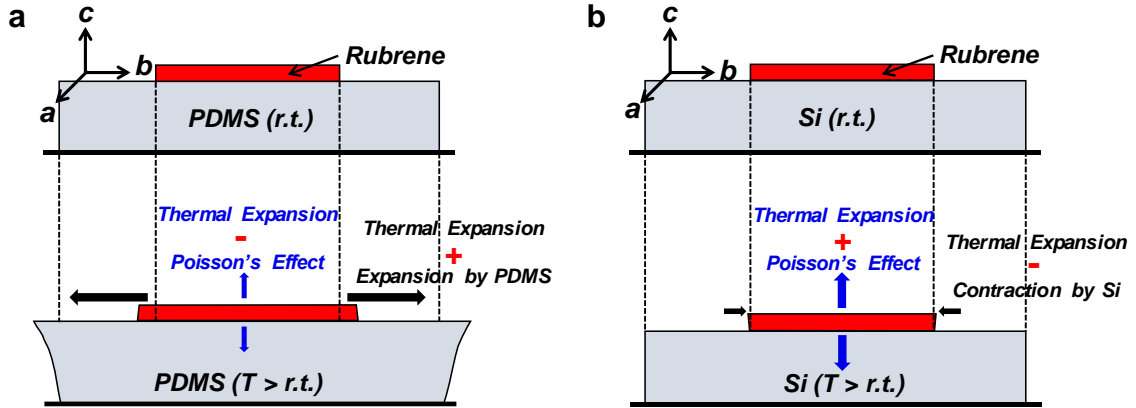
Figure 6.3 Illustration of strain components for rubrene on PDMS and rubrene on Si.

Such different strain states for rubrene on PDMS and rubrene on Si are explained by the schematics in Figure 6.3a and 6.3b. For rubrene on PDMS, significant expansion of PDMS due to its large CTE induces tensile strains in the rubrene a-b plane, resulting in ε^{total} greater than the estimated $\varepsilon^{thermal}$ of free crystals. The difference in ε^{total} for the a and b axes with respect to the corresponding $\varepsilon^{thermal}$ may be attributed to the anisotropic CTE of rubrene,[215, 216] i.e., CTE along the a axis ($\sim78 \times 10^{-6}$ K^{-1}) is significantly larger than that along the b axis ($\sim16 \times 10^{-6}$ K^{-1}), which leads to anisotropic CTE mismatch between the crystal and PDMS. Furthermore, as a result of the Poisson effect, the substrate-induced in-plane tensile strain in rubrene exerts a compressive component in the out-of-plane direction, or the c axis. Therefore, ε^{total} measured in the c axis is smaller than the predicted $\varepsilon^{thermal}$ if the crystal only undergoes thermal expansion.

131

In contrast, the Si substrate has negligible expansion (~0.015%) within the temperature range of interest such that the thermal expansion in the *a-b* plane of rubrene is largely constrained. The *a* and *b* axes experience compression induced by the substrate, offsetting thermal expansion and thus leading to very small ε^{total}. Similarly, due to the Poisson effect, the compressive strain creates tension in the *c* axis, making ε^{total} along the *c* axis much larger than the *c*-axis thermal expansion expected for free crystals.

The overall tension and compression states of rubrene crystals laminated on PDMS and Si, respectively, are illustrated quantitatively by the percentages of unit cell volume expansion as shown in Figure 6.3a. Rubrene on PDMS exhibits a total volume increase of 0.7%, slightly larger than that estimated for free crystals, consistent with net tension, whereas the total volume increases by only 0.25% for rubrene on Si, much smaller compared to the computed free crystal result and consistent with net compression. Though the CTE mismatch between rubrene and PDMS is greater, the magnitude of the tensile strain induced in rubrene by PDMS is actually smaller than the compressive strain induced by Si. This can be understood by the relative stiffness of rubrene compared to the substrates. Rubrene with modulus of ~15 GPa is approximately 10 times softer than Si whereas it is over 10^4 times stiffer than PDMS.[221] The complexity introduced by the compounding effects of CTE mismatch, relative stiffness, and interface adhesion is such that the elastic state of the rubrene crystal cannot be calculated and must be accessed experimentally by *in situ* XRD measurements.

132
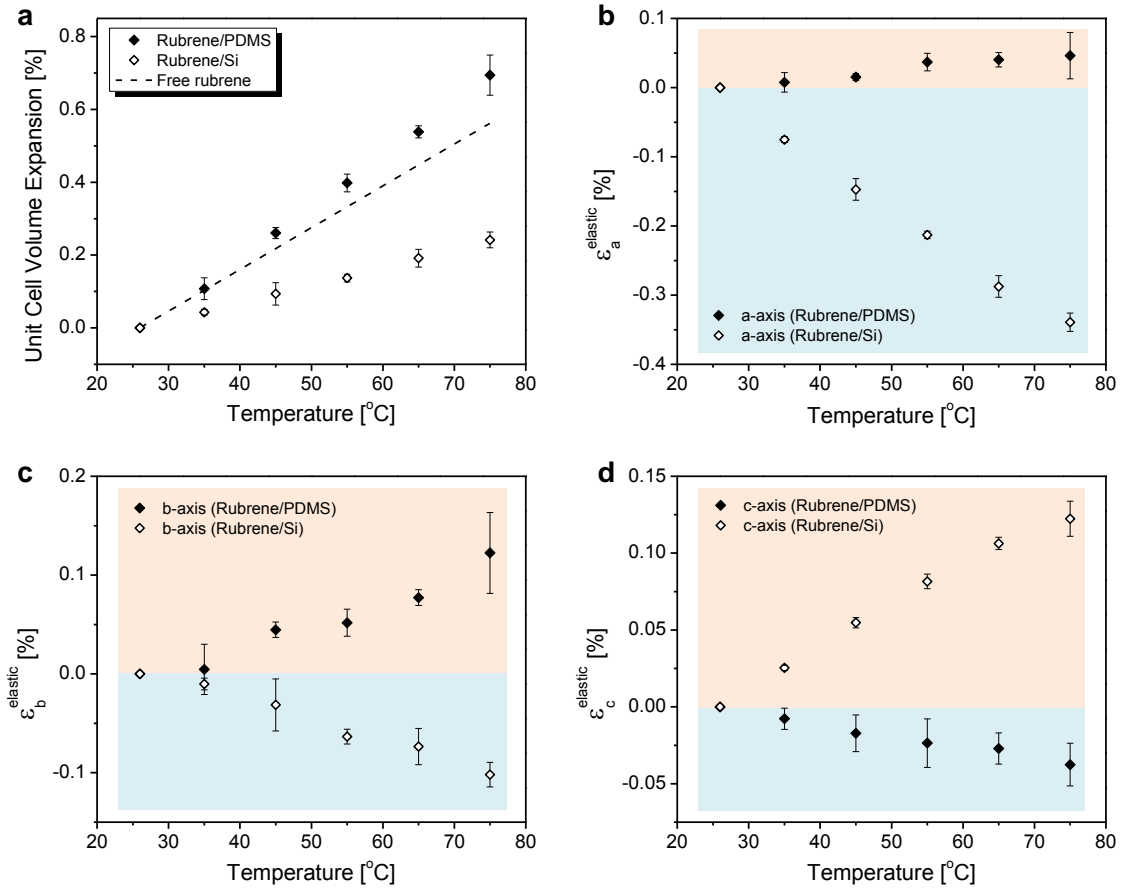
Figure 6.4 Unit cell volume expansion and substrate-induced elastic mechanical strain $\varepsilon^{elastic}$ of rubrene crystals at different temperatures.
(a) The unit cell volume expansion for rubrene crystals laminated on PDMS and Si as a function of temperature, which are compared with that expected for free crystals. (b) Average induced mechanical strain ($\varepsilon^{elastic} = \varepsilon^{total} - \varepsilon^{thermal}$) along rubrene a axis as a function of temperature for crystals laminated on PDMS and Si, respectively. (c) Average $\varepsilon^{elastic}$ along rubrene b axis as a function of temperature for crystals laminated on PDMS and Si, respectively. (d) Average $\varepsilon^{elastic}$ along rubrene c axis as a function of temperature for crystals laminated on PDMS and Si, respectively.

The net elastic mechanical strains ($\varepsilon^{elastic} = \varepsilon^{total} - \varepsilon^{thermal}$) along the three principal axes of rubrene on PDMS and Si are shown in Figure 6.4b-d. For rubrene on PDMS, tensile strain reaches ~0.05% along the a axis and over 0.1% along the b axis; the c axis compressive strain reaches ~-0.04%. For rubrene on Si, the a and b axes show large

133

compressive strain, approximately -0.35% and -0.1%, respectively; the tensile strain along the c axis reaches over 0.1%. We will show below that the differences in $\varepsilon^{elastic}$ for the two types of samples correlate with dramatically different WF changes.

6.5 Work Function Measurements

To measure the WF change of rubrene as a function of its mechanical states, SKPM as described above was carried out at different temperatures with the same tip as shown in Figure 6.5. Note that the WF change of the Pt-coated tip with temperature is not significant over the temperature range of interest because the WFs of metals typically exhibit a weak temperature dependence ($\sim 10^{-4}$ eV/K).[222]

Figure 6.5a and 6.5b show the CPD maps of rubrene crystals on PDMS and Si from room temperature to 75 ℃. As temperature increases, the CPD of the rubrene (001) surface decreases (bright to dark) on PDMS and increases (dark to bright) on Si. The CPD evolutions are illustrated quantitatively with the histograms extracted from the CPD maps at different temperatures, as shown in Figure 6.5c and 6.5d. For rubrene on PDMS (Figure 6.5c), the CPD changes by more than -200 mV from room temperature to 75 ℃, whereas for rubrene on Si (Figure 6.5d), it changes by about +120 mV across the same temperature range.
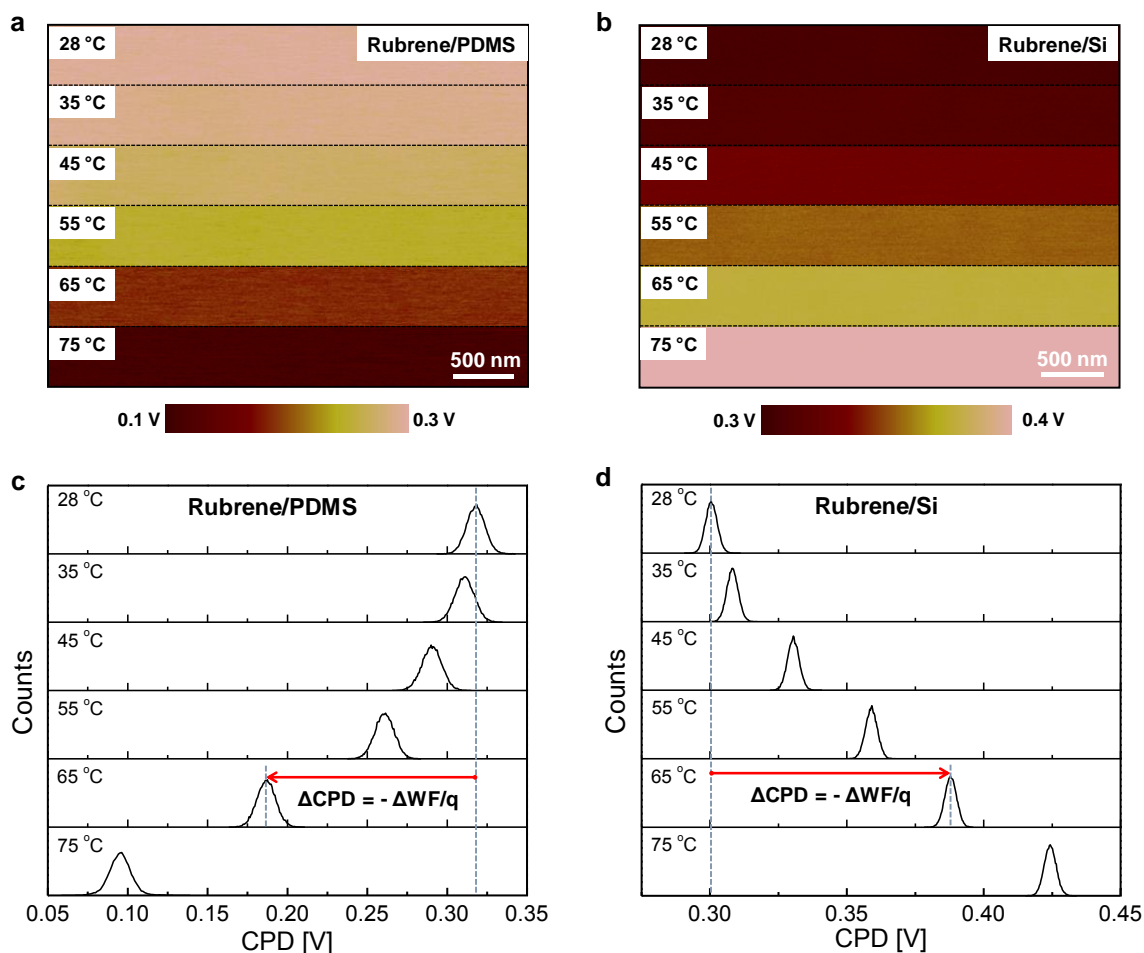
Figure 6.5 SKPM measurements of rubrene laminated on PDMS and Si as a function of temperature.
(a) CPD of rubrene on PDMS shifts from more positive (bright) to more negative (dark) when the sample is heated from room temperature to 75 °C. (b) CPD of rubrene on Si shifts from more negative (dark) to more positive (bright) when the sample is heated from room temperature to 75 °C. (c) CPD histograms extracted from images in panel a. ΔCPD, indicated by the red arrow, is defined as the change of CPD at any elevated temperature from that at room temperature, i.e., ΔCPD = CPD(T) – CPD(r.t.). (d) CPD histograms extracted from images in panel b.

By averaging multiple measurements from multiple samples, the average change in WF ($\Delta WF = -q\Delta CPD$) as a function of temperature is plotted for rubrene on PDMS (Figure 6.6a) and rubrene on Si (Figure 6.6b), respectively, for samples undergoing consecutive heating and cooling cycles. As shown in Figure 6.6a, the WF of rubrene

135

increases (ΔWF > 0) with increasing temperature on PDMS and there is an evident

transition when the temperature is close to 50 ºC. First, the WF increases only slightly

from room temperature to ~50 ºC and then above 50 ºC it increases much more steeply.

As will be discussed later, we attribute the slope change to the elastic-to-plastic

transition. Upon cooling, the WF of rubrene decreases continuously (ΔWF < 0) and there

remains a large hysteresis of ~100 meV upon returning to room temperature. An opposite

trend is observed in rubrene crystals on Si, as shown in Figure 6.6b. The WF of rubrene

decreases (ΔWF < 0) with increasing temperature, and unlike rubrene on PDMS, there is

no obvious slope change upon heating and the hysteresis between heating and cooling is

almost negligible: the WF comes back to its original value at the end of the cycle.

Overall, Figure 6.6 demonstrates that changes in WF are significant for both types of

samples and there is a qualitative difference in behavior for rubrene on PDMS and
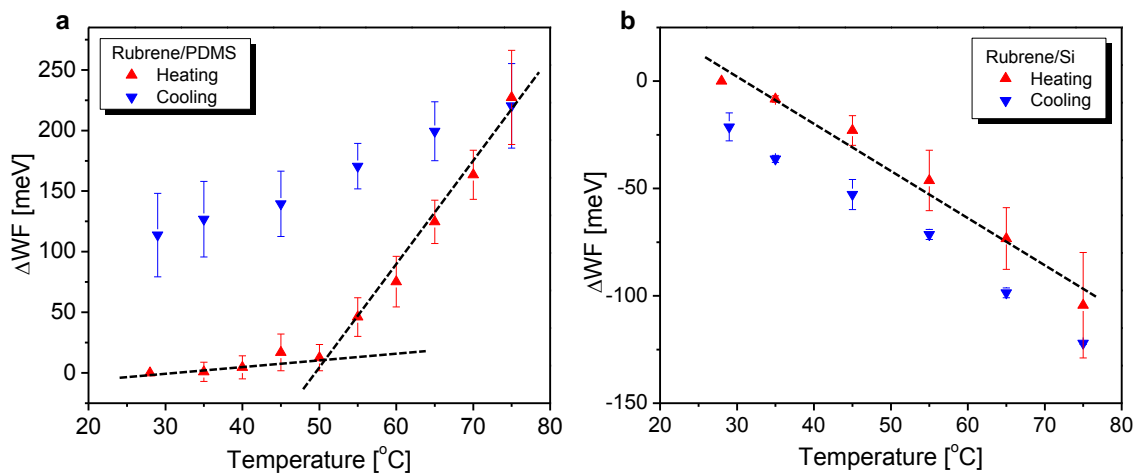
rubrene on Si.

Figure 6.6 Average ΔWF of rubrene as a function of temperature for rubrene on PDMS and rubrene on Si.

136

6.6 Strain-Work Function Relationship and the Origin

Figure 6.7 illustrates ΔWF as a function of $\varepsilon^{elastic}$ (tensile and compressive) in rubrene. ΔWF is plotted versus the *b* axis elastic strain for simplicity because it is reasonable to suppose that the relative significance of mechanical strains along different axes is positively correlated with the strength of intermolecular interactions, i.e., *b* axis (π-stacking direction) > *a* axis >> *c* axis. It is evident from Figure 6.7 that WF increases significantly with tensile strain and decreases with compressive strain, and that the changes can be much greater than *kT* (25 meV) at room temperature. A similar trend of the WF change has been observed or predicted in strained Si and graphene.[223-225]
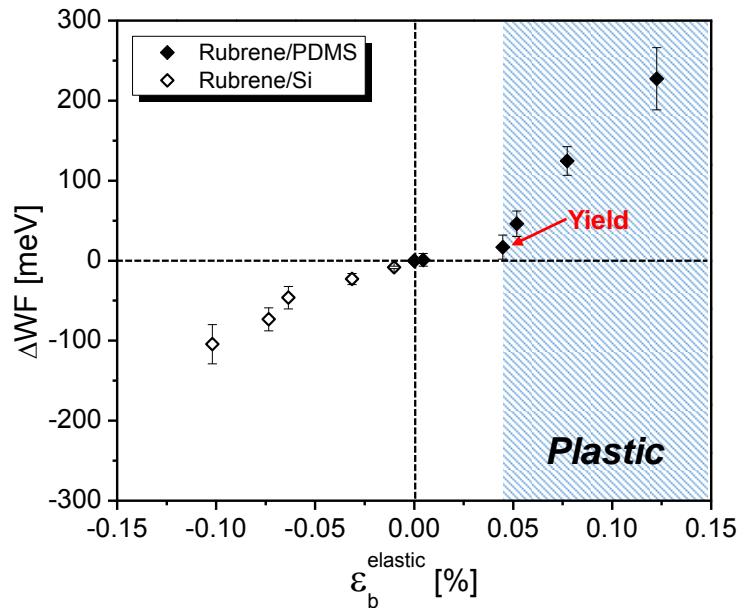
Figure 6.7 ΔWF as a function of substrate-induced $\varepsilon^{elastic}$ (tensile and compressive strain) along the *b* axis.
The WF increases with tensile strain and decreases with compressive strain. Note that ΔWF in the shaded region is mainly a result of plastic deformation instead of elastic tensile strain.

137

We attribute the measured ΔWFs to the substrate-induced mechanical strains $\varepsilon^{elastic}$ in rubrene crystals - instead of intrinsic changes with temperature or surface contamination - for several reasons. First, ΔWF is completely opposite for rubrene on PDMS versus rubrene on Si even though they experience the same temperature change. This rules out temperature as the dominating factor for ΔWF. Second, although in general the WF may be affected by surface contamination, it is unlikely to result in the systematic WF trends we observed, including the hysteresis in rubrene on PDMS. Third, we performed static level ($T = 0$ K) density functional theory (DFT) calculations of ΔWF as a function of strain as is shown in Figure 6.8a and 6.8b. Although they do not match quantitatively, the calculations predict the same signs for ΔWF as observed experimentally and thus qualitatively support our conclusion that ΔWF is dominated by mechanical strain (see Appendix A3).

To estimate ΔWF by DFT, the evolution of the valence band maximum (VBM) and the potential energy of an electron at the vacuum level (E_{vac}) were calculated based on the crystal structures of rubrene under the experimentally-attained mechanical strains; we set $WF = E_{vac} - E_F \approx E_{vac} - VBM$ such that $\Delta WF \approx \Delta E_{vac} - \Delta VBM$. This definition of WF is justified because we expect E_F of rubrene to lie closer to the VBM and to track the VBM because of Fermi level pinning or partial pinning, i.e., the offset between E_F and VBM is set by the natural p-type doping of as-grown rubrene. From Figure 6.8a and 6.8b, it is clear that the signs of the calculated ΔWF are determined by ΔVBM. Further, the calculated ΔVBM is consistent with qualitative expectations, namely that tensile strain decreases HOMO-HOMO (π-π interaction), lowering the VBM and thus increasing the

138

WF (ΔWF > 0). Compressive strain, on the other hand, increases the π-π interaction, which increases the VBM and decreases the WF (ΔWF < 0).
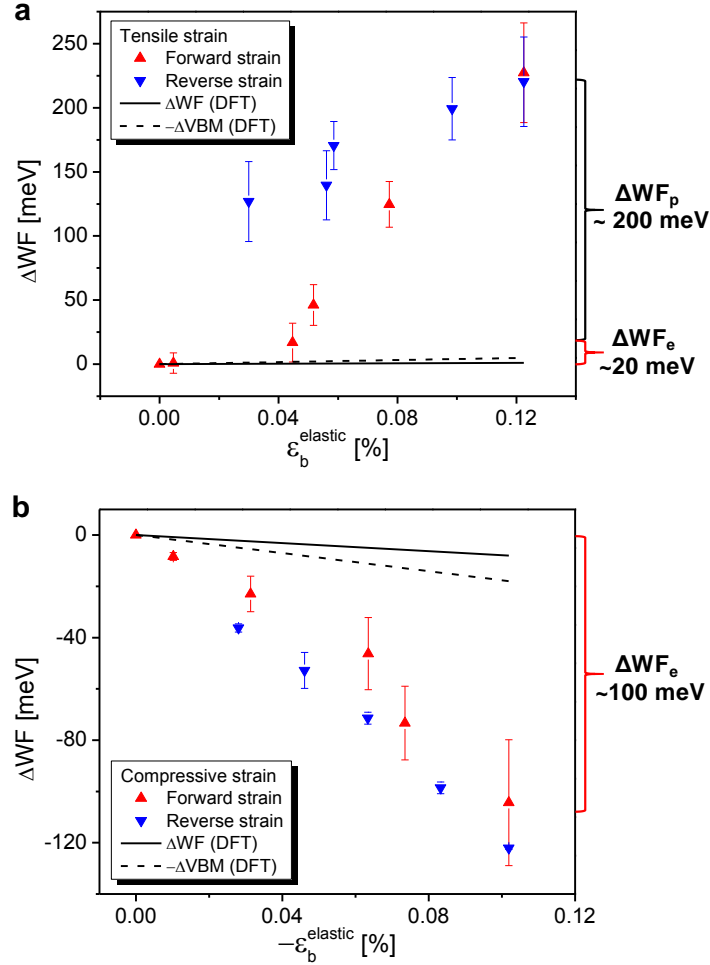
Figure 6.8 ΔWF as a function of $\varepsilon^{elastic}$ for forward and reverse strains.
(a) ΔWF as a function of elastic tensile strain for forward and reverse strains. There is an elastic-to-plastic transition characterized by a sudden rise in ΔWF with strain. There is a large hysteresis of ΔWF, indicating the effect of plastic deformation. The DFT calculation results are shown by the dashed line (-ΔVBM) and the solid line (ΔWF). The calculated -ΔVBM and ΔWF slightly increase with elastic tensile strain, a trend that qualitatively agrees with the experimental results. The quantitative disagreement between the calculations and the experimental results in the high-strain regime is attributed to plastic deformation which is not considered in the calculations. (b) ΔWF as a function of elastic compressive strain for forward and reverse strains. The WF decreases with strain smoothly and no apparent elastic-to-plastic transition is observed. There is negligible hysteresis of ΔWF. The calculated -ΔVBM and ΔWF decrease with elastic tensile strain, in qualitative agreement with the experimental results.

The discrepancy between the calculations and experiments may have several origins. First, we note that the calculations did not and cannot take into account plastic deformation that occurs for the case of rubrene on PDMS. So in this case, comparison is only fair at the lowest strains, and here the number of data points is sparse. Second, within the elastic strain regime, the calculations only simulate a static picture, whereas dynamic effects with increasing temperature (e.g., local/non-local electron-phonon couplings) are not considered. Such dynamic effects are expected to be more significant in the case of compressive strain. Indeed, a larger quantitative discrepancy with the experimental results is observed for compressive elastic strain (Figure 6.8b)

The WF trend in the high-tension regime (Figure 6.7 and Figure 6.8a) is ascribed primarily to the effect of plastic deformation based on two experimental observations. One is the sudden steep rise in ΔWF at ~0.05% strain, which is not associated with any noticeable signs of surface roughening or structural instability (e.g., cracks). It is known from the literature that yield strains for organic crystals are typically <0.1%,[226] consistent with our assignment. A similar WF-strain relationship upon yielding has also been reported for metals.[227] The other important observation is the large hysteresis in ΔWF when elastic tensile strain recovers. This non-recoverable ΔWF is also strongly indicative of plastic strain. In compression, however, ΔWF decreases smoothly as a function of strain without any significant transition point or hysteresis, suggesting that the yield point is not reached. The yield strain is therefore higher for compressive strain than tensile strain, which is also in agreement with observations in other materials and could be due to larger friction between slip layers under compression.[227] The association of plastic

deformation with a large non-recoverable ΔWF strongly suggests the existence of a relationship between defects such as dislocations and charge trapping in organic films.

6.7 Conclusion

In summary, by utilizing thermal expansion of the substrate, we have induced controlled and quantifiable tensile and compressive strains in rubrene single crystals. The change of WF as a result of induced strain is measured by SKPM. The WF increases with tensile strain (elastic and plastic) and decreases with compressive strain in the *a-b* plane of rubrene crystals, confirmed qualitatively by DFT calculations. In tension, the WF increase is slight but measurable by SKPM in the elastic regime. The WF increase becomes much more significant upon the onset of plastic deformation, which occurs at a relatively small tensile strain (<0.1%). In compression, the WF decreases smoothly with increasing strain and no apparent cross-over from elastic to plastic behavior is observed within the investigated strain range. We propose that strain-induced WF variations will lead to band-edge fluctuations, which can impact charge transport, and are an important mechanism for the creation of electrostatic disorder (e.g., band-tail states) in organic semiconductors. As organic thin films will typically have residual microstrain, the sensitivity of WF to strain in organic semiconductors has great implications for the fundamental electrical properties of these materials and their performance in devices.

6.8 Experimental

6.8.1   Sample Preparation

Rubrene single crystals were grown by physical vapor transport using ultrapure Ar as carrier gas.[58] Commercially available rubrene (sublimed grade, 99.99%, Sigma Aldrich) was used as received as the source material. The sublimation temperature was ~280 °C. Only thin crystals (<5 μm) with uniform crystalline regions and smooth/clean surfaces were selected for sample preparation. Thicknesses of the crystals were measured by surface profilometry (KLA-Tencor P-16 surface profiler). The average thickness of all crystals used was ~2 μm. Freshly made crystals were laminated onto either PDMS or silicon substrates. Spontaneous adhesion of the crystals to the substrates occurred. In order to electrically ground the sample, vapor deposited gold film with thicknesses around 500 nm was removed from a Si substrate and transferred to cover part of the crystal by tweezers, and silver paint was then used to connect the gold film to the metal SKPM sample puck.

6.8.2   Scanning Kelvin Probe Microscopy

SKPM measurements were performed with a Cypher ES™ Environmental AFM (Asylum Research), which works in a two pass "lift mode". In the first pass of each line of an image, the conductive probe scans the rubrene surface in attractive-regime dynamic mode to generate the topographic data under conventional amplitude-modulation feedback (also known as "AC" or "tapping" mode) while mechanically vibrating the

cantilever near resonance. The attractive-regime dynamic mode was used since it better preserves the probe and thereby allows meaningful CPD comparison among different measurements. To stabilize performance in the attractive regime, the cantilever was driven at a drive frequency slightly larger (~150 Hz) than the fundamental resonant frequency, and the setpoint amplitude was about 90% of the free amplitude (~90 nm). In the second "interleave" pass, the probe was lifted to a constant height above the surface and scanned the topographic trajectory acquired in the first pass. A tip-applied AC bias resonantly excited the cantilever (via a time-varying electrostatic force gradient between tip and sample) while a DC bias was adjusted under feedback so as to *null* the AC excitation by matching (and thus measuring) the CPD point-to-point across the surface.[135] The samples were heated with an integrated heating stage at a heating rate of ~2 °C/min. The samples were held for ~10 min at the target temperature and the CPDs of the same area were measured multiple times. Note that the cantilever vibrational tuning was repeated at each temperature to account for changes in resonant frequency with temperature. The typical probes were from Nanosensors (PPP-EFM-W, Pt/Ir coated, resonant frequency ~75 kHz, spring constant ~2.8 N/m). The lift height during the second pass was 50 nm, which was beyond the range where van der Waals forces come into play. The applied AC voltage in SKPM was 0-+3 V in amplitude. The SKPM images were analyzed using the freeware Gwyddion.

6.8.3   X-Ray Diffraction

In-situ XRD measurements were carried out with a PANalytical X'Pert Pro X-ray diffractometer with a Cu Kα source operated at 45 kV and 40 mA filament current. The samples were slowly heated (~2 °C/min) to target temperatures using a thermal stage connected to an Anton Paar temperature control unit (TCU 150) within the diffractometer. The samples were allowed to stabilize at the target temperature for ~10 min before the diffraction peaks of interest were measured. To more accurately study the weakly diffracting off-axis peaks, 2D reciprocal space maps were measured. Detailed calculations of strain based XRD measurements are shown in Appendix A3.

6.8.4   Density Functional Theory Calculation

The geometric and electronic properties of strained rubrene single crystals were computed at the density functional theory (DFT) level with the VASP code.[228] The PBE functional were used with a plane-wave basis set (300 eV cutoff) and projector augmented wave potentials.[229, 230] The DFT calculations were carried out using on a 2×2×1 *k*-point grid and a Gaussian smearing with 0.10 eV width. The calculations considered the effects due to elastic strain in a static sense (that is, the dynamic motions of the molecules at a given temperature were not explicitly considered), with the unit-cell parameters chosen as those modified by mechanical strain obtained experimentally. For each crystal structure, the molecules within a unit cell were allowed to fully relax while the lattice parameters remained fixed to the experimental values. Next, a periodic slab containing two layers of rubrene molecules was extracted from the 3D structure, with 30

Å of vacuum space placed between each slab (to prevent spurious inter-slab interactions). The molecules were then allowed to further relax within the fixed surface (slab) unit cell. The WF was determined by tracking the evolution of the potential energy of an electron at the vacuum level (E_{vac}) and the valence band maximum (VBM), as a function of the change in the (experimentally observed) lattice parameters due to mechanical strain.

Chapter 7 Future Work

7.1 Resolution Enhancement of In-Liquid Lattice Imaging

As discussed in Chapter 5, although lattice-resolved images of pentacene bi-layers on dielectrics is possible by in-liquid AFM, the significant noise caused by instrument drift and/or the tip/sample contaminations leads to distorted lattice structures obtained from the low friction (LF) region of the pentacene second layer, and loss of lattice resolution from the pentacene first layer and the high friction (HF) domains of the second layer. This hinders the direct determination of the homoepitaxial type. Therefore, it would be helpful to improve the resolution of in-liquid lattice imaging. In this section, two methods are proposed, namely, to explore more liquid options, and to calibrate the lattice images by references.

Explore more liquid options. It is known that the imaging environment is critical for the resolution of the lattice-resolved images.[231] In my previous work, two common liquids, DI water and ethanol, were used for the lattice imaging, as shown in Figure 7.1. The comparison of the two liquids shows that the imaging resolution is very sensitive to the type of liquid used as it largely affects the force curve. Also, there is a trade-off between lattice resolution and the film integrity. As can be seen in the results, imaging in ethanol renders the best lattice resolution and the lattice image (Figure 7.1b) shows much less noise than those obtained in water (Figure 7.1e) and water-ethanol mixture (Figure 7.1h). However, the film is quickly "dissolved" by ethanol as shown in Figure 7.1a. The

water-ethanol mixture seems to be the best in terms of obtaining a balance between the lattice resolution and the film integrity. However, the obtained lattice images are still too noisy to reflect the true structure of the film.
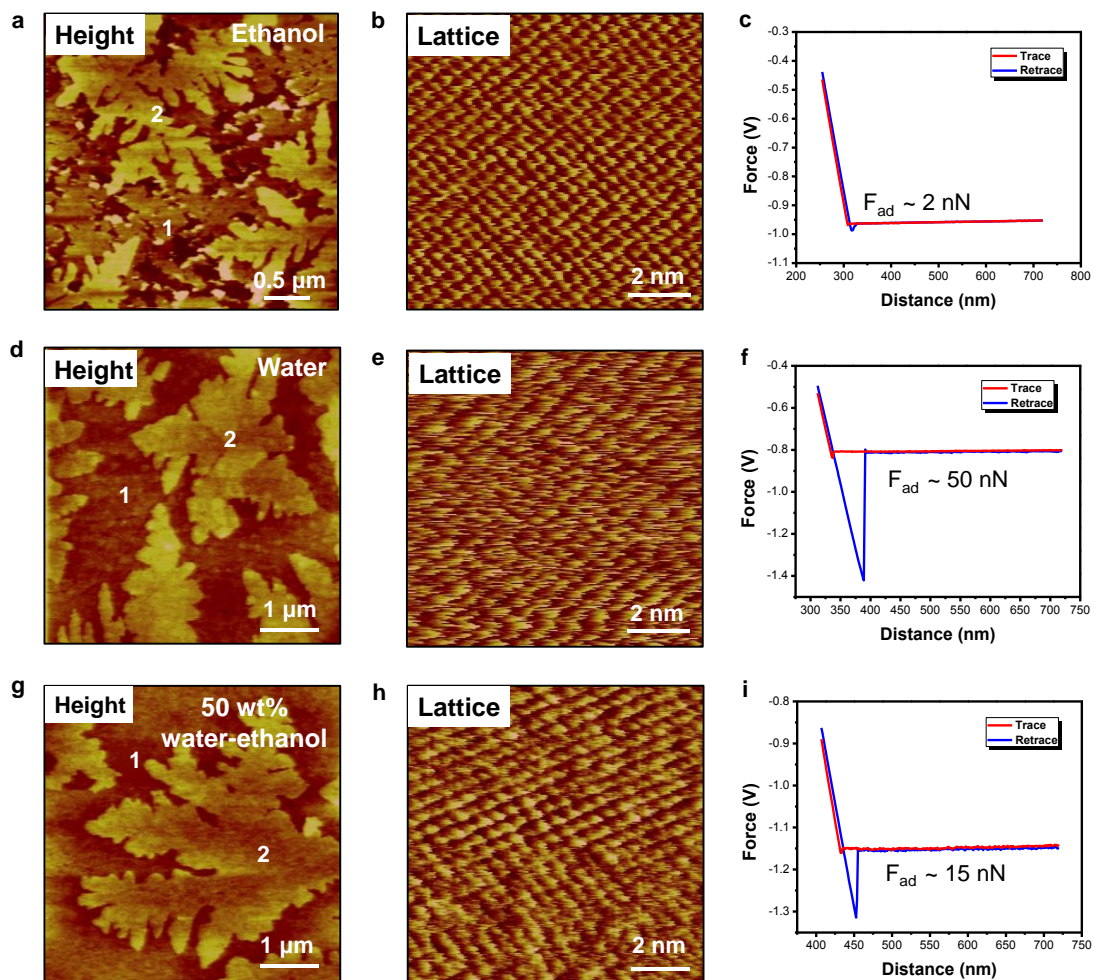
Figure 7.1 Comparison of different liquids for lattice imaging.
There is a trade-off between the film integrity and the lattice resolution. In ethanol (a-c), very small adhesion force gives rise to good lattice resolution. However, the pentacene film, especially the first monolayer, is not stable. In water (d-f), the film is intact but much larger adhesion force makes the lattice resolution much worse. In 50 wt% water-ethanol mixture (g-i), the film morphology can be maintained and the lattice resolution is somewhat acceptable.

Therefore, more liquid options need to be explored to achieve less destructive imaging with minimized attractive force between the tip and the sample. Note that it would be better to use liquids that are polar,[232] less toxic, and less corrosive. Table 7.1 lists several solvents that have been investigated in literature. The van der Waals force relative to the vacuum and the type of interaction between the tip and the sample are given, and are compared with that of water.[232]

Table 7-1 Different liquids for lattice imaging.

Liquid	Van der Waals Force Relative to Vacuum	Type of Interaction
CCl_4	4.4%	Attractive
Glycerol	3.6%	Repulsive
H_2O_2	2.7%	Attractive
Glycol	1.6%	Attractive
Formamide	0.8%	Repulsive
H_2O	22%	Attractive

Calibrate the lattice images by references. As shown in Figure 5.6, distorted lattice structures are obtained from the LF region of the pentacene second layer mainly due to instrument drift. Note that although the thin film phase structure of the pentacene first monolayer is known, the structure of the pentacene second layer has never been explicitly determined. Therefore, if the distortion can be calibrated, the second layer structure of pentacene can be potentially determined by the lattice images. A solution to this problem is to use references with known lattice structures and also easy to image.

In my previous study, freshly cleaved mica was used as the reference. Mica is a subset of the phyllosilicates (sheet silicates). Classification of the phyllosilicates is based on their

octahedral layers, which may be either all filled trioctahedral layers or two-thirds filled dioctahedral layers. These closely related materials all have perfect basal cleavage and are all monoclinic with a tendency towards pseudohexagonal crystals. The outermost mica surface typically exposes a hexagonally arrayed pattern of oxygen atoms, with a periodicity of 0.52 nm as shown in Figure 7.2. The reciprocal lattice structure of mica obtained from in-liquid AFM imaging are shown in Figure 7.3. Unfortunately, the lattice structures obtained from the same area show quite significant drift from each other, and using either of them as a reference is associated with errors. Therefore, more lattice imaging needs to be carried out until reproducible lattice images of the reference are obtained. Also, efforts need to be made to vary the type of liquid and the applied force so that the imaging is better optimized.
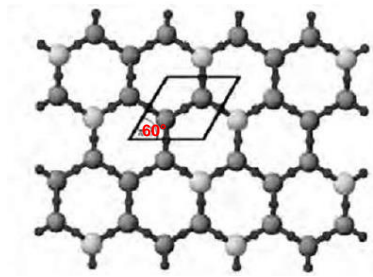
Figure 7.2 Outermost mica surface.
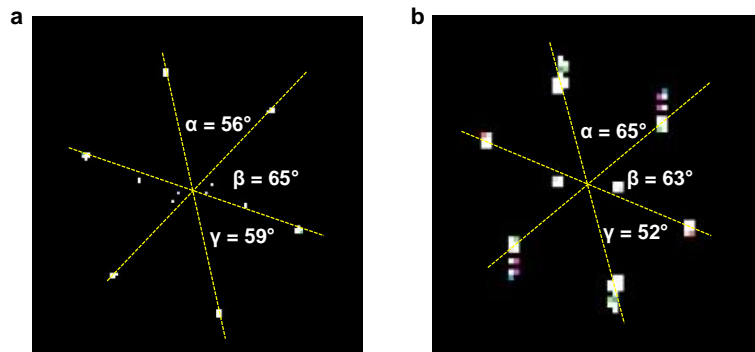
Figure 7.3 Reciprocal lattice structures obtained from the same mica surface by in-liquid AFM.

149

Overall, as can be seen from the above discussion, the two methods are indeed coupled. Optimized liquid, as well as imaging force needs to be determined that works both for the sample and the reference such that the lattice distortion can be calibrated with the known structure of the reference.

7.2 General Correlation between Homoepitaxial Growth Modes and Surface Potential Inhomogeneity

As shown in Chapter 4, SKPM provides the potential method to identify domains with different homoepitaxial growth modes in organic semiconductor bi-layers. Also, Chapter 5 shows that the homoepitaxial growth modes can be conveniently and explicitly determined by a combination of FFM and TSM. Since our previous studies have been mainly focused on pentacene films on different dielectrics, it would be interesting to extend the studies to other common molecular organic semiconductors and to demonstrate that the relationship between homoepitaxial growth modes and surface electrostatic potential is general in other soft, polycrystalline organic bi-layers.

For this study, the organic semiconductors need to be able to form polycrystalline films on common dielectric substrates by thermal evaporation. Also, the film formation needs to be in layer-by-layer or layer-plus-island fashions. In my previous research, several organic molecules were investigated as listed in Figure 7.4.

a

Dinaphtho[2,3-b:2′,3′-f]thieno[3,2-b]thiophene
(DNTT; P-type)

b

N,N′-Dioctyl-3,4,9,10-perylenedicarboximide
(PTCDI-C8; N-type)

c

Para-sexiphenyl
(6P; P-type)
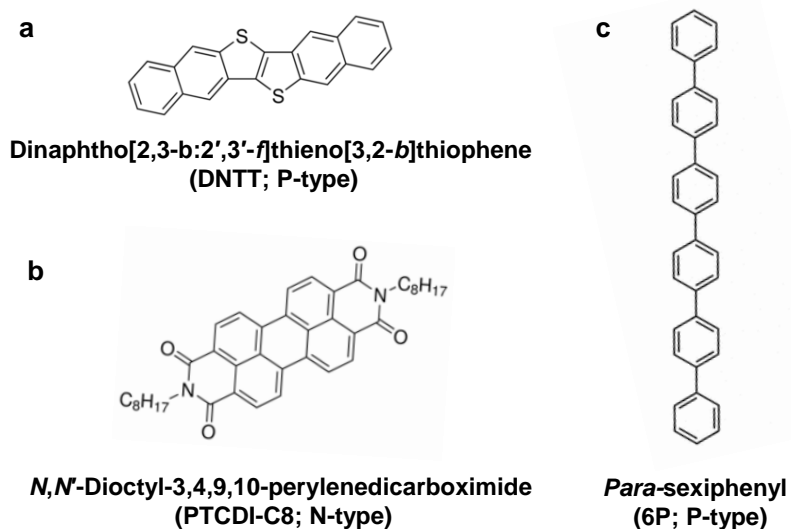
Figure 7.4 Molecular structures of candidate organic semiconductors.

The above molecules were found to exhibit similar growth behavior as pentacene when thermally deposited on common dielectric substrates, such as PMMA and SiO_2. The AFM topography images of the sub-monolayer and multi-layer films are shown in Figure 7.5. The morphologies of DNTT and 6P bi-layers are very similar to pentacene bi-layers, i.e., dendritic second layer grains growing on top of almost closed first layer. The multi-layer films of PTCDI-C8, however, show very different morphology. The second and the third layer grains seems to exhibit some preferential elongation along certain orientations.

Therefore, the next step is to carry out SKPM and FFM/TSM imaging on these films. It is reasonable to expect mixed homoepitaxial types, i.e., epitaxy and non-epitaxy, in all these films due to their polycrystalline nature. The different strain states and/or defect densities associated with the epitaxial and non-epitaxial domains will lead to lateral variations of the surface electrostatic potential. It would be interesting to identify the

different domains, to quantify the occurrence of different homoepitaxial types, and to measure the surface potential differences in different organic thin films.
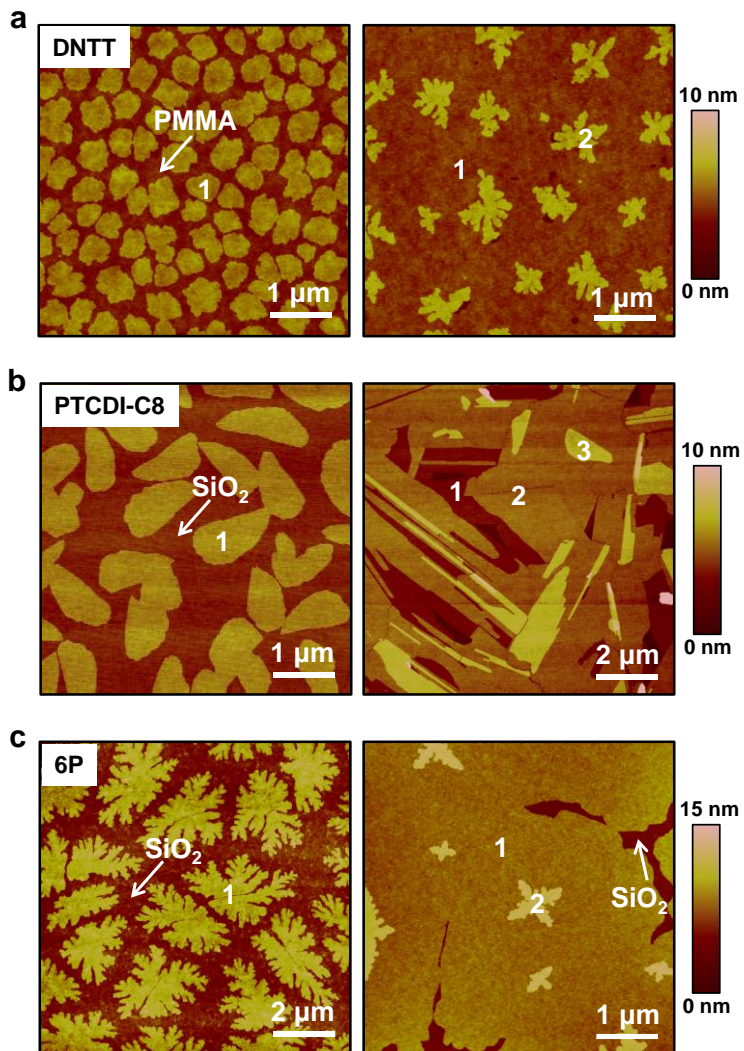
Figure 7.5 Topography of sub-monolayer and multi-layer films of DNTT, PTCDI-C8, and 6P on dielectrics.
(a-b) DNTT sub-monolayer and bi-layer films deposited on PMMA. The morphology is very similar to pentacene films on PMMA. (c-d) PTCDI-C8 sub-monolayer and multi-layer films deposited on SiO_2. The second and the third layer grains exhibit some preferential elongation along certain directions. (d-e) 6P sub-monolayer and multi-layer films deposited on SiO_2.

Bibliography

1. Cahen, D. & Hodes, G. Molecules and electronic materials. *Adv. Mater.* **14**, 789-798 (2002).

2. Horowitz, G. Organic thin film transistors: From theory to real devices. *J. Mater. Res.* **19**, 1946-1962 (2004).

3. Drury, C., Mutsaers, C., Hart, C., Matters, M. & de Leeuw, D. Low-cost all-polymer integrated circuits. *Appl. Phys. Lett.* **73**, 108-110 (1998).

4. Forrest, S. The path to ubiquitous and low-cost organic electronic appliances on plastic. *Nature* **428**, 911-918 (2004).

5. Baude, P. *et al*. Pentacene-based radio-frequency identification circuitry. *Appl. Phys. Lett.* **82**, 3964-3966 (2003).

6. Granstrom, M. *et al*. Laminated fabrication of polymeric photovoltaic diodes. *Nature* **395**, 257-260 (1998).

7. Klauk, H., Gundlach, D., Nichols, J. & Jackson, T. Pentacene organic thin-film transistors for circuit and display applications. *I.E.E.E. transactions on electron devices* **46**, 1258-1263 (1999).

8. Kelley, T. W. *et al*. Recent Progress in Organic Electronics: Materials, Devices, and Processes. *Chem. Mater.* **16**, 4413-4422 (2004).

9. Hung, L. S. & Chen, C. H. Recent progress of molecular organic electroluminescent materials and devices. *Mater. Sci. & Eng.* **39**, 143-222 (2002).

10. So, F., Kido, J. & Burrows, P. Organic Light-Emitting Devices for Solid-State Lighting. *MRS Bull. (previously 'Materials Research Society Newsletter')* **33**, 663-669 (2008).

11. Baeg, K., Noh, Y., Sirringhaus, H. & Kim, D. Controllable Shifts in Threshold Voltage of Top-Gate Polymer Field-Effect Transistors for Applications in Organic Nano Floating Gate Memory. *Adv. Func. Mater.* **20**, 224-230 (2010).

12. Li, J. *et al*. A stable solution-processed polymer semiconductor with record high-mobility for printed transistors. *Sci. Rep.* **2**, 754-754 (2012).

13. Sekitani, T., Noguchi, Y., Zschieschang, U., Klauk, H. & Someya, T. Organic transistors manufactured using inkjet technology with subfemtoliter accuracy. *Proc. Natl. Acad. Sci. U.S.A.* **105**, 4976-4980 (2008).

14. Sokolov, A. N., Roberts, M. E. & Bao, Z. Fabrication of low-cost electronic biosensors. *Materials today* **12**, 12-20 (2009).

15. Someya, T. *et al*. Conformable, flexible, large-area networks of pressure and thermal sensors with organic transistor active matrixes. *Proc. Natl. Acad. Sci. U.S.A.* **102**, 12321-12325 (2005).

16. Someya, T. *et al*. A large-area, flexible pressure sensor matrix with organic field-effect transistors for artificial skin applications. *Proc. Natl. Acad. Sci. U.S.A.* **101**, 9966-9970 (2004).

17. Subramanian, V., Chang, P. C., Lee, J. B., Molesa, S. E. & Volkman, S. K. Printed organic transistors for ultra-low-cost RFID applications. *IEEE transactions on components and packaging technologies* **28**, 742-747 (2005).

18. Yan, H. *et al*. A high-mobility electron-transporting polymer for printed transistors. *Nature* **457**, 679-686 (2009).

19. Katz, H. Recent advances in semiconductor performance and printing processes for organic transistor-based electronics. *Chem. Mater.* **16**, 4748-4756 (2004).

20. Sze, S. M. *Physics of Semiconductor Devices* (1981).

21. Ellison, D., Kim, J. Y., Stevens, D. & Frisbie, C. D. Determination of quasi-Fermi levels across illuminated organic donor/acceptor heterojunctions by Kelvin probe force microscopy. *J. Am. Chem. Soc.* **133**, 13802-13805 (2011).

22. Ellison, D., Lee, B., Podzorov, V. & Frisbie, C. D. Surface Potential Mapping of SAM-Functionalized Organic Semiconductors by Kelvin Probe Force Microscopy. *Adv. Mater.* **23**, 502 (2010).

23. Burgi, L., Sirringhaus, H. & Friend, R. H. Noncontact potentiometry of polymer field-effect transistors. *Appl. Phys. Lett.* **80**, 2913-2915 (2002).

24. Burgi, L., Richards, T., Chiesa, M., Friend, R. & Sirringhaus, H. A microscopic view of charge transport in polymer transistors. *Synth. Met.* **146**, 297-309 (2004).

25. de Wolf, P. *et al*. Status and review of two-dimensional carrier and dopant profiling using scanning probe microscopy. *J. Vac. Sci. Techno. B* **18**, 361-368 (2000).

26. Silveira, W. & Marohn, J. Microscopic view of charge injection in an organic semiconductor. *Phys. Rev. Lett.* **93**, 116104 (2004).

27. Duhm, S., Heimel, G., Salzmann, I., Glowatzki, H., Johnson, R., Vollmer, A., Rabe, J. & Koch, N. Orientation-dependent ionization energies and interface dipoles in ordered molecular assemblies. *Nat. Mater.* **7**, 326-32 (2008).

28. Koch, N., Salzmann, I., Johnson, R. L., Pflaum, J. & Friedlein, R. Molecular orientation dependent energy levels at interfaces with pentacene and pentacenequinone. *Org. Electro.* **7**, 537-545 (2006).

29. Zhu, X. & Kahn, A. Electronic Structure and Dynamics at Organic Donor/Acceptor Interfaces. *MRS Bull.* **35**, 443-448 (2010).

30. Dong, H., Wang, C. & Hu, W. High performance organic semiconductors for field-effect transistors. *Chem. Comm.* **46**, 5211-5222 (2010).

31. Wang, C. *et al*. Dibenzothiophene Derivatives: From Herringbone to Lamellar Packing Motif. *Cryst. Growth & Design* **10**, 4155-4160 (2010).

32. Würthner, F. & Schmidt, R. Electronic and crystal engineering of acenes for solution-processible self-assembling organic semiconductors. *Chem. Phys. Chem.* **7**, 793-797 (2006).

33. Podzorov, V. *et al*. Intrinsic Charge Transport on the Surface of Organic Semiconductors. *Phys. Rev. Lett.* **93**, 086602 (2004).

34. Ma, H., Yip, H., Huang, F. & Jen, A. K. Interface Engineering for Organic Electronics. *Adv. Func. Mater.* **20**, 1371-1388 (2010).

35. Murphy, A. R. & Fréchet, J. M. J. Organic semiconducting oligomers for use in thin film transistors. *Chem. Rev.* **107**, 1066-1096 (2007).

36. Knipp, D., Volkel, A. R., Street, R. A. & Volkel, A. R. Morphology and electronic transport of polycrystalline pentacene thin-film transistors. *Appl. Phys. Lett.* **82**, 3907-3909 (2003).

37. Ruiz, R., Papadimitratos, A., Mayer, A. & Malliaras, G. Thickness dependence of mobility in pentacene thin-film transistors. *Adv. Mater.* **17**, 1795 (2005).

38. Dinelli, F. *et al*. Spatially correlated charge transport in organic thin film transistors. *Phys. Rev. Lett.* **92**, 116802-116802 (2004).

39. Muck, T. *et al*. In situ electrical characterization of DH4T field-effect transistors. *Synth. Met.* **146**, 317-320 (2004).

40. Ohring, M. *Materials Science of Thin Films* (Academic Press, Burlington, 2002).

41. Campbell, S. *Fabrication engineering at the micro and nanoscale*.

42. Venables, J., Spiller, G. & Hanbucken, M. Nucleation and growth of thin films. *Rep. Prog. Phys.* **47**, 399-459 (1984).

43. Mattheus, C. C., Baas, J., Meetsma, A., Dros, A. B., de Boer, J. L. & Palstra, T. T. Polymorphism in pentacene. *Acta Cryst. C, Cryst. Struct. Comm.* **57**, 939-41 (2001).

44. Campbell, R. B., Robertson, J. M. & Trotter, J. The crystal and molecular structure of pentacene. *Acta Cryst. C, Cryst. Struct. Comm.* **14**, 705-711 (1961).

45. Ruiz, R. *et al*. Structure of pentacene thin films. *Appl. Phys. Lett.* **85**, 4926-4928 (2004).

46. Yoshida, H., & Sato, N. Crystallographic and electronic structures of three different polymorphs of pentacene. *Phys. Rev. B* **77**, 235205 (2008).

47. Bouchoms, I., Schoonveld, W., Vrijmoeth, J. & Klapwijk, T. Morphology identification of the thin film phases of vacuum evaporated pentacene on SIO2 substrates. *Synth. Met.* **104**, 175-178 (1999).

48. Ruiz, R. *et al*. Pentacene thin film growth. *Chem. Mater.* **16**, 4497-4508 (2004).

49. Kim, C., Facchetti, A. & Marks, T. Gate dielectric microstructural control of pentacene film growth mode and field-effect transistor performance. *Adv. Mater.* **19**, 2561 (2007).

50. Käfer, D., Ruppel, L. & Witte, G. Growth of pentacene on clean and modified gold surfaces. *Phys. Rev. B* **75**, 085309 (2007).

51. Simeoni, M., Picozzi, S. & Delley, B. An ab-initio study of pentacene on aluminum (100) surface. *Surf. Sci.* **562**, 43-52 (2004).

52. Fritz, S., Martin, S., Frisbie, C. D., Ward, M. & Toney, M. Structural characterization of a pentacene monolayer on an amorphous SiO_2 substrate with grazing incidence X-ray diffraction. *J. Am. Chem. Soc.* **126**, 4084-4085 (2004).

53. Dachs, J. & Bayona, J. Langmuir-derived model for diffusion- and reaction-limited adsorption of organic compounds on fractal aggregates. *Environ. Sci. Techno.* **31**, 2754-2760 (1997).

54. de Boer, R. W. I., Gershenson, M. E., Morpurgo, A. F. & Podzorov, V. Organic single-crystal field-effect transistors. *Phys. Status Solidi.* **201**, 1302-1331 (2004).

55. Lezama, I. G. & Morpurgo, A. F. Progress in organic single-crystal field-effect transistors. *MRS Bull.* **38**, 51-56 (2013).

56. Reese, C. & Bao, Z. Organic single-crystal field-effect transistors. *Materials today* **10**, 20-27 (2007).

57. Jiang, H. & Kloc, C. Single-crystal growth of organic semiconductors. *MRS Bull.* **38**, 28-33 (2013).

58. Laudise, R. A., Kloc, C., Simpkins, P. G. & Siegrist, T. Physical vapor growth of organic semiconductors. *J. Cryst. Growth* **187**, 449-454 (1998).

59. Henn, D. E., Williams, W. G. & Gibbons, D. J. Crystallographic data for an orthorhombic form of rubrene. *J. Appl. Cryst.* **4**, 256 (1971).

60. da Silva Filho, D. A., Kim, E. G. & Bredas, J. L. Transport Properties in the Rubrene Crystal: Electronic Coupling and Vibrational Reorganization Energy. *Adv. Mater.* **17**, 1072-1076 (2005).

61. Binnig, G., Quate, C. F. & Gerber, C. Atomic Force Microscope. *Phys. Rev. Lett.* **56**, 930-933 (1986).

62. Binnig, G. & Rohrer, H. Scanning tunneling microscopy. *Helvetica Phys. Acta.* **55**, 726-735 (1982).

63. Barth, C., Foster, A. S., Henry, C. R. & Shluger, A. L. Recent trends in surface characterization and chemistry with high-resolution scanning force methods. *Adv. Mater.* **23**, 477-501 (2011).

64. Loos, J. The Art of SPM: Scanning Probe Microscopy in Materials Science. *Adv. Mater.* **17**, 1821-1833 (2005).

65. Salapaka, S. & Salapaka, M. Scanning Probe Microscopy. *IEEE control systems magazine*. **28**, 65-83 (2008).

66. Poggi, M. A. *et al*. Scanning probe microscopy. *Anal. Chem.* **76**, 3429-3443 (2004).

67. Karoutsos, V. Scanning probe microscopy: instrumentation and applications on thin films and magnetic multilayers. *J. Nanosci. Nanotechno.* **9**, 6783-6798 (2009).

68. Bhushan, B. Springer Handbook of Nanotechnology. *Springer Science & Business Media*, 331-346 (2010).

69. Haugstad, G. Atomic force microscopy: understanding basic modes and advanced applications. *John Wiley & Sons* (2012).

70. Meyer, E. Atomic force microscopy. *Prog. Surf. Sci.* **41**, 3-49 (1992).

71. García, R. & Perez, R. Dynamic atomic force microscopy methods. *Surf. Sci. Rep.* **47**, 197-301 (2002).

72. Carpick, R. & Salmeron, M. Scratching the surface: Fundamental investigations of tribology with atomic force microscopy. *Chem. Rev.* **97**, 1163-1194 (1997).

73. Bennewitz, R. Friction force microscopy. *Materials today* **8**, 42-48 (2005).

74. Socoliuc, A., Bennewitz, R., Gnecco, E. & Meyer, E. Transition from stick-slip to continuous sliding in atomic friction: entering a new regime of ultralow friction. *Phys. Rev. Lett.* **92**, 134301-134301 (2004).

75. Bhushan, B., Israelachvili, J. & Landman, U. Nanotribology: friction, wear and lubrication at the atomic scale. *Nature* **374**, 607-616 (1995).

76. Chen, J., Ratera, I., Murphy, A. & Ogletree, D. F. Friction-anisotropy dependence in organic self-assembled monolayers. *Surf. Sci.* **600**, 4008-4012 (2006).

77. Lio, A., Charych, D. & Salmeron, M. Comparative atomic force microscopy study of the chain length dependence of frictional properties of alkanethiols on gold and alkylsilanes on mica. *J. Phys. Chem. B* **101**, 3800-3805 (1997).

78. Sasaki, D., Carpick, R. & Burns, A. High molecular orientation in mono- and trilayer polydiacetylene films imaged by atomic force microscopy. *J. Colloid Interface Sci.* **229**, 490-496 (2000).

79. Haugstad, G., Gladfelter, W. L., Weberg, E. B., Weberg, R. T. & Jones, R. R. Probing molecular relaxation on polymer surfaces with friction force microscopy. *Langmuir* **11**, 3473-3482 (1995).

80. Leggett, G. J., Brewer, N. J. & Chong, K. S. L. Friction force microscopy: towards quantitative analysis of molecular organisation with nanometre spatial resolution. *Phys. Chem. Chem. Phys.* **7**, 1107-1120 (2005).

81. Brewer, N., Beake, B. & Leggett, G. Friction force microscopy of self-assembled monolayers: Influence of adsorbate alkyl chain length, terminal group chemistry, and scan velocity. *Langmuir* **17**, 1970-1974 (2001).

82. Xiao, X., Hu, J., Charych, D. & Salmeron, M. Chain length dependence of the frictional properties of alkylsilane molecules self-assembled on Mica studied by atomic force microscopy. *Langmuir* **12**, 235-237 (1996).

83. Last, Julie Hillier, Andrew Hooks, Daniel Maxson,Jeffrey Ward, Michael. Epitaxially Driven Assembly of Crystalline Molecular Films on Ordered Substrates. *Chem. Mater.* **10**, 422-437 (1998).

84. Puntambekar, K., Dong, J., Haugstad, G. & Frisbie, C. D. Structural and electrostatic complexity at a pentacene/insulator interface. *Adv. Func. Mater.* **16**, 879-884 (2006).

85. Kalihari, V., Tadmor, E., Haugstad, G. & Frisbie, C. D. Grain Orientation Mapping of Polycrystalline Organic Semiconductor Films by Transverse Shear Microscopy. *Adv. Mater.* **20**, 4033 (2008).

86. Kalihari, V., Haugstad, G. & Frisbie, C. D. Distinguishing Elastic Shear Deformation from Friction on the Surfaces of Molecular Crystals. *Phys. Rev. Lett.* **104**, 086102 (2010).

87. Burgi, L., Richards, T., Friend, R. & Sirringhaus, H. Close look at charge carrier injection in polymer field-effect transistors. *J. Appl. Phys.* **94**, 6129-6137 (2003).

88. Coffey, D. & Ginger, D. Time-resolved electrostatic force microscopy of polymer solar cells. *Nat. Mater.* **5**, 735-740 (2006).

89. Douheret, O. *et al*. High resolution electrical characterisation of organic photovoltaic blends. *Microelectronic Eng.* **84**, 431-436 (2007).

90. Fujihira, M. Kelvin probe force microscopy of molecular surfaces. *Annu. Rev. Mater. Sci.* **29**, 353-380 (1999).

91. Hoppe, H. *et al*. Kelvin probe force microscopy study on conjugated polymer/fullerene bulk heterojunction organic solar cells. *Nano Lett.* **5**, 269-74 (2005).

92. Melitz, W., Shen, J., Kummel, A. & Lee, S. Kelvin probe force microscopy and its application. *Surf. Sci. Rep.* **66**, 1-27 (2011).

93. Mathijssen, S. *et al*. Scanning Kelvin probe microscopy on organic field-effect transistors during gate bias stress. *Appl. Phys. Lett.* **90**, 192104 (2007).

94. Muller, E. & Marohn, J. Microscopic evidence for spatially inhomogeneous charge trapping in pentacene. *Adv. Mater.* **17**, 1410 (2005).

95. Seshadri, K., & Frisbie, C. D. Potentiometry of an operating organic semiconductor field-effect transistor. *Appl. Phys. Lett.* **78**, 993-995 (2001).

96. Puntambekar, K., Pesavento, P., Frisbie, C. D. Surface potential profiling and contact resistance measurements on operating pentacene thin-film transistors by Kelvin probe force microscopy. *Appl. Phys. Lett.* **83**, 5539-5541 (2003).

97. Nonnenmacher, M., Oboyle, M. & Wickramasinghe, H. Kelvin probe force microscopy. *Appl. Phys. Lett.* **58**, 2921-2923 (1991).

98. Weaver, J. & Abraham, D. High-resolution atomic force microscopy potentiometry. *J. Vac. Sci. Techno. B,* **9**, 1559-1561 (1991).

99. Liess, H.-D., Maeckel, R. & Ren, J. The scanning Kelvin microscope with voltage modulation: a new principle to image discrete surface potentials. *Surf. Interf. Anal.* **25**, 855 (1997).

100. Kelvin, L. Contact electricity of metals. *Philos. Mag. 5* **46**, 82-120 (1898).

101. Zisman, W. A. A new method of measuring contact potential differences in metals. *Rev. Sci. Instru.* **3**, 367-370 (1932).

102. Colchero, J., Gil, A. & Baro, A. Resolution enhancement and improved data interpretation in electrostatic force microscopy. *Phys. Rev. B,* **64**, 245403 (2001).

103. Jacobs, H., Leuchtmann, P., Homan, O. & Stemmer, A. Resolution and contrast in Kelvin probe force microscopy. *J. Appl. Phys.* **84**, 1168-1173 (1998).

104. Colchero, J. *et al*. Electrostatic force gradient signal: resolution enhancement in electrostatic force microscopy and improved Kelvin probe microscopy. *Nanotechnology* **14**, 332-340 (2003).

105. Jacobs, H. O., Knapp, H. F. & Stemmer, A. Practical aspects of Kelvin probe force microscopy. *Rev. Sci. Instru.* **70**, 1756-1760 (1999).

106. Sugimura, H., Ishida, Y., Hayashi, K., Takai, O. & Nakagiri, N. Potential shielding by the surface water layer in Kelvin probe force microscopy. *Appl. Phys. Lett.* **80**, 1459-1461 (2002).

107. Braun, S., Salaneck, W. & Fahlman, M. Energy-Level Alignment at Organic/Metal and Organic/Organic Interfaces. *Adv. Mater.* **21**, 1450-1472 (2009).

108. Cahen, D. & Kahn, A. Electron energetics at surfaces and interfaces: Concepts and experiments. *Adv. Mater.* **15**, 271-277 (2003).

109. Fukagawa, H., Yamane, H., Kera, S., Okudaira, K. & Ueno, N. Experimental estimation of the electric dipole moment and polarizability of titanyl phthalocyanine using ultraviolet photoelectron spectroscopy. *Phys. Rev. B,* **73** (2006).

110. Gao, Y. Surface analytical studies of interfaces in organic semiconductor devices. *Mater. Sci. & Eng. R,* **68**, 39-87 (2010).

111. Ishii, H., Sugiyama, K., Ito, E. & Seki, K. Energy level alignment and interfacial electronic structures at organic metal and organic organic interfaces. *Adv. Mater.* **11**, 605 (1999).

112. Hwang, J., Wan, A. & Kahn, A. Energetics of metal–organic interfaces: New experiments and assessment of the field. *Mater. Sci. & Eng. R,* **64**, 1-31 (2009).

113. Schlaf, R., Parkinson, B. A., Lee, P. A., Nebesny, K. W. & Armstrong, N. R. Determination of frontier orbital alignment and band bending at an organic

semiconductor heterointerface by combined x-ray and ultraviolet photoemission measurements. *Appl. Phys. Lett.* **73**, 1026-1028 (1998).

114. Koch, N. Electronic structure of interfaces with conjugated organic materials. *Phys. Status Solidi. R.* **6**, 277-293 (2012).

115. Crispin, X., Geskin, V., Crispin, A., Cornil, J., Lazzaroni, R., Salaneck, W. & Brédas, J.-L. Characterization of the interface dipole at organic/metal interfaces. *J. Am. Chem. Soc.* **124**, 8131-41 (2002).

116. Monti, O. L. A. & Steele, M. Influence of electrostatic fields on molecular electronic structure: insights for interfacial charge transfer. *Phys. Chem. Chem. Phys.* **12**, 12390-400 (2010).

117. Sakurai, T., Kuroda, R., Akimoto, K. & Wang, S. Energy band bending induced charge accumulation at fullerene/bathocuproine heterojunction interface. *Appl. Phys. Lett.* **100**, 243301 (2012).

118. Brabec, C. J., Sariciftci, N. S. & Hummelen, J. C. Plastic Solar Cells. *Adv. Func. Mater.* **11**, 15-26 (2001).

119. Wilke, A., Endres, J., Hoermann, U., Niederhausen, J. et al. Correlation between interface energetics and open circuit voltage in organic photovoltaic cells. *Appl. Phys. Lett.* **101**, 233301 (2012).

120. Logdlund, M., Salaneck, W. R. & Lögdlund, M. Conjugated polymer surfaces and interfaces in polymer-based light-emitting diodes. *Polym. Adv. Technol.* **9**, 419-428 (1998).

121. Parthasarathy, G., Adachi, C., Burrows, P. E. & Forrest, S. R. High-efficiency transparent organic light-emitting devices. *Appl. Phys. Lett.* **76**, 2128-2130 (2000).

122. Dimitrakopoulos, C. D. & Malenfant, P. Organic Thin Film Transistors for Large Area Electronics. *Adv. Mater.* **14**, 99-117 (2002).

123. Chabinyc, M., Lujan, R., Endicott, F., Toney, M., McCulloch, I. & Heeney, M. Effects of the surface roughness of plastic-compatible inorganic dielectrics on polymeric thin film transistors. *Appl. Phys. Lett.* **90**, 233508 (2007).

124. Zhang, H., Guo, X., Hui, J., Hu, S., Xu, W. & Zhu, D. Interface engineering of semiconductor/dielectric heterojunctions toward functional organic thin-film transistors. *Nano Lett.* **11**, 4939-46 (2011).

125. Yang, S. Y., Shin, K. & Park, C. E. The effect of gate-dielectric surface energy on pentacene morphology and organic field-effect transistor characteristics. *Adv. Func. Mater.* **15**, 1806-1814 (2005).

126. Veres, J., Ogier, S., Lloyd, G. & de Leeuw, D. Gate insulators in organic field-effect transistors. *Chem. Mater.* **16**, 4543-4555 (2004).

127. Salleo, A., Chabinyc, M. L., Yang, M. S. & Street, R. A. Polymer thin-film transistors with chemically modified dielectric interfaces. *Appl. Phys. Lett.* **81**, 4383-4385 (2002).

128. Koch, N. Organic electronic devices and their functional interfaces. *Chem. Phys. Chem.* **8**, 1438-1455 (2007).

129. Chen, L., Ludeke, R., Cui, X., Schrott, A., Kagan, C. & Brus, L. Electrostatic field and partial Fermi level pinning at the pentacene-SiO$_2$ interface. *J. Phys. Chem. B* **109**, 1834-8 (2005).

130. Chiesa, M., Bürgi, L., Kim, J. S., Shikler, R., Friend, R. H. & Sirringhaus, H. Correlation between surface photovoltage and blend morphology in polyfluorene-based photodiodes. *Nano Lett.* **5**, 559-563 (2005).

131. Ikeda, S., Shimada, T., Kiguchi, M. & Saiki, K. Visualization of induced charge in an organic thin-film transistor by cross-sectional potential mapping. *J. Appl. Phys.* **101**, 094509 (2007).

132. Luo, Y., Gustavo, F., et al. Probing Local Electronic Transport at the Organic Single-Crystal/Dielectric Interface. *Adv. Mater.* **19**, 2267-2273 (2007).

133. Jaquith, M., Muller, E. M. & Marohn, J. A. Time-resolved electric force microscopy of charge trapping in polycrystalline pentacene. *J. Phys. Chem. B* **111**, 7711-7714 (2007).

134. Pingree, L. S. C., Rodovsky, D., Coffey, D., Bartholomew, G. & Ginger, D. Scanning Kelvin probe imaging of the potential profiles in fixed and dynamic planar LECs. *J. Am. Chem. Soc.* **129**, 15903-10 (2007).

135. Palermo, V., Palma, M. & Samorı, P. Films by Kelvin Probe Force Microscopy. *Scanning Probe Microscopies Beyond Imaging: Manipulation of Molecules and Nanostructures* (2006).

136. Rosenwaks, Y., Shikler, R., Glatzel, T. & Sadewasser, S. Kelvin probe force microscopy of semiconductor surface defects. *Phys. Rev. B* **70**, 085320 (2004).

137. Ribic, P., Kalihari, V., Frisbie, C. & Bratina, G. Growth of ultrathin pentacene films on polymeric substrates. *Phys. Rev. B* **80**, 115307 (2009).

138. Krok, F., Sajewicz, K., Konior, J., Goryl, M., Piatkowski, P. & Szymonski, M. Lateral resolution and potential sensitivity in Kelvin probe force microscopy: Towards understanding of the sub-nanometer resolution. *Phys. Rev. B* **77** (2008).

139. Zerweck, U., Loppacher, C., Otto, T., Grafström, S. & Eng, L. M. Accuracy and resolution limits of Kelvin probe force microscopy. *Phys. Rev. B* **71**, 125424 (2005).

140. Tsiper, E. & Soos, Z. Electronic polarization in pentacene crystals and thin films. *Phys. Rev. B* **68** (2003).

141. Bryantsev, V. H., Benjamin. Are C-H groups significant hydrogen bonding sites in anion receptors? Benzene complexes with Cl-, NO3-, and ClO4-. *J. Am. Chem. Soc.* **127**, 8282-3 (2005).

142. Parker, H. & Lombardi, J. R. Dipole Moment of the First Excited $\pi^* \leftarrow \pi$ States of Styrene. *J. Chem. Phys.* **54**, 5095 (1971).

143. Chen, H. B., Chang, T. C., Chiu, Y. S. & Ho, S. Y. Photopolymerization of styrene, p-chlorostyrene, methyl methacrylate, and butyl methacrylate with polymethylphenylsilane as photoinitiator. *J. Poly. Chem. A* **34**, 679-685 (1996).

144. Pratontep, S., Brinkmann, M., Nuesch, F. & Zuppiroli, L. Nucleation and growth of ultrathin pentacene films on silicon dioxide: effect of deposition rate and substrate temperature. *Synth. Met.* **146**, 387-391 (2004).

145. Kajimoto, N., Manaka, T. & Iwamoto, M. Decay process of a large surface potential of Alq_3 films by heating. *J. Appl. Phys.* **100**, 053707 (2006).

146. Sushko, P. V., Shluger, A. L. & Catlow, C. Relative energies of surface and defect states: ab initio calculations for the MgO (001) surface. *Surf. Sci.* **450**, 153-170 (2000).

147. Puntambekar, K., Dong, J., Haugstad, G., Frisbie, C. D. Structural and Electrostatic Complexity at a Pentacene/Insulator Interface. *Adv. Func. Mater.* **16**, 879-884 (2006).

148. Kalihari, V., Ellison, D., Haugstad, G., Frisbie, C. D. Observation of Unusual Homoepitaxy in Ultrathin Pentacene Films and Correlation with Surface Electrostatic Potential. *Adv. Mater.* **21**, 3092-3098 (2009).

149. Hains, A., Liang, Z., Woodhouse, M. & Gregg, B. Molecular Semiconductors in Organic Photovoltaic Cells. *Chem. Rev.* **110**, 6689-6735 (2010).

150. Kulkarni, A., Tonzola, C., Babel, A. & Jenekhe, S. Electron Transport Materials for Organic Light-Emitting Diodes. *Chem. Mater.* **16**, 4556-4573 (2004).

151. Rand, B., Genoe, J., Heremans, P., Poortmans, J. Solar cells utilizing small molecular weight organic semiconductors. *Prog. Photovoltaics* **15**, 659-676 (2007).

152. Shirota, Y. & Kageyama, H. Charge carrier transporting molecular materials and their applications in devices. *Chem. Rev.* **107**, 953-1010 (2007).

153. Klauk, H. Organic thin-film transistors. *Chem. Soc. Rev.* **39**, 2643-66 (2010).

154. Coropceanu, V. *et al*. Charge transport in organic semiconductors. *Chem. Rev.* **107**, 926-952 (2007).

155. Horowitz, G. & Hajlaoui, M. E. Mobility in Polycrystalline Oligothiophene Field-Effect Transistors Dependent on Grain Size. *Adv Mater* **12**, 1046-1050 (2000).

156. Horowitz, G. & Hajlaoui, M. E. Grain size dependent mobility in polycrystalline organic field-effect transistors. *Synth. Met.* **122**, 185-189 (2001).

157. Fiebig, M., Beckmeier, D. & Nickel, B. Thickness-dependent in situ studies of trap states in pentacene thin film transistors. *Appl. Phys. Lett.* **96**, 083304 (2010).

158. Nickel, B. *et al*. Pentacene devices: Molecular structure, charge transport and photo response. *Phys. Status. Solidi.* **205**, 526-533 (2008).

159. Bolognesi, A. *et al*. Effects of grain boundaries, field-dependent mobility, and interface trap states on the electrical characteristics of pentacene TFT. *IEEE Trans. Electron Devices* **51**, 1997 (2004).

160. Yogev, S., Matsubara, R., Nakamura, M. & Rosenwaks, Y. Local charge accumulation and trapping in grain boundaries of pentacene thin film transistors. *Org. Electro.* **11**, 1729-1735 (2010).

161. Verlaak, S., Arkhipov, V. & Heremans, P. Modeling of transport in polycrystalline organic semiconductor films. *Appl. Phys. Lett.* **82**, 745-747 (2003).

162. Verlaak, S. & Heremans, P. Molecular microelectrostatic view on electronic states near pentacene grain boundaries. *Phys. Rev. B* **75**, 115127 (2007).

163. Rivnay, J. *et al*. Large modulation of carrier transport by grain-boundary molecular packing and microstructure in organic thin films. *Nat. Mater.* **8**, 952-958 (2009).

164. Hooks, D., Fritz, T. & Ward, M. Epitaxy and molecular organization on solid substrates. *Adv. Mater.* **13**, 227 (2001).

165. Witte, G. & Woll, C. Growth of aromatic molecules on solid substrates for applications in organic electronics. *J. Mater. Res.* **19**, 1889-1916 (2004).

166. Hillier, A. & Ward, M. Epitaxial interactions between molecular overlayers and ordered substrates. *Phys. Rev. B* **54**, 14037 (1996).

167. Kakudate, T., Yoshimoto, N., Kawamura, K. & Saito, Y. Observation of epitaxial growth of pentacene thin films on KCl substrate by X-ray diffractometry. *J. Cryst. Growth* **306**, 27-32 (2007).

168. Mannsfeld, S. C. B. & Fritz, T. Understanding organic–inorganic heteroepitaxial growth of molecules on crystalline substrates: Experiment and theory. *Phys. Rev. B* **71**, 235405 (2005).

169. Kasemann, D. *et al*. Line-on-line organic-organic heteroepitaxy of quaterrylene on hexa-peri-hexabenzocoronene on Au (111). *Langmuir* **25**, 12569-12573 (2009).

170. Wagner, C., Forker, R. & Fritz, T. On the Origin of the Energy Gain in Epitaxial Growth of Molecular Films. *J. Phys. Chem. Lett.* **3**, 419-424 (2012).

171. Götzen, J., Käfer, D., Wöll, C. & Witte, G., Christof. Growth and structure of pentacene films on graphite: Weak adhesion as a key for epitaxial film growth. *Phys. Rev. B* **81** (2010).

172. Kakudate, T., Yoshimoto, N. & Saito, Y. Polymorphism in pentacene thin films on SiO$_2$ substrate. *Appl. Phys. Lett.* **90**, 081903 (2007).

163

173. Schmitz-Hübsch, T., Fritz, T., Sellam, F., Staub, R. & Leo, K. Epitaxial growth of 3,4,9,10-perylene-tetracarboxylic-dianhydride on Au(111): A STM and RHEED study. *Phys. Rev.* **55**, 7972-7976 (1997).

174. Nishinaga, J., Kawaharazuka, A. & Horikoshi, Y. RHEED intensity oscillation of C60 layer epitaxial growth. *J. Cryst. Growth* **311**, 2227-2231 (2009).

175. Last, J. A. & Ward, M. D. Electrochemical annealing and friction anisotropy of domains in epitaxial molecular films. *Adv. Mater.* **8**, 730-733 (1996).

176. Zhang, J., Rabe, J. & Koch, N. Grain-boundary evolution in a pentacene monolayer. *Adv. Mater.* **20**, 3254 (2008).

177. Klauk, H. *et al*. High-mobility polymer gate dielectric pentacene thin film transistors. *J. Appl. Phys.* **92**, 5259-5263 (2002).

178. McDermott, M., Green, J. & Porter, M. Scanning force microscopic exploration of the lubrication capabilities of n-alkanethiolate monolayers chemisorbed at gold Structural basis of microscopic friction and wear. *Langmuir* **13**, 2504-2510 (1997).

179. Gosvami, N., Egberts, P. & Bennewitz, R. Molecular order and disorder in the frictional response of alkanethiol self-assembled monolayers. *J. Phys. Chem. A* **115**, 6942-7 (2011).

180. Wu, Y., Haugstad, G., Frisbie, C. D. Electronic Polarization at Pentacene/Polymer Dielectric Interfaces: Imaging Surface Potentials and Contact Potential Differences as a Function of Substrate Type, Growth Temperature, and Pentacene Microstructure. *J. Phys. Chem. C* **118**, 2487-2497 (2014).

181. Mannsfeld, S., Virkar, A., Reese, C., Toney, M. & Bao, Z. Precise Structure of Pentacene Monolayers on Amorphous Silicon Oxide and Relation to Charge Transport. *Adv. Mater.* **21**, 2294 (2009).

182. Drake, B. *et al*. Imaging crystals, polymers, and processes in water with the atomic force microscope. *Science* **243**, 1586-1589 (1989).

183. Cai, H., Hillier, A. C., Franklin, K. R., Nunn, C. C. & Ward, M. D. Nanoscale imaging of molecular adsorption. *Science* **266**, 1551-5 (1994).

184. Carter, P., Hillier, A. & Ward, M. Nanoscale surface topography and growth of molecular crystals - the role of anisotropic intermolecular bonding. *J. Am. Chem. Soc.* **116**, 944 (1994).

185. Gan, Y. F., George. High resolution AFM images of the single-crystal alpha-Al2O3(0001) surface in water. *J. Phys. Chem. B* **109**, 12474-9 (2005).

186. Hillier, A. C. & Ward, M. D. Atomic force microscopy of the electrochemical nucleation and growth of molecular crystals. *Science* **263**, 1261-4 (1994).

187. Weisenhorn, A., Hansma, P., Albrecht, T. & Quate, C. Forces in atomic force microscopy in air and water. *Appl. Phys. Lett.* **54**, 2651-2653 (1989).

188. Jang, J., Schatz, G. & Ratner, M. Capillary force in atomic force microscopy. *J. Chem. Phys.* **120**, 1157-1160 (2004).

189. Ohnesorge, F. & Binnig, G. True atomic-resolution by atomic force microscopy through repulsive and attractive forces. *Science* **260**, 1451-1456 (1993).

190. Russell, V. & Ward, M. Molecular crystals with dimensionally controlled hydrogen-bonded nanostructures. *Chem. Mater.* **8**, 1654-1666 (1996).

191. Weisenhorn, A. *et al*. Molecular-resolution images of Langmuir-Blodgett-film and DNA by atomic force microscopy. *Langmuir* **7**, 8-12 (1991).

192. Nelles, G. *et al*. Two-Dimensional Structure of Disulfides and Thiols on Gold(111). *Langmuir* **14**, 808-815 (1998).

193. Fischetti, M. V. & Laux, S. E. Band structure, deformation potentials, and carrier mobility in strained Si, Ge, and SiGe alloys. *J. Appl. Phys.* **80**, 2234-2252 (1996).

194. Ishikawa, Y. *et al*. Strain-induced band gap shrinkage in Ge grown on Si substrate. *Appl. Phys. Lett.* **82**, 2044-2046 (2003).

195. Kuo, C. P., Vong, S. K., Cohen, R. M. & Stringfellow, G. B. Effect of mismatch strain on band gap in III-V semiconductors. *J. Appl. Phys.* **57**, 5428-5432 (1985).

196. Roberts, M. *et al*. Elastically relaxed free-standing strained-silicon nanomembranes. *Nat. Mater.* **5**, 388-393 (2006).

197. Sun, Y., Thompson, S. E. & Nishida, T. Physics of strain effects in semiconductors and metal-oxide-semiconductor field-effect transistors. *J. Appl. Phys.* **101**, 104503 (2007).

198. Lee, M., Fitzgerald, E., Bulsara, M., Currie, M. & Lochtefeld, A. Strained Si, SiGe, and Ge channels for high-mobility metal-oxide-semiconductor field-effect transistors. *J. Appl. Phys.* **97**, 011101 (2005).

199. Welser, J., Hoyt, J. L. & Gibbons, J. F. Electron mobility enhancement in strained-Si n-type metal-oxide-semiconductor field-effect transistors. *IEEE Electron. Device Lett.* **15**, 100-102 (1994).

200. Kido, J., Kimura, M. & Nagai, K. Multilayer White Light-Emitting Organic Electroluminescent Device. *Science* **267**, 1332-1334 (1995).

201. Günes, S., Neugebauer, H. & Sariciftci, N. S. Conjugated polymer-based organic solar cells. *Chem. Rev.* **107**, 1324-1338 (2007).

202. Peumans, P., Uchida, S. & Forrest, S. Efficient bulk heterojunction photovoltaic cells using small-molecular-weight organic thin films. *Nature* **425**, 158-162 (2003).

203. Giri, G. *et al*. Tuning charge transport in solution-sheared organic semiconductors using lattice strain. *Nature* **480**, 504-508 (2011).

204. Briseno, A. *et al*. High-Performance Organic Single-Crystal Transistors on Flexible Substrates. *Adv. Mater.* **18**, 2320-2324 (2006).
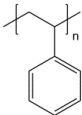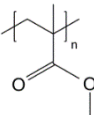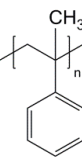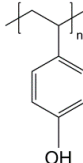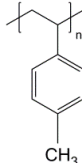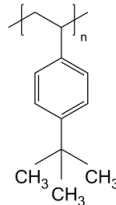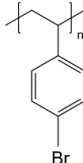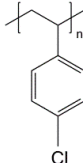
205. Jedaa, A. & Halik, M. Toward strain resistant flexible organic thin film transistors. *Appl. Phys. Lett.* **95**, 103309 (2009).

206. Sekitani, T. *et al*. Bending experiment on pentacene field-effect transistors on plastic films. *Appl. Phys. Lett.* **86**, 073511 (2005).

207. Sokolov, A., Cao, Y., Johnson, O. & Bao, Z. Mechanistic Considerations of Bending-Strain Effects within Organic Semiconductors on Polymer Dielectrics. *Adv. Func. Mater.* **22**, 175-183 (2012).

208. Yang, C., Yoon, J., Kim, S. H., Hong, K., Chung, D. H., Heo, K., Park, C. E. & Ree, M. Bending-stress-driven phase transitions in pentacene thin films for flexible organic field-effect transistors. *Appl. Phys. Lett.* **92**, 243305 (2008).

209. Cour, I. *et al*. Origin of stress and enhanced carrier transport in solution-cast organic semiconductor films. *J. Appl. Phys.* **114**, 093501 (2013).

210. Kowarik, S. *et al*. Real-Time Observation of Structural and Orientational Transitions during Growth of Organic Thin Films. *Phys. Rev. Lett.* **96**, 125504 (2006).

211. Mativetsky, J., Burke, S., Fostner, S. & Grutter, P. Templated growth of 3,4,9,10-perylenetetracarboxylic dianhydride molecules on a nanostructured insulator. *Nanotechnology* **18**, 105303 (2007).

212. Murakami, Y. *et al*. Microstructural Study of the Polymorphic Transformation in Pentacene Thin Films. *Phys. Rev. Lett.* **103**, 146102 (2009).

213. Okada, Y., Sakai, K., Uemura, T., Nakazawa, Y. & Takeya, J. Charge transport and Hall effect in rubrene single-crystal transistors under high pressure. *Phys. Rev. B* **84**, 245308 (2011).

214. Schatschneider, B., Monaco, S., Tkatchenko, A. & Liang, J. Understanding the structure and electronic properties of molecular crystals under pressure: application of dispersion corrected DFT to oligoacenes. *J. Phys. Chem.* **117**, 8323-8331 (2013).

215. Jurchescu, O., Baas, J. & Palstra, T. Effect of impurities on the mobility of single crystal pentacene. *Appl. Phys. Lett.* **84**, 3061-3063 (2004).

216. Haas, S. Crystal structure analysis and trap spectroscopy in organic semiconducting crystals. *PhD Diss. ETH Zürich* **16657**, 28-33 (2006).

217. Bowden, N., Huck, W., Paul, K. E. & Whitesides, G. M. The controlled formation of ordered, sinusoidal structures by plasma oxidation of an elastomeric polymer. *Appl. Phys. Lett.* **75**, 2557-2559 (1999).

218. Okada, Y. & Tokumaru, Y. Precise determination of lattice parameter and thermal expansion coefficient of silicon between 300 and 1500 K. *J. Appl. Phys.* **56**, 314-320 (1984).

219. Palermo, V., Palma, M., Samori, P. Electronic Characterization of Organic Thin Films by Kelvin Probe Force Microscopy. *Adv. Mater.* **18**, 145-164 (2006).

220. Lee, B., Choi, T., Cheong, S. & Podzorov, V. Nanoscale Conducting Channels at the Surface of Organic Semiconductors Formed by Decoration of Molecular Steps with Self-Assembled Molecules. *Adv. Func. Mater.* **19**, 3726-3730 (2009).

221. Reyes-Martinez, M., Ramasubramaniam, A., Briseno, A. & Crosby, A. The Intrinsic Mechanical Properties of Rubrene Single Crystals. *Adv. Mater.* **24**, 5548-5552 (2012).

222. Ibragimov, K. I. & Korol'kov, V. A. Temperature dependence of the work function of metals and binary alloys. *Inorg. Mater.* **37**, 567-572 (2001).

223. Leu, P. W., Svizhenko, A. & Cho, K. Ab initio calculations of the mechanical and electronic properties of strained Si nanowires. *Phys. Rev. B* **77**, 235305 (2008).

224. Unal, K. & Wickramasinghe, H. K. Nanoscale quantitative stress mapping with atomic force microscopy. *Appl. Phys. Lett.* **90**, 113111 (2007).

225. Choi, S., Jhi, S. & Son, Y. Effects of strain on electronic properties of graphene. *Phys. Rev. B* **81**, 081407 (2010).

226. Robinson, P. M. & Scott, H. G. Plastic deformation of anthracene single crystals. *Acta Met.* **15**, 1581-1590 (1967).

227. Li, W. & Li, D. Y. In situ measurements of simultaneous electronic behavior of Cu and Al induced by mechanical deformation. *J. Appl. Phys.* **99**, 073502 (2006).

228. Kresse, G. & Furthmüller, J. Efficiency of ab-initio total energy calculations for metals and semiconductors using a plane-wave basis set. *Comp. Mater. Sci.* **6**, 15-50 (1996).

229. Blöchl, P. E. Projector augmented-wave method. *Phys. Rev.* **50**, 17953-17979 (1994).

230. Kresse, G. & Joubert, D. From ultrasoft pseudopotentials to the projector augmented-wave method. *Phys. Rev.* **59**, 1758-1775 (1999).

231. Liu, Z. H. & Brown, N. M. D. The influence of imaging conditions on the appearance of lattice-resolved AFM images of mica surfaces. *J. Phys.* **30**, 2503-2508 (1997).

232. Hartmann, U. Theory of van der Waals microscopy. *J. Vac. Sci. Techno. B* **9**, 465-469 (1991).

Appendix

A1. Supplementary Information for Chapter 4

Table A1-1 Summary of polymer properties

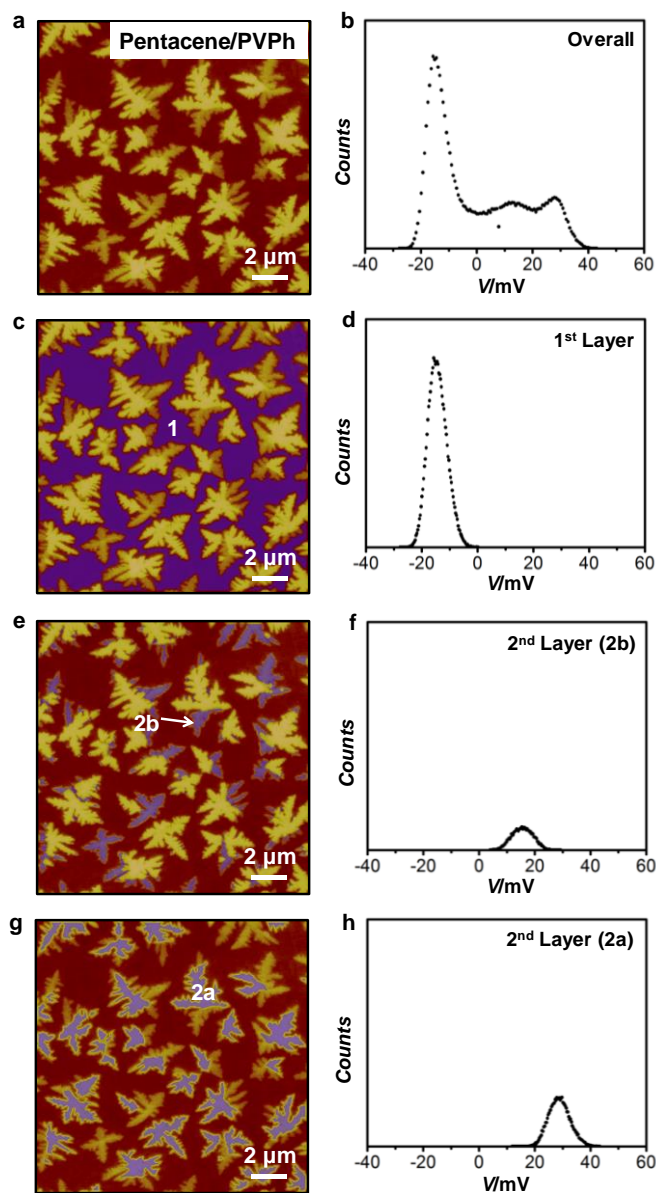| Polymer								
Short Name	PS	PMMA	PαMS	PVPh	PMS	P*t*BS	PBS	PCS
M_w [kg/mol]	350	350	65	35	72	50-100	65	75
T_g [°C]	~100	~125	~180	~170	~108	~137	~118	~110
Water Contact Angle [°]	86±1	72±2	90±1	73±2	97±1	101±1	96±1	92±1

Figure A1.1 An example demonstrating the histogram analyses for individual regions using freeware *Gwyddion*.

(a) Surface potential image of pentacene two-layer film deposited on PVPh. (b) Corresponding histogram for the entire image of (a). (c) The first layer is masked and by shrinking the mask pixiel by pixiel the boundary between the second layer and the first is exposed. (d) Histogram of masked region of (c). (e) The low surface potential region of the second layer (2b) is masked and similarly, the edge is not included to avoid the tip convolution. (f) Histogram of masked region in (e). (g) the high surface potential domain of the second layer (2a) is masked with boundary being excluded. (h) Corresponding histogram of masked region in (g).
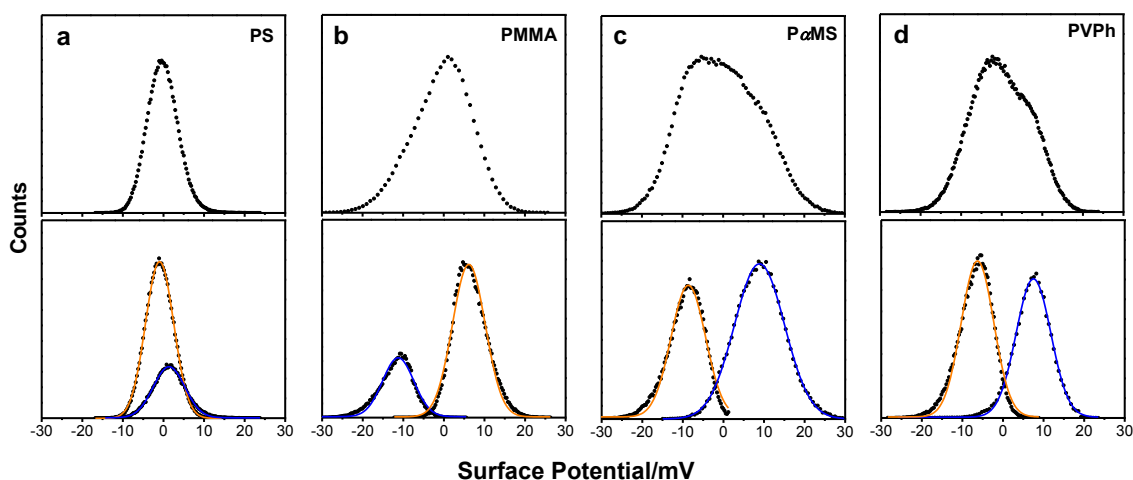
Figure A1.2 Surface potential histograms of pentacene sub-monolayer films grown on different substrates.

Top: surface potential histogram of pentacene sub-monolayers on PS, PMMA, PαMS, and PVPh directly obtained from an entire potential image using *Gwyddion*. A broad distribution is shown in all the four different films. Bottom (from Figure 4.2): Potential histogram of the same image obtained by placing mask on the substrate or pentacene grains, and extracting histograms for masked region only. Two peaks representing the surface potential distribution of the substrate (blue) and pentacene islands (orange), respectively, can be clearly distinguished.

Figure A1.3 Surface potential histograms of sub-monolayer pentacene films grown on different substrates.

Top: surface potential histogram of pentacene sub-monolayers on directly obtained from an entire potential image using *Gwyddion*. A broad distribution is shown only with d) and e) showing two distinguishable peaks. Bottom (from Figure 4.3): Potential histogram of the same image obtained by placing mask on the substrate or pentacene grains, and extracting histograms for masked region only. Two peaks representing the surface potential distribution of the substrate (blue) and pentacene islands (orange), respectively, can be clearly distinguished.
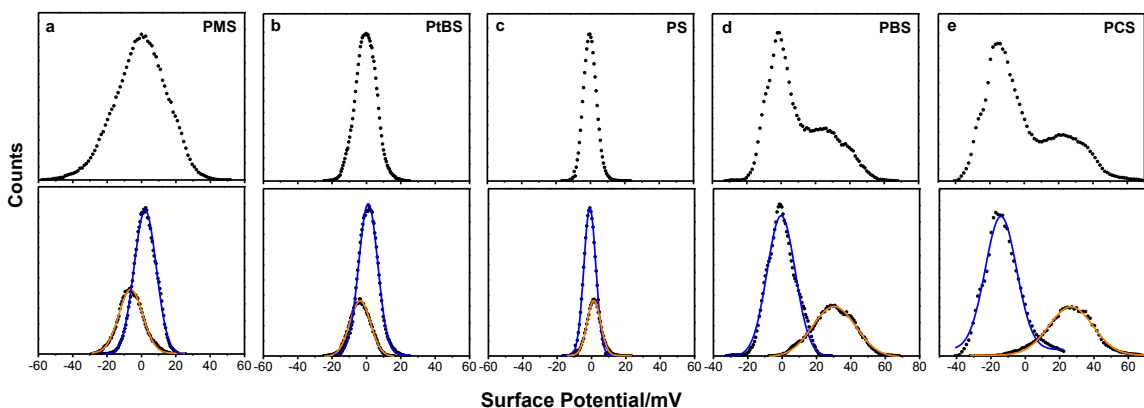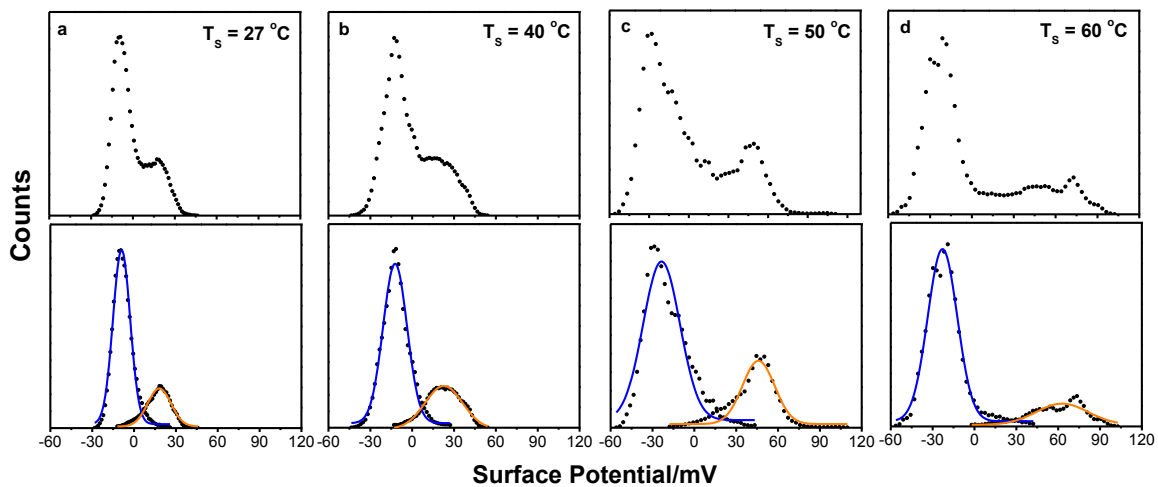
Figure A1.4 Surface potential histograms of pentacene sub-monolayer films grown on PBS at different substrate temperatures.
Top: surface potential histograms of pentacene sub-monolayers grown on PBS at 27 °C, 40 °C , 50 °C, and 60 °C directly obtained by histogram analysis of an entire potential image by *Gwyddion*. Bottom (from Figure 4.6): Potential histogram of the same image obtained by placing mask on the substrate or pentacene grains, and extracting histograms for masked region only. The potential convolution effect is largely eliminated and two clear peaks are shown in the potential histogram, representing the surface potential distribution of the substrate (orange) and pentacene grains (blue), respectively.
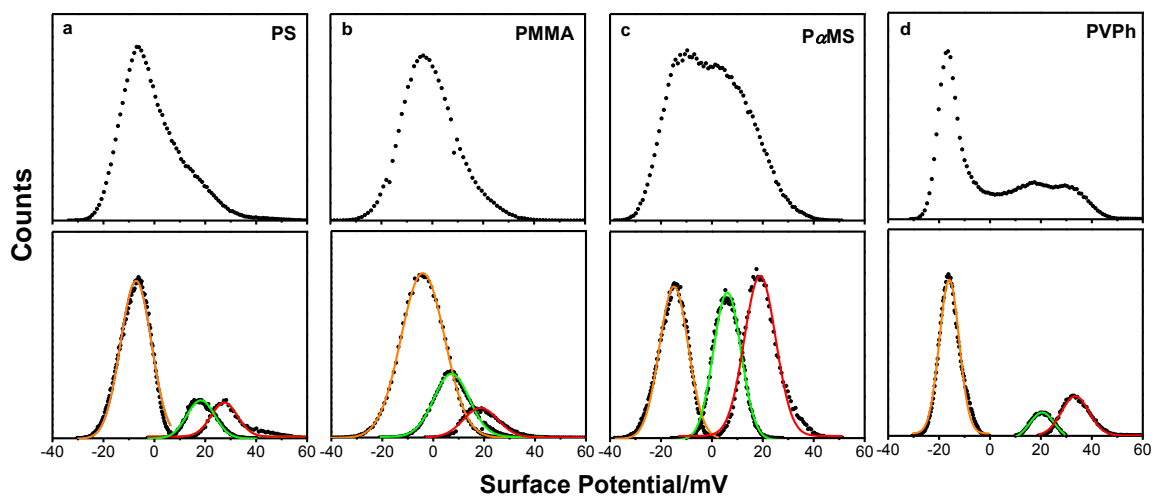
Figure A1.5 Surface potential histograms of pentacene bi-layers grown on different substrates.
Top: surface potential histogram of pentacene bi-layers grown on PS, PMMA, PαMS, and PVPh directly obtained from an entire potential image by *Gwyddion*. A broad distribution is shown in all the four different films only with (d) displaying three peaks. Bottom (from Figure 4.8): Potential histogram of the same image obtained by placing mask on the first layer or the two different domains of the second layer, and extracting histograms for masked region only. Three peaks representing the surface potential distribution of the first layer (orange), 2a domains (red), and 2b domains (green) respectively, can be clearly distinguished.
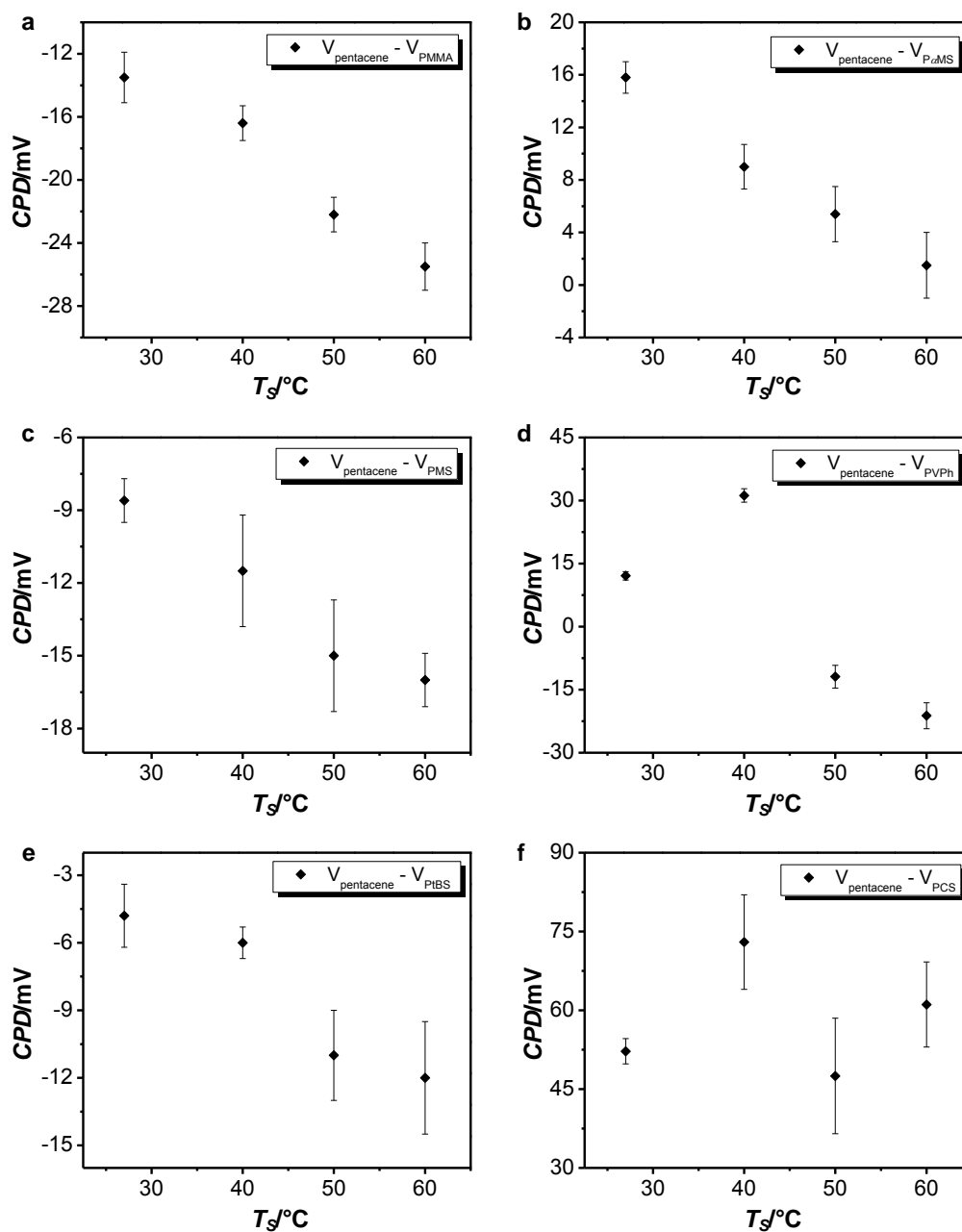
Figure A1.6 Surface potential as a function of substrate temperatures for pentacene sub-monolayers grown at different temperatures.
The plotted CPD is defined as the difference between surface potential of pentacene grains and that of the bare substrates and each CPD was obtained from averaging peak-to-peak separation of histograms of at least two different samples in six measurements. Significant CPD difference can be seen by varying T_S.
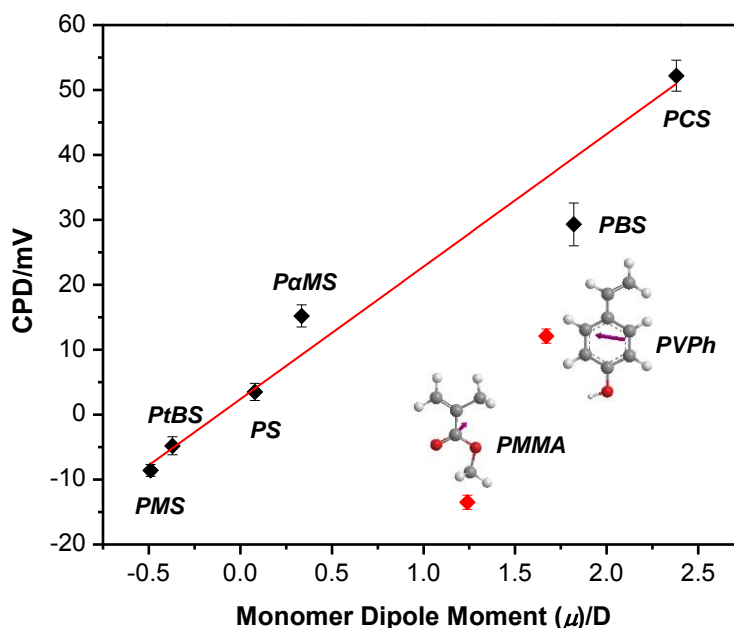
Figure A1.7 Quantitative summary of CPDs as a function of the monomer dipole moment, with all investigated polymers plotted.
All the films were deposited when the substrates were at room temperature. The CPDs were calculated using the surface potential peaks of pentacene and substrate, respectively, from potential histograms of at least two different samples in six measurements. The dipole moments of the monomers were calculated using the software ChemDraw. PMMA and PVPh deviate from the linear CPD/dipole moment relationship as observed in all the other polymers probably due to their smaller hydrophobicity.
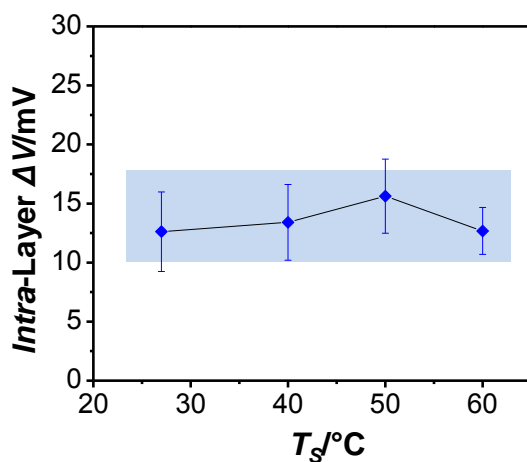
Figure A1.8 Plot of *intra*-layer surface potential difference as a function of substrate temperature. Not a strong dependence is found. (Data were taken from pentacene/PVPh films)

A2. Supplementary Information for Chapter 5
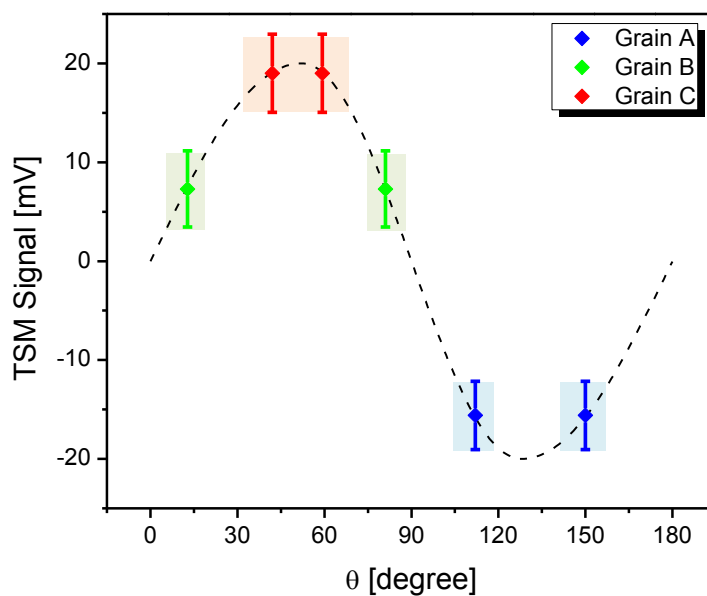
Figure A2.1 Dependence of TSM signal on the grain orientation and detemination of specific grain orientation for grains (Grain A, B, and C) labeled in Figure 5.1.
The TSM signal could indicate two different grain orientations in most circumstances. The instrument noise gives each TSM signal errors comparable to the total signal level. Therefore, with the uncertainty of TSM signals, ranges of grain orientations are determined instead of explicit grain orientations.
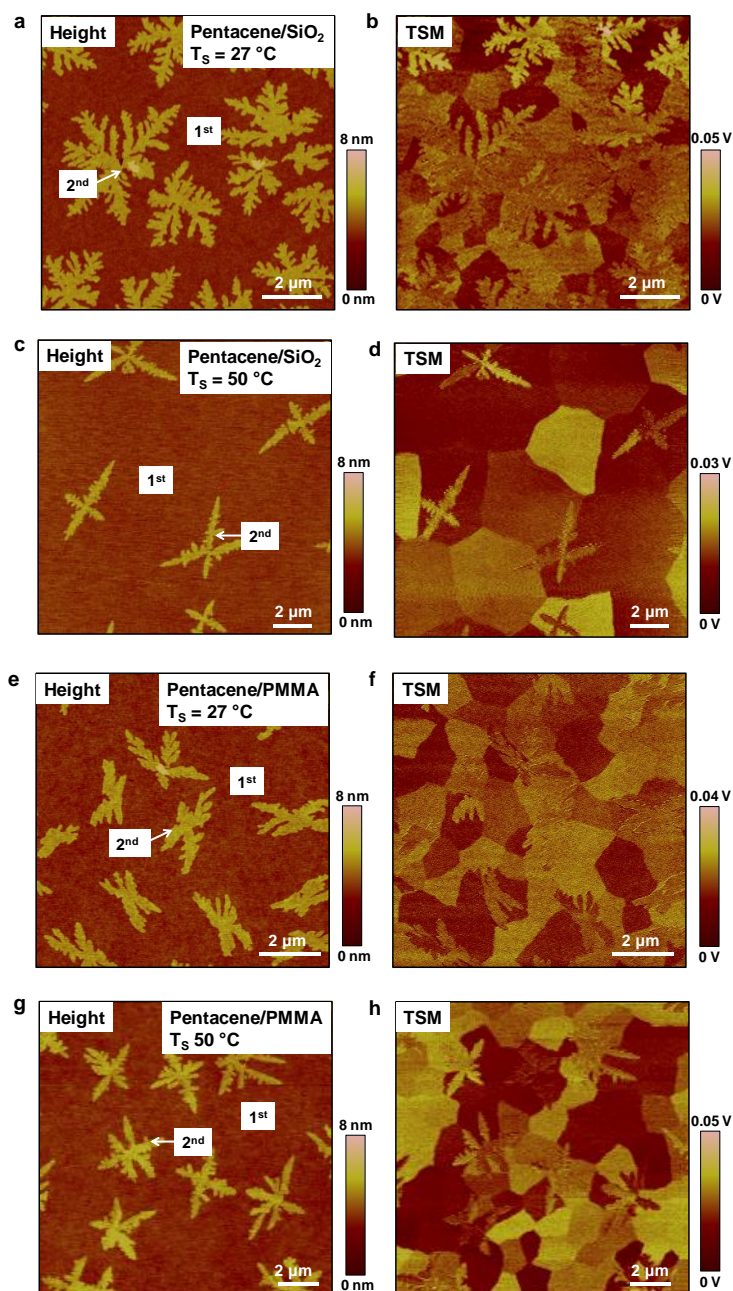
Figure A2.2 Topography and corresponding TSM images of pentacene bi-layers deposited on SiO₂ and PMMA at low and high substrate temperatures.

There are some differences in film morphology and nucleation density for films deposited on different substrates and at different substrate temperatures. The TSM images all show rich contrast, indicating grain orientations of both layers. There is always co-existence of type A and type B grains as defined in Figure 5.2, implying mosaic homoepitaxy regardless of the substrate type and deposition condition.

176

A3. Supplementary Information for Chapter 6

Measurement of Strains. XRD measurements were carried out to quantify the shift of 2θ positions of rubrene (0012), (313), and (113) diffraction peaks as a function of temperature. Examples of the raw data are shown in Figure A3.1. Out-of-plane 2θ-ω coupled scan was used to measure rubrene (0012) peak for both rubrene on PDMS and rubrene on Si. Off-axis 2θ-ω coupled scan was used to measure rubrene (313) and (113) diffraction peaks for rubrene on Si. The (313) and (113) peaks of rubrene on PDMS were measured by 2D reciprocal space mapping since these two peaks for rubrene on PDMS are very weak by off-axis 2θ-ω coupled scan and thus the accuracy is unsatisfactory. The corresponding d-spacings at different temperatures, d_{0012}, d_{313}, and d_{113}, can thus be determined with obtained 2θ by Bragg's law ($2d\sin\theta = n\lambda$). The changes of d-spacing at any elevated temperature relative to that at room temperature, i.e., d-spacing strains (ε d_{hkl}), were calculated for d_{0012}, d_{313}, and d_{113} and were averaged among multiple samples. The average d-spacing strains for rubrene on PDMS and rubrene on Si upon consecutive heating-cooling cycles are shown in Figure A3.2.

The average d-spacing strains along with their standard deviation errors were used to compute the total elastic strains along the three principal axes, a (ε a), b (ε b), and c (ε c) axes of rubrene. Since rubrene adopts an orthorhombic structure, the equation that relates the d-spacing d_{hkl} to the lattice parameters a, b, and c is given by

$$\frac{1}{d_{hkl}^2} = \frac{h^2}{a^2} + \frac{k^2}{b^2} + \frac{l^2}{c^2}$$

A sample calculation of a, b, c, εa, εb, εc, as well as their standard deviation errors is shown in Table A3.1. Figure A3.3 shows that the average total elastic strains (εa, εb and εc) exhibit good reversibility upon heating and cooling.
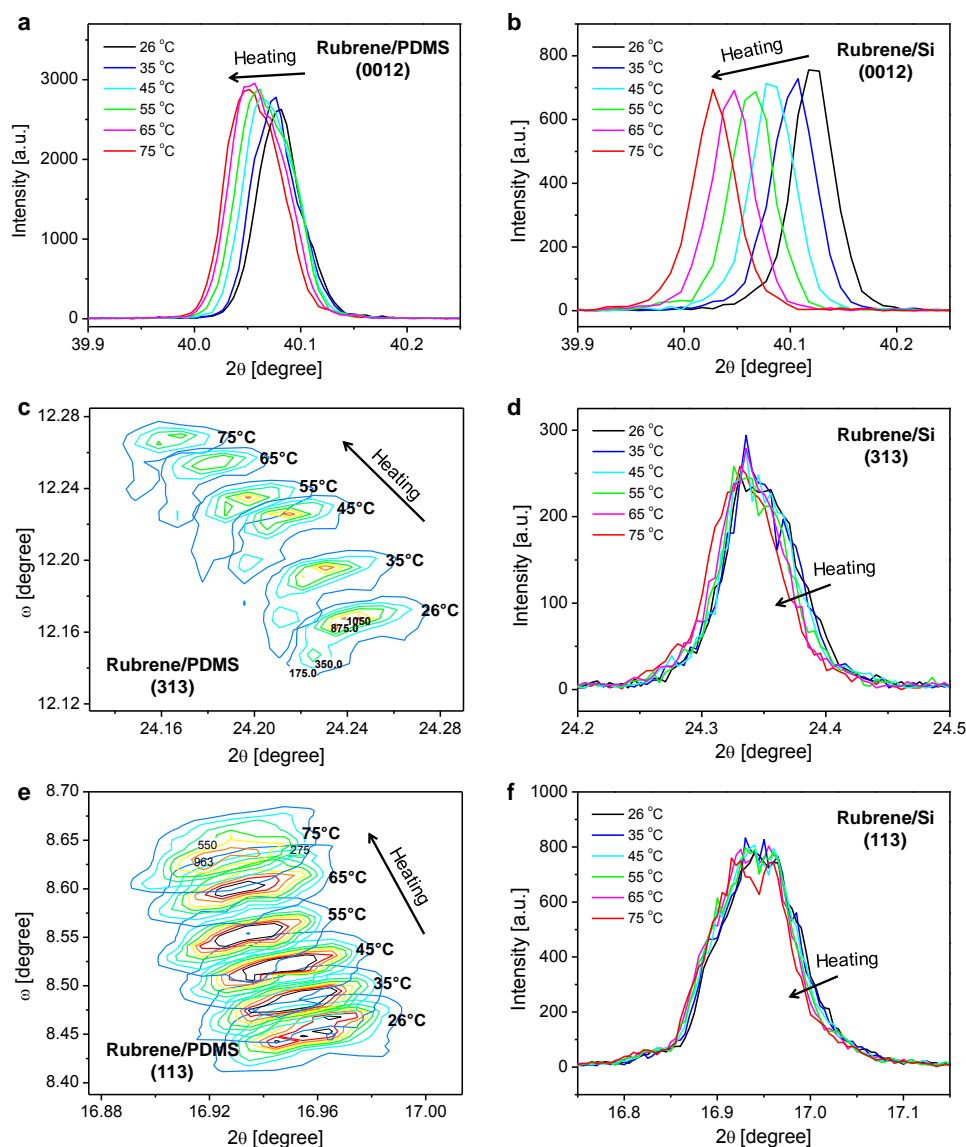
Figure A3.1 XRD measurements of 2θ as a function of temperature for the (0012), (313), and (113) diffraction peaks of rubrene laminated on PDMS and Si.
a. Out-of-plane $2\theta\text{-}\omega$ coupled scan of rubrene (0012) diffraction peak upon heating for rubrene on PDMS. b. Out-of-plane $2\theta\text{-}\omega$ coupled scan of rubrene (0012) diffraction peak upon heating for rubrene on Si. c. 2D reciprocal space mapping of rubrene (313) diffraction peak upon heating for rubrene on PDMS. 2D reciprocal space mapping instead of $2\theta\text{-}\omega$ coupled scan was used since the (313) diffraction peak for rubrene on PDMS obtained by $2\theta\text{-}\omega$ coupled scan is very weak. d. Off-axis $2\theta\text{-}\omega$ coupled scan of rubrene (313) diffraction peak upon heating for rubrene on Si. e. 2D reciprocal space mapping of rubrene (113) diffraction peak upon heating for rubrene on PDMS. 2D reciprocal space mapping instead of $2\theta\text{-}\omega$ coupled scan was used since the (113) diffraction peak for rubrene on PDMS obtained by $2\theta\text{-}\omega$ coupled scan is very weak. f. Off-axis $2\theta\text{-}\omega$ coupled scan of rubrene (113) diffraction peak upon heating for rubrene on Si.
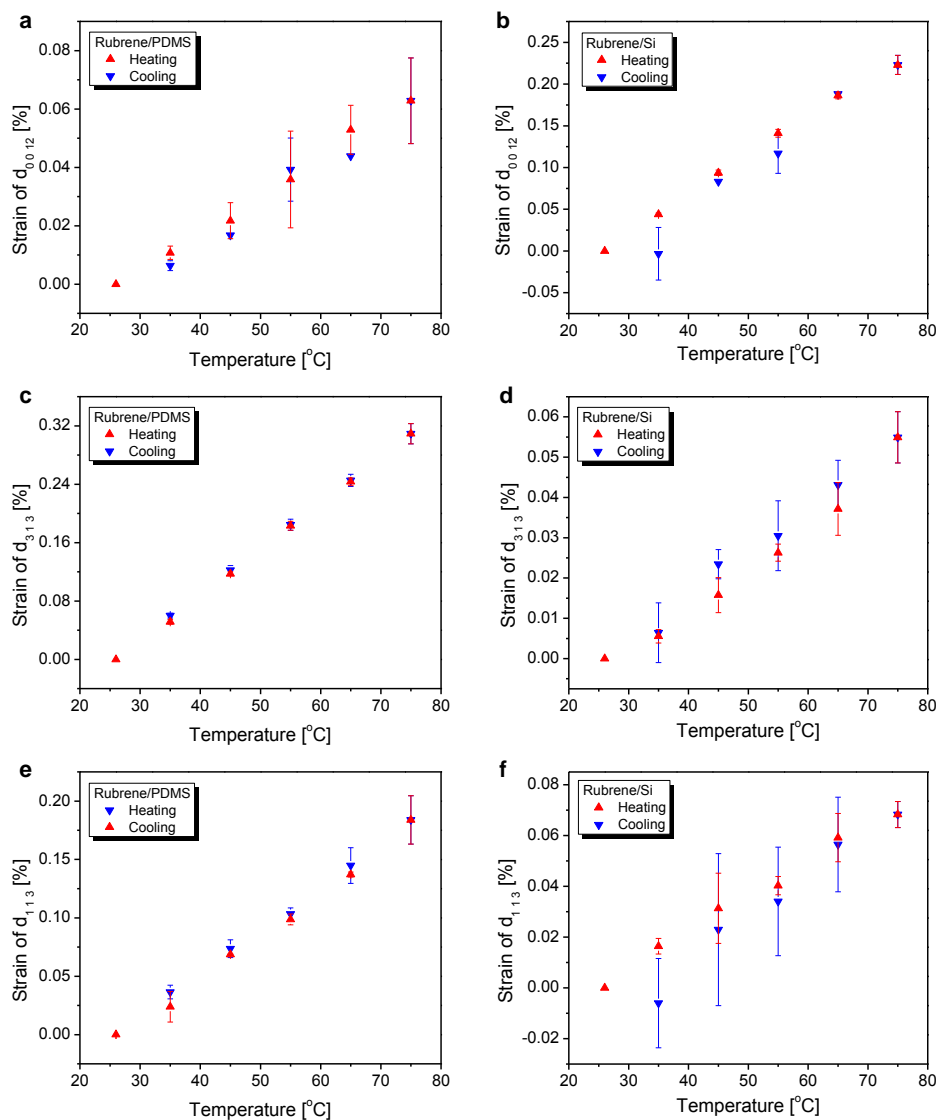
179

Figure A3.2 Average strains of the d-spacings as a function of temperature.
a. Average strain of d_{0012} as a function of temperature during heating and cooling obtained by measuring the (0012) peak shift of multiple rubrene samples on PDMS. b. Average strain of d_{0012} as a function of temperature during heating and cooling obtained by measuring the (0012) peak shift of multiple rubrene samples on Si. c. Average strain of d_{313} as a function of temperature during heating and cooling obtained by measuring the (313) peak shift of multiple rubrene samples on PDMS. d. Average strain of d_{313} as a function of temperature during heating and cooling obtained by measuring the (313) peak shift of multiple rubrene samples on Si. e. Average strains of d_{113} as a function of temperature during heating and cooling obtained by measuring the (113) peak shift of multiple rubrene samples on PDMS. f. Average strains of d_{113} as a function of temperature during heating and cooling obtained by measuring the (113) peak shift of multiple rubrene samples on Si.
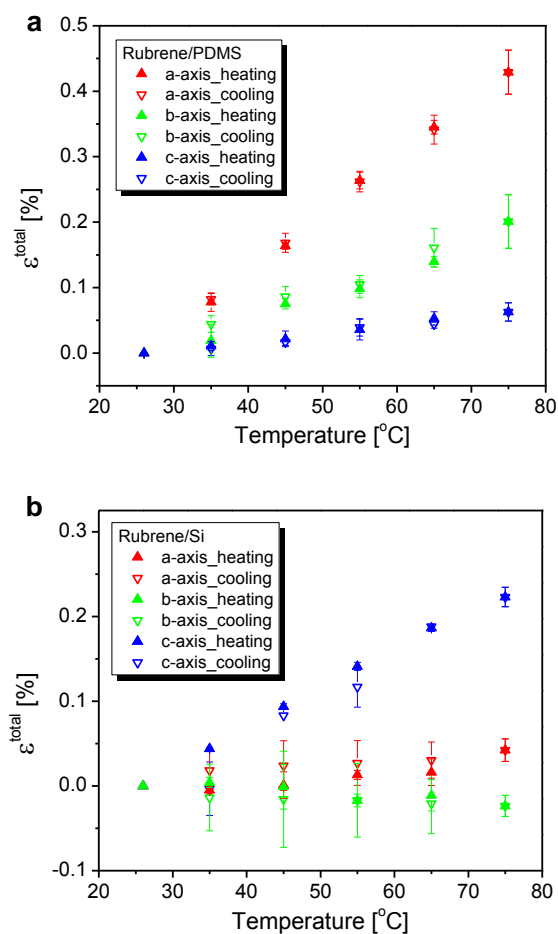
Figure A3.3 Reversibility of the average total elastic strain of rubrene on PDMS and rubrene on Si upon heating and cooling.
a. Average total elastic strain ε^{total} of rubrene a, b, and c axes as a function of temperature for crystals on PDMS during a continuous heating and cooling cycle. **b.** Average ε^{total} of rubrene a, b, and c axes as a function of temperature for crystals on Si during a continuous heating and cooling cycle. Both cases show very good reversibility of ε^{total}.

181

Table A3-1 Sample calculation of lattice parameters, lattice strains, and corresponding standard deviation errors based on measured average d-spacing strains of rubrene on PDMS at 55 °C.

Quantity	Unit	Value	Note
$\varepsilon\, d_{0012}$	%	0.03585	Average strain of d_{0012} for Rubrene/PDMS @ 55°C
$\delta\,(\varepsilon\, d_{0012})$	%	0.01581	Standard deviation of $\varepsilon\, d_{0012}$
$\varepsilon\, d_{313}$	%	0.18301	Average strain of d_{313} for Rubrene/PDMS @ 55°C
$\delta\,(\varepsilon\, d_{313})$	%	0.00608	Standard deviation of $\varepsilon\, d_{313}$
$\varepsilon\, d_{113}$	%	0.09868	Average strain of d_{113} for Rubrene/PDMS @ 55°C
$\delta\,(\varepsilon\, d_{113})$	%	0.00463	Standard deviation of $\varepsilon\, d_{113}$
d_{0012}	Å	2.248306	$d_{0012} = d_{0012}(\text{r.t.}) \times (1 + \varepsilon\, d_{0012})$; $d_{0012}(\text{r.t.}) = 2.2475$ Å
$\delta\,(d_{0012})$	Å	0.000355	$\delta\,(d_{0012}) = d_{0012}(\text{r.t.}) \times \delta\,(\varepsilon\, d_{0012})$
d_{313}	Å	3.659788	$d_{313} = d_{313}(\text{r.t.}) \times (1 + \varepsilon\, d_{313})$; $d_{313}(\text{r.t.}) = 3.653102$ Å
$\delta\,(d_{313})$	Å	0.000222	$\delta\,(d_{313}) = d_{313}(\text{r.t.}) \times \delta\,(\varepsilon\, d_{313})$
$1/(d_{313})^2$	Å^{-2}	0.07466	
$\delta\,(1/(d_{313})^2)$	Å^{-2}	9.0576×10^{-6}	$\delta\,(1/(d_{313})^2) = 2 \times \delta\,(d_{313})/(d_{313})^3$
d_{113}	Å	5.23462	$d_{113} = d_{113}(\text{r.t.}) \times (1 + \varepsilon\, d_{113})$; $d_{113}(\text{r.t.}) = 5.22946$ Å
$\delta\,(d_{113})$	Å	0.000242	$\delta\,(d_{113}) = d_{113}(\text{r.t.}) \times \delta\,(\varepsilon\, d_{113})$
$1/(d_{113})^2$	Å^{-2}	0.036495	
$\delta\,(1/(d_{113})^2)$	Å^{-2}	3.3743×10^{-6}	$\delta\,(1/(d_{113})^2) = 2 \times \delta\,(d_{113})/(d_{113})^3$
$\Delta 1$	Å^{-2}	0.038165	$\Delta 1 = 1/(d_{313})^2 - 1/(d_{113})^2$
$\delta\,(\Delta 1)$	Å^{-2}	9.6657×10^{-6}	$\delta\,(\Delta 1) = \{[\delta\,(1/(d_{313})^2)]^2 + [\delta\,(1/(d_{313})^2)]^2\}^{1/2}$
c	Å	26.97967	$c = 12 \times d_{0012}$
$\delta\,(c)$	Å	0.00426	$\delta\,(c) = 12 \times \delta\,(d_{0012})$
$\varepsilon\, c$	%	0.03585	$\varepsilon\, c = \varepsilon\, d_{0012}$
$\delta\,(\varepsilon\, c)$	%	0.01581	$\delta\,(\varepsilon\, c) = \delta\,(\varepsilon\, d_{0012})$
$9/c^2$	Å^{-2}	0.012364	
$\delta\,(9/c^2)$	Å^{-2}	3.9046×10^{-6}	$\delta\,(9/c^2) = 9 \times 2 \times \delta\,(c)/c^3$
a	Å	14.47813	$a = (8/\Delta 1)^{1/2}$
$\delta\,(a)$	Å	0.001833	$\delta\,(a) = 0.5 \times a \times \delta\,(\Delta 1)/\Delta 1$
$\varepsilon\, a$	%	0.264058	$\varepsilon\, a = [a - a(\text{r.t.})]/a(\text{r.t.})$; $a(\text{r.t.}) = 14.44$ Å
$\delta\,(\varepsilon\, a)$	%	0.012694	$\delta\,(\varepsilon\, a) = \delta\,(a)/a(\text{r.t.})$
$1/a^2$	Å^{-2}	0.004771	
$\delta\,(1/a^2)$	Å^{-2}	1.208×10^{-6}	$\delta\,(1/a^2) = 2 \times \delta\,(a)/a^3$
$\Delta 2$	Å^{-2}	0.01936	$\Delta 2 = 1/(d_{113})^2 - 1/a^2 - 9/c^2$
$\delta\,(\Delta 2)$	Å^{-2}	5.3×10^{-6}	$\delta\,(\Delta 2) = \{[\delta\,(1/(d_{113})^2)]^2 + [\delta\,(1/a^2)]^2 + [\delta\,(9/c^2)]^2\}^{1/2}$
b	Å	7.18699	$b = (1/\Delta 2)^{1/2}$
$\delta\,(b)$	Å	0.00098	$\delta\,(b) = 0.5 \times b \times \delta\,(\Delta 2)/\Delta 2$
$\varepsilon\, b$	%	0.09735	$\varepsilon\, b = [b - b(\text{r.t.})]/b(\text{r.t.})$; $b(\text{r.t.}) = 7.18$ Å
$\delta\,(\varepsilon\, b)$	%	0.01365	$\delta\,(\varepsilon\, b) = \delta\,(b)/b(\text{r.t.})$

Table A3-2 Theoretical absolute values (in eV) of the potential energy at the vacuum level (E$_{vac}$), the valence band maximum (VBM), and the work function (WF) for rubrene on PDMS and rubrene on Si at different temperatures. The VBM values correspond to two-layer slabs, relaxed at fixed unit-cell parameters (taken from the experimental work). Each E$_{vac}$ value is calculated at the vacuum level (30 Å thick vacuum layers added over the rubrene slabs). The electronic properties are calculated with the PBE functional.

	E$_{vac}$ (eV)		Δ E$_{vac}$ (eV)	VBM (eV)		ΔVBM (eV)	WF (eV)		ΔWF (eV)
T (°C)	26	75		26	75		26	75	
Rubrene/Si	2.463	2.473	0.010	-1.518	-1.500	0.018	3.981	3.973	-0.008
Rubrene/PDMS	2.463	2.459	-0.004	-1.518	-1.523	-0.005	3.981	3.982	0.001